Title

Thermal Effects and Activation in Josephson Junctions

Author

Cheng, Chungho

Publication Date

2023

Peer reviewed|Thesis/dissertation

Thermal Effects and Activation in Josephson Junctions

By

CHUNGHO CHENG

DISSERTATION

Submitted in partial satisfaction of the requirements for the degree of

DOCTOR OF PHILOSOPHY

in

Mechanical and Aerospace Engineering

in the

OFFICE OF GRADUATE STUDIES

of the

UNIVERSITY OF CALIFORNIA

DAVIS

Approved:

_____

Niels Grønbech-Jensen, Chair

_____

Zhaojun Bai

_____

Francois Gygi

Committee in Charge

2023

To My Youth

CONTENTS

LIST OF FIGURES

LIST OF TABLES

ABSTRACT

Thermal Effects and Activation in Josephson Junctions

The Josephson effect is one of the macroscopic quantum phenomena and it was predicted by B.D Josephson in 1962. For a typical S-I-S Josephson junction, there exists a continuous supercurrent across the junction without any external voltage applied due to the Cooper pair tunnelling. The Cooper pair is a bound state of a pair of electrons caused by a small attraction due to the electron-phonon interaction in a metal at low temperatures. When the temperature is increased or external bias voltage is imposed, the Cooper pairs could be broken due to the thermal motion or the voltage overcoming the binding energy of the paired electrons. The term "activation" or "switching" of Josephson junction from superconducting state to normal or resistive state refers to such a process, that the normal electrons formed from the broken Cooper pairs result in a normal current, which is higher than a threshold, namely, critical current, so that a voltage drop across the junction can be measured and the current-voltage relation satisfies the Ohm's law.

According to the Josephson relations, the current flowing through the junction is characterizes by the phase difference between the two superconductors of the junction, and the resistively and capacitively shunted junction (RCSJ) model was proposed in 1968 for the description of phase dynamics. The governing equation of the phase difference is a Langevin equation analogously describing a Brownian particle moving in a periodic potential well. Accordingly, the escape of Brownian particles from the well was used to study the switching of the junction. The RCSJ model in the past five decades has been accepted as a good model for successfully providing a switching mechanism called "thermal activation (TA)" at high temperatures relative to the "crossover temperature". As a series of Josephson experiments were reported during 1980s, the RCSJ model was considered failing to explain some phenomena, such as the saturation of the switching current distribution (SCD) as the temperature is down to zero. Meanwhile, the theory of macroscopic quantum tunnelling (MQT) was built; the phase was quantized and the saturation of SCD was attributed to the tunnelling of the phase particle through the potential barrier. As a test for the secondary quantum effect, MQT has been accepted as a main theory

for the interpretation of saturation of SCD in Josephson switching experiments.

In this dissertation, we try to explore a classical switching mechanism as an alternative and simpler description for the phase difference of the Josephson junction at low temperatures besides MQT. The content of this thesis is structured as follows: in Chapter 1, we review the background of Josephson effect and present some of the key concepts that will be used in the following chapters. In Chapter 2, by solving the Langevin equation of the RCSJ model using the GJ thermostat method, we will investigate the effects of the parameters in the equation, such as damping, temperature, sweep rate and initial conditions. Non-equilibrium phenomena are observed and discussed. In Chapter 3, the effects of initial conditions, especially the saturation phenomena in non-equilibrium state will be discussed. In Chapter 4, with the understandings on the classical switching mechanism of the junction, we will compare the results generated by our model to the published experimental data. Up to Chapter 4, our discussion is based on a single Josephson junction, while in Chapter 5, the simulation will be generalized to a one-dimension long Josephson junction, which will be a more complex system in which additional phenomena, such as kink-soliton, can be studied. In Chapter 6, we summarize the discussion in this dissertation.

ACKNOWLEDGMENTS

I would like to express my deepest appreciation to Professor Niels Grønbech-Jensen, my supervisor, who led me to the field of applied physics, especially Josephson junction and molecular dynamics. Josephson junction is an important superconducting device involving the subjects from classical to quantum physics, from fundamental physics to engineering applications. It is worth working on it with a whole life. Professor Grønbech-Jensen helped me a lot in research, teaching and daily life. I am glad to be able to work with him as an engineering graduate student.

I would like to thank Professor Matteo Cirillo for his help in research and for reviewing this dissertation. We have a long term communication and I always benefit from his valuable discussions on the Josephson problems. I also would like to thank Professor James Blackburn. I learn many from him especially the algorithm on the escape simulation. Hope I can still work with them in the future.

I would like to thank Professors Zhaojun Bai and Francois Gygi, for serving for the dissertation Committee, reading my dissertation carefully and giving me valuable advice for the revision. Thanks also go to Jean-Pierre Delplanque, Raissa D'Souza, Zhaojun Bai (again), Richard Scalettar, and Mohamed Hafez, for being the Committee members of my qualifying exam. Especially for Professor Mohamed Hafez, we have known each other for over seven years; thanks for his help when taking his classes and when being his TA for the PDE class.

I would like to thank my friend, Bohan Zhu. I am always astonished by his polymathy and enjoy our random talks on all kinds of subjects. Hope one day in the future I can work with him in academics.

I would like to thank Basil Wong, our group leader when I worked in Port of Oakland before coming to UC Davis. Thank him for his encouragement and for writing me the recommendation letter for the graduate school application.

I would like to thank my family, including my grandma, my parents, younger brother, Bob and Ben, for their supports and the patience for my immaturity and heavy procrastination in the recent two years.

I would like to thank my friend, Weilai, for her companion during the difficult time.

Finally, thank UC Davis for giving me the offer of admission to the graduate school. With all mentioned and not mentioned above, I can be here writing up this dissertation.

Chapter 1

Introduction

1.1 Historical background

During 1950s-1960s, the modern physics was still in its "silver age". The story of the Josephosn junction at least can be traced back to the birth of the concept of "Cooper pair", which was proposed by Leon Cooper in 1956 [1]. Later in 1957, the basic theory of superconductivity, BCS theory, has been built up by Bardeen, Cooper, and Schrieffer [2]. In 1962, Brian David Josephson in 1962 predicted theoretically that besides the single particle tunneling, there exists Cooper pairs tunneling currents between two superconductors separated by an thin insulated film [3]. This prediction in three pages of paper paved the way to the study of a series of new physics and important applications of electric devices up to nowadays. Shortly, in January of 1963, Philip Anderson and John Rowell [4] reported that the DC Josephson effect was observed - the current-voltage characteristics for the tin-tin oxide-lead junction at 1.5 K indicated there was a 0.3 mA of direct tunneling current survived under the very weak interior magnetic field without external voltage applied. Later in June, S.Shapiro confirmed the direct-current Josephson effect and represented an indirect proof for Josephson's alternating-current [5]. Besides in coupled superconductors, the Josephson-type effects can also be found in neutral matter, such as ^{4}He and ^{3}He-B that can be described by a macroscopic wave function of the form $\Psi = \sqrt{\rho_s}e^{i\varphi}$, where ρ_s is the superfluid density and φ is an actual phase. Anderson's consideration on the flow of superfluid ^{4}He [6] provided a groundwork for the search of these kind of phenomena, e.g., Superfluid Hydrodynamics [7] in 1965.

Plasma resonance is an oscillatory mode of the junction in the zero-voltage state due to the exchange of energy between equivalent inductor and capacitor in the Josephson junction [8]. This phenomenon was pointed out by Anderson [9] in 1964 and later discussed by Josephson [10] in 1965. The experimental confirmation was performed by Dahm et al. in 1968 for small amplitude limit [11], and in 1975 for large amplitude [12].

In 1968, to study the current-voltage relation of weak-link junctions, the relaxation oscillations in Josephson junctions was proposed by Stewart [13, 14]. This model gives an equivalent circuit for the weakly coupled superconductors and the corresponding system equation for the phase with a fluctuation terms will turn to a Langevin equation, which, together with the well-known escape theories from from Kramers in 1940 [15] and Buttiker et al. in 1983 [16], successfully describes the switching process of the junction, namely, "thermal activation (TA)" at high temperatures[1] in the Brownian particle analogy (phase particle).

Besides the escape rate of the particle of the junction, the switching current distribution (SCD) is another characteristic of the junction, where the information of the switching or activation process is encoded. In 1972, Kurkijärvi theoretically considered the transition distribution for the intrinsic fluctuations in a superconducting ring closed with a Josephson junction in a magnetic flux and found that the width of distribution is proportional to the power of $2/3$ of temperature [17]. This was experimentally confirmed by L D. Jackel et, al in 1973 for the same system [18]. The first SCD experiment of an extremely underdamped Josephson junction are presented by Paolo Silvestrini et al. [19] in 1988, and it showed that the junction resistance depended on the superconductor energy gap and temperature in an exponential form.

In 1980s, a series of experiments [20–24] show that the escape rate of the phase particles and switching current distribution was measured to be temperature-independent at low temperatures. This kind of saturation phenomenon was considered a proof of the failure of the classical escape theories and RCSJ model at low temperatures. Hence, on the theory side, macroscopic quantum tunneling (MQT), the second switching mechanism for the Josephson junction was proposed [25–28] almost simultaneously. This is a "secondary quantum macroscopic effect" based on

[1] In this thesis, the term "high temperature" refers to a temperature relatively higher than the "crossover temperature" but lower than the critical temperature (T_c) of the junction, or roughly speaking, $\hbar\omega_{j0} < k_B T < k_B T_c$; a "low temperature" for e.g., MQT, refers to a temperature lower than the "crossover temperature" and down to zero, or $0 < k_B T < \hbar\omega_{j0}$. Here, k_B is the Boltzmann constant and ω_{j0} is the zero-bias plasma frequency of the junctions.

quantum postulates, which may not be necessary [29]. Nevertheless, MQT is considered a main theory for interpreting the phase behaviours in the Josephson junction at low temperatures nowadays.

On the other hand, the Kramers and BHL escape rates theory based on the assumption of equilibrium state under small damping condition, fail to give a consistent result as the Langevin simulation does. This phenomenon attributes to the non-equilibrium effects, including the "finite barrier effect" [30, 31]. The efforts for improving the Kramers or BHL model, or finding an expression for the escape rate of Brownian particle has been made in the past four decades [30, 32, 33] and is still going on even today.

1.2 Physical background - Josephson relations

The basic Josephson relations can be derived by many approaches, such as the Ginsburg-Landau equations, the gauge invariance, etc. Following is a simple derivation given by Feynman [34] and can be found in many of the textbooks on solid state physics or superconductivity [8]. Since we only focus on the fundamental physics of Josephson junction, let's confine the topic to the case that a S-I-S tunnel junction (Figure 1.1) with two pieces of superconductors is separated by a thin insulated barrier, through which, the Cooper pairs tunnel from one side to the other [1].

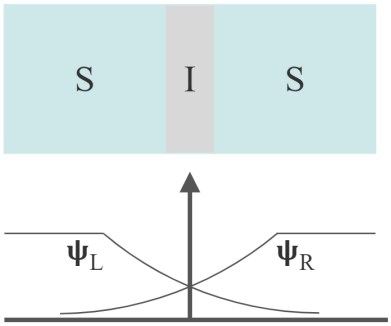

Figure 1.1. Upper: two superconductors separated by a thin insulating barrier; Lower: the superconducting order parameters Ψ for each side.

The macroscopic states of the junction of the left and right are described respectively by a single state function ψ_L and ψ_R. Let the total state function be

$$\Psi = \sqrt{n_s}\mathrm{e}^{i\varphi} \tag{1.1}$$

where $n_s = |\Psi|^2$ is the concentration of the electrons that form the Cooper pairs, and the constant φ indicates all of the Cooper pairs have the same phase due to the condensation of bosonic Cooper pairs. Ψ satisfies the Schrödinger equation

$$i\hbar\partial_t|\Psi\rangle = H|\Psi\rangle \tag{1.2}$$

with

$$|\Psi\rangle = \psi_L|L\rangle + \psi_R|R\rangle \tag{1.3}$$

$$\begin{aligned} H &= H_L + H_R + H_T \\ &= E_L|L\rangle\langle L| + E_R|R\rangle\langle R| + K(|L\rangle\langle R| + |R\rangle\langle L|) \end{aligned} \tag{1.4}$$

where $\hbar = \frac{h}{2\pi}$ is the reduced Planck constant; L, the state of the left piece of the superconductor and R for the right one; K, a constant related to the interaction between the two superconductors. Substituting the above state function and Hamiltonian in (1.2), and using orthogonality of the base, we get two equations of the right and left superconductors respectively:

$$\begin{aligned} i\hbar\partial_t\psi_R &= E_R\psi_R + K\psi_L \\ i\hbar\partial_t\psi_L &= E_L\psi_L + K\psi_R \end{aligned} \tag{1.5}$$

By (1.1), letting $\psi_L = \sqrt{n_L}e^{i\varphi_L}$ and $\psi_R = \sqrt{n_R}e^{i\varphi_R}$, substituting them into (1.5), and separating the real and image parts, we get:

$$\partial_t n_L = -\partial_t n_R = \frac{2K\sqrt{n_L n_R}}{\hbar}\sin(\varphi_R - \varphi_L) \tag{1.6}$$

$$\partial_t(\varphi_R - \varphi_L) = -\frac{E_R - E_L}{\hbar} \tag{1.7}$$

We assume $n_R = n_L = n$ due to the symmetry of the junction, noting that the supercurrent density is the rate of the density of the tunneling Cooper pairs: $j \equiv (2e)\partial_t n$, with e being the charge of an electron, so the supercurrent is $I = jA$ with A being the cross-section area of the junction. If the voltage applied to the junction is V, the potential change across the barrier will be $E_R - E_L = -2eV$. Hence, we obtain the two Josephson relations respectively from (1.6) and (1.7):

$$I = I_c\sin\varphi \tag{1.8a}$$

$$\partial_t\varphi = \frac{2eV}{\hbar} \tag{1.8b}$$

where $I_c = j_c A$ is the maximum Josephson supercurrent (aka "critical current"), and $j_c = 4eK\sqrt{n_L n_R}/\hbar$ is the current density. Therefore, it can be seen that (1) if $V = 0$, then the phase is constant φ_0, so is the supercurrent, $I = I_c \sin\varphi_0$ (DC Josephson effect). (2) if V is constant, then $I = I_c \sin(2eVt/\hbar + \varphi_0)$, meaning the supercurrent is oscillating with a frequency $\omega = 2eV/\hbar$ (AC Josephson effect). These two phenomena have been respectively observed in Anderson and Shapiro's experiments mentioned above.

1.2.1 The S and R states, critical current I_c

The critical current I_c of Josephson junction is defined to be the maximum Josephson supercurrent, determined by the structure of the junction and sensitive to temperature and magnetic field [4, 35–37]. When the DC current I through the junction within the interval of $[-I_c, I_c]$, according to relation (1.8b), the voltage drop will be zero, and the junction is said to be in "S state" (superconducting or stationary state). The situation beyond I_c could be attributed to the normal current (I_N) formed by conductive quasi-particles from the breaking of Cooper pairs due to thermal motion or bias voltage over the gap. Since the normal current satisfies Ohm's law (see Figure 1.5) [38], the junction is said to switch to the "R state" (Resistive state).

Although in this thesis, the critical current I_c is assumed to be constant, it is worth noting here that in general it is temperature and magnetic-field dependent. Only considering the case without magnetic field that reduces I_c, for symmetrical junctions, a well-known analytic expression for temperature dependent I_c was given by Ambegaokar and Baratoff in 1963 [39] based on the BCS theroy:

$$I_c = \frac{\pi\Delta(T)}{2eR_N}\tanh\left[\frac{\Delta(T)}{2k_BT}\right] \tag{1.9}$$

in which, $\Delta(T)$ is the gap energy; R_N, the normal state resistance of the junction, and k_B, the Boltzmann constant. At temperature T, the gap energy is approximated by

$$\frac{\Delta(T)}{\Delta(0)} = \tanh\left[\frac{T}{T_c}\frac{\Delta(T)}{\Delta(0)}\right] \tag{1.10}$$

where T_c is the critical temperature of the superconductor and $\Delta(0) \approx \pi k_B T/1.78$. The quantity $I_c R_N$ is another characteristic parameter of Josephson junction dependent on the parameters of the junction at certain T.

1.2.2 Josephson inductance, energy, and plasma oscillation

Combining the Josephson relations (1.8a) and (1.8b) yields a relation between voltage and the rate of current:

$$V = L(\varphi)\frac{dI}{dt} \tag{1.11}$$

where $L_j(\varphi) = \frac{\hbar}{2eI_c\cos\varphi}$, and $L_{j0} \equiv L(0) = \frac{\hbar}{2eI_c}$ is called Josephson inductance [40]. Thus, one can calculate the energy stored in this non-linear "inductor":

$$E_j = \int_0^t IV dt = E_{j0}[1-\cos\varphi(t)] \tag{1.12}$$

where $E_{j0} = \frac{I_c\hbar}{2e}$ is the zero-bias Josephson energy that relates to coupling energy between the phases of the gap functions on the two sides [4].

Due to the similar structure as a capacitor, there exists a charge difference and displacement current (I_D) between the two electrodes of the junction so one can treat the junction as a LC circuit. Letting C be the capacitance of the junction, the plasma frequency of Josephson junction can be defined as

$$\omega_j \equiv \frac{1}{\sqrt{L_jC}} = \omega_{j0}\left[1-\left(\frac{I}{I_c}\right)^2\right]^{1/4} \tag{1.13}$$

where $\omega_{j0} = \left(\frac{2eI_c}{\hbar C}\right)^{\frac{1}{2}}$ is called zero-bias plasma frequency of the Josephson junction, and this kind of mode exists in the zero-voltage state (or S state) of the junction; once $I > I_c$, the junction switches to R state and a voltage drop V can be measured; by relation (1.8b), the frequency will be determined by $\omega = 2eV/\hbar$. The voltage at $I = I_c$ is called characteristic voltage: $V_c = I_cR_N$, where R_N is the normal resistance of the junction. Correspondingly, one can define another "characteristic frequency" of Josephson junction, as: $\omega_c = 2eV_c/\hbar$.

On the other hand, the electrical energy stored in the junction, similar to a capacitor, can be written as

$$E_c = \frac{CV^2}{2} = \frac{1}{2}C\left(\hbar\frac{\partial_t\varphi}{2e}\right)^2 = \frac{1}{2}\frac{\varphi'^2}{\omega_{j0}^2}E_{j0} = \frac{1}{2}\dot{\varphi}^2E_{j0} \tag{1.14}$$

$$\text{or}: \quad E_c = \frac{Q^2}{2C} = \frac{1}{2}\left(\frac{N\hbar\omega_{j0}}{E_{j0}}\right)^2 E_{j0} \tag{1.15}$$

where $Q = 2eN$ with N being the total number of Cooper pairs in the junction deviating from the electrical equilibrium; $\varphi' \equiv \partial_t \varphi$, whose dimensionless form is $\dot{\varphi} \equiv \partial_\tau \varphi = \varphi' \omega_{j0}$ with the time variable t normalized by ω_{j0} as $\tau = \omega_{j0} t$. If an external current source (I) is applied to the junction, one must consider the energy it induced. By the first Anderson equation [7, 9, 41]:

$$\partial_\varphi E_{ext} = \hbar \frac{dN}{dt} = -\frac{\hbar I}{2e} \tag{1.16}$$

we have $E_{ext} = -\hbar I \varphi / 2e = -E_{j0}(I/I_c)\varphi$. Summing up these energies considered above, finally, we obtain an expression for the total Hamiltonian of the junction:

$$H = K(\varphi') + U(\varphi) = E_{j0} \left[\frac{1}{2}\dot{\varphi}^2 + (1 - \cos\varphi - \eta\varphi) \right] \tag{1.17}$$

$$\overset{\text{or}}{=} E_{j0} \left[\frac{1}{2} \left(\frac{N\hbar\omega_{j0}}{E_{j0}} \right)^2 + (1 - \cos\varphi - \eta\varphi) \right] \tag{1.18}$$

where K and U respectively corresponding to the "kinetic" and "potantial" energies. The kinetic terms in these two expressions should be equal, so that

$$\dot{\varphi} = N\hbar\omega_{j0}/E_{j0} \tag{1.19}$$

This makes sense because according to the relation (1.8b), the phase derivative is proportional to the voltage crossing the junction, which is dependent on the number of charges (N) distributed on the two electrodes of the junction. For the normalized phase derivative, when only one Cooper pair is tunnelling, i.e., $N = 1$, there exists a minimum $\dot{\varphi}_{min} = \hbar\omega_{j0}/E_{j0}$.

It is worth noting here that the plasma oscillation existing in the zero-voltage state is due to the pulsating energy exchange between the K and U terms in expression [8], or say, it is the oscillation in the equivalent LC circuit of the junction, as seen from discussion around expression (1.13). The plasma oscillation was theoretically discussed by Anderson and Josephson [9, 10], and experimentally confirmed by Dahm et al. [12]. Based on the Anderson equation, the zero-voltage plasma oscillation will result in a chemical potential [7, 9], which will play an important role in the Kramers and Langevin simulations (see Chapter 4).

1.2.3 The uncertainty relation

Up to now the discussion is still classical. The quantization of the phase difference is based on the postulation that the phase φ and number of Cooper pairs N satisfy $-i\partial_\varphi \Psi = N\Psi$, which

gives the operator $N \equiv -i\partial_\varphi$, where Ψ is the wave function [7, 9]. Thus, the commutator is $[\varphi, N] = i$. Following from the Robertson uncertainty relation, one gets [38]

$$\sigma_\varphi \sigma_N \geq \frac{1}{2} \tag{1.20}$$

where σ_φ and σ_N denote the corresponding standard deviations. By (1.19), the commutator of the phase and its normalized time derivative will be $[\varphi, \dot{\varphi}] = i\hbar\omega_{j0}/E_{j0}$, and the uncertainty relation reads

$$\sigma_\varphi \sigma_{\dot{\varphi}} \geq \frac{\hbar\omega_{j0}}{2E_{j0}} \tag{1.21}$$

where σ_φ and $\sigma_{\dot{\varphi}}$ are the standard deviations of φ and its normalized times derivative $\dot{\varphi}$. In this thesis, however, this postulation is not involved, and the relation between the phase and its time derivative will be just simply $\dot{\varphi} = d\varphi/d\tau$.

Besides, since for the S state, $|I| = |\frac{dQ}{dt}| \leq I_c$, where $Q = 2eN$, we have

$$\frac{dN}{d\tau} \leq \left(\frac{\hbar\omega_{j0}}{E_{j0}}\right)^{-1} \tag{1.22}$$

where $\tau \equiv t/t_0$ is the dimensionless time normalized to $t_0 = 1/\omega j0$. When $I = I_c$, the equal sign is taken. It can be seen one of the physical meaning of the quantity $\hbar\omega_{j0}/E_{j0}$, the inverse of which, gives an upper boundary for the rate of change of the tunneling Cooper pairs in the S state of Josephson junction.

1.3 RCSJ Model - phase dynamics

The Josephson relations (1.8a) and (1.8b) characterize the supercurrent I_S formed by the Cooper pair tunneling. For a real Josephson junction, as we have mentioned in the last section, there also exists a normal current I_N for quasi-particle tunneling and displacement current I_D for junction capacitance due to its S-I-S structure. On the other hand, according to the Josephson relations, the current and voltage are controlled by the phase difference φ, which is a macroscopic variable describing the collective behavior of the electrons in superconductor. Hence, one might wonder if there is an time-evolution equation for the phase variable. In 1968, W. J. Johnson, D. E. McCumber [13], and W.C.Stewart [14] proposed an model that captures the essential characteristics of a real Josephson device. Assuming the size of the junction is small and there is

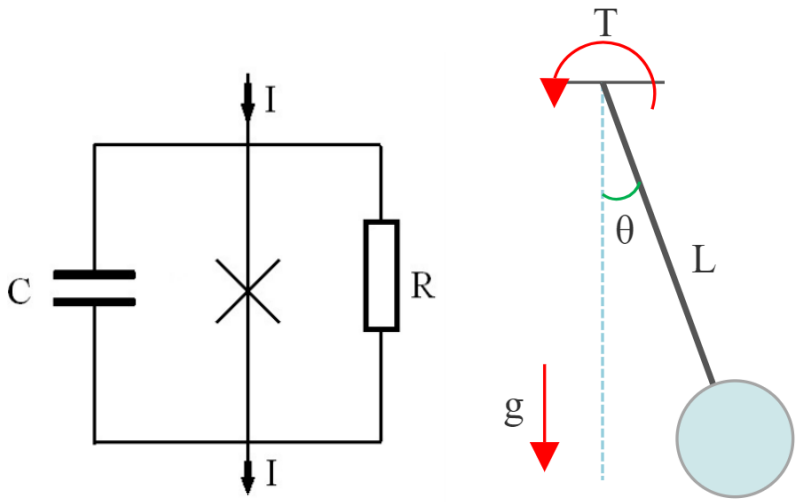

Figure 1.2. Left: The equivalent circuit of RCSJ model; Right: A simple pendulum analog to the RCSJ model

no magnetic field applied, besides the Cooper-pair tunneling current given by equation (1.8a), the normal current is given by $I_N = V/R = \frac{\hbar}{2eR}\varphi'$, in which, R is the junction resistance, and the displacement current is $I_D = C\partial_t V = \frac{\hbar C}{2e}\varphi''$, with C being the capacitance of the junction. In addition, fluctuation current I_F due to thermal noise should also be taken into account (neglecting the other kinds of noise, such as shot noise, "'1/f" noise, etc.). Letting the overall current be I and summing up these four branches of currents above by Kirchhoff's law (Figure 1.2) as $I = I_D + I_N + I_S + I_F$, one can obtain a stochastic differential equation (Langevin equation) for the phase difference across the junction:

$$\frac{\hbar C}{2e}\varphi'' + \frac{\hbar}{2eR}\varphi' + I_c \sin\varphi + I_F = I \tag{1.23}$$

where $\varphi' \equiv \partial_t \varphi$ and the thermal fluctuation current I_F is assumed to be characterized by the white noise that satisfies

$$\langle I_F(t)\rangle = 0 \tag{1.24a}$$

$$\langle I_F(t) I_F(t')\rangle = \frac{2k_B T}{R}\delta(t-t') \tag{1.24b}$$

where k_B is the Boltzmann constant and T is temperature. This model is called "resistively and capacitively shunted Josephson Junction (RCSJ)" model, providing a rule for the evolution of the phase difference across the junction.

1.3.1 Mechanical analogy and washboard potential

Equation (1.23) can be analogous to the motion equation of the torque driven pendulum in a uniform gravitational field (Figure 1.2) or a Brownian particle moving in a tilted periodic potential. For the pendulum, the equation reads

$$\theta'' + \frac{b}{m}\theta' + \frac{g}{L}\sin\theta = \frac{T}{mL^2} \tag{1.25}$$

where θ is the angle between the pendulum and the direction of the gravity g; m, the mass of the pendulum; b, the damping coefficient; g the gravitational acceleration; L the length of the string, and T is the external torque that biases the pendulum. The characteristic angular frequency and potential energy extracted from (1.25) are respectively $\omega_0 = \sqrt{g/L}$ and $U = mgL(1-\cos\theta) + \tau\theta$. Thus, rewriting equation (1.23) as

$$\left(\frac{\hbar}{2e}\right)^2 C\varphi'' + \left(\frac{\hbar}{2e}\right)^2 \frac{1}{R}\varphi'' = -\partial_\varphi\left[E_{j0}\left(1-\cos\varphi - \frac{I-I_F}{I_c}\varphi\right)\right] \tag{1.26}$$

or

$$\varphi'' + \frac{1}{RC}\varphi' + \frac{2eI_c}{\hbar C}\sin\varphi = \frac{2e}{\hbar C}(I-I_F). \tag{1.27}$$

we have the potential of the phase particle as

$$U(\varphi) = E_{j0}\left[(1-\cos\varphi) - \frac{I-I_F}{I_c}\varphi\right] \tag{1.28}$$

where $E_{j0} = \frac{\hbar I_c}{2e}$. This periodic function is called "washboard potential" in the analogy of Brownian or phase particle. Thus, the frequency of the phase particle oscillating in the washboard potential can be obtained as $\omega_j^2 = \partial_t^2 U/m = \frac{2eI_c}{\hbar C}\sqrt{1-\eta^2}$, where $m = \hbar^2 C/4e^2$ is the "mass term" in equation (1.26). This expression is consistent with (1.13) from the equivalent LC circuit.

1.3.2 The normalized forms

For convenience in numerically solving the Langevin equation (1.23), we prefer to normalize it using the characteristic time $t_0 = 1/\omega_{j0}$, hence, equation (1.23) becomes

$$\ddot{\varphi} + \alpha\dot{\varphi} + \sin\varphi = \eta + \beta \tag{1.29}$$

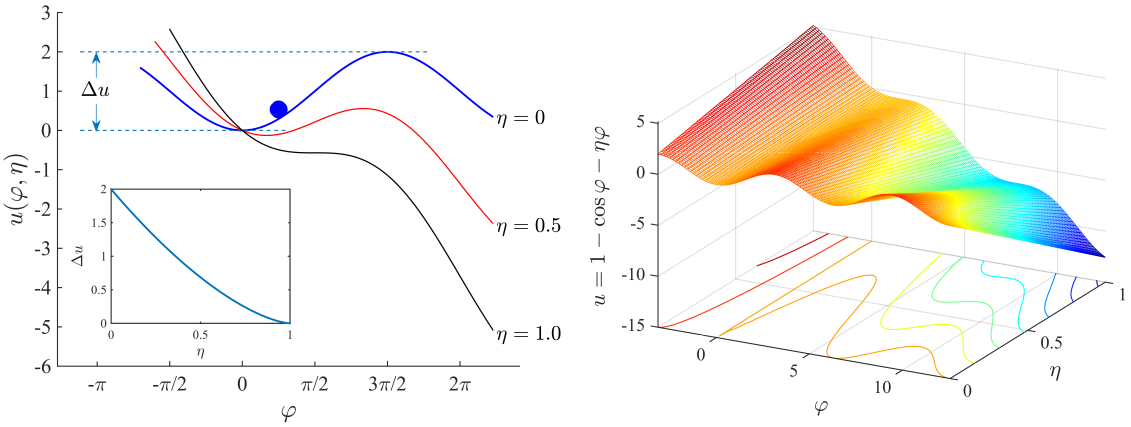

Figure 1.3. Normalized tiled washboard potential without noise term. The left plot presents three screenshot of the well under three values of η and in the inset is the height of the well as a function of η; the right one is the potential surface if the potential is treated as a two-variable function of η and φ.

where the normalized time $\tau = t/t_0$, phase derivative $\dot{\varphi} \equiv \frac{d\varphi}{d\tau}$, damping coefficient $\alpha = \frac{\hbar\omega_{J0}}{2eI_cR} = \frac{1}{\omega_{j0}RC}$ and external bias current $\eta = I/I_c$. The thermal fluctuation $\beta = -I_F/I_c$ having the properties given by (1.24a) and (1.24b) can be normalized as

$$\langle \beta(\tau) \rangle = 0 \tag{1.30a}$$

$$\langle \beta(\tau)\beta(\tau') \rangle = 2\alpha\theta\delta(\tau - \tau') \tag{1.30b}$$

where $\theta \equiv k_BT/E_{j0}$ is the normalized temperature. In this thesis, we tend to use the Brownian particle or phase particle analogy, saying that the phase particle is moving in a washboard potential with a normalized form

$$u(\varphi) = U/E_{j0} = (1 - \cos\varphi) - \eta\varphi - \beta\varphi \tag{1.31}$$

as shown in Figure 1.3. The dimensionless Hamiltonian of the phase particle then can be written as

$$\tilde{H} = \frac{1}{2}\dot{\varphi} + (1 - \cos\varphi) - \eta\varphi - \beta\varphi \tag{1.32}$$

which is identical to expression (1.17) with the energy consideration in the absence of the noise term. Meanwhile, the bias plasma frequency normalized to ω_{j0} now reads $\omega_j = \left(1 - \eta^2\right)^{1/4}$. Since this potential is periodic, here we just assume the phase particle is localized in a certain

interval, let say, $\varphi \in [0, 2\pi]$, within which, the local minimum is $\varphi_{min} = \sin^{-1}\eta$, while the local maximum is $\varphi_{max} = \pi - \sin^{-1}\eta$. The height of the potential well Δu is then defined by the potential difference between these two points, i.e.,

$$\begin{aligned}\Delta u &= u(\varphi_{max}) - u(\varphi_{min}) \\ &= 2\left[\sqrt{1-\eta^2} - \eta\cos^{-1}\eta\right] \\ &\approx \frac{4\sqrt{2}}{3}(1-\eta)^{3/2}, \;\; \eta \to 1\end{aligned} \tag{1.33}$$

in which, the second expression of Δu is obtained by taking Taylor expansion for the first expression near $\eta = 1$. It can be seen that as the increasing bias current I approaches the critical current I_c (or $\eta \to 1$), φ_{min} and φ_{max} will merge at $\varphi = \frac{\pi}{2}$, and the potential well gets flat, so that the phase particle in the well will certainly escape of the well and roll down along the potential surface (Figure 1.3). Thus, after crossing this maximum point, the phase and the phase derivative will increase dramatically, thus correspondingly, we say, the junction switches from the S state (aka zero-voltage state) to R state (finite-voltage state, "running state", "normal state", "rotation state"), for which, the current and voltage satisfies the Ohm's law, $V = IR$, or in normalized form, $\dot{\varphi} = \eta/\alpha$ (Figure 1.5), as we have mentioned in the last section.

In (1.29), the damping coefficient α that relates to the resistance not only stands for the dissipation of energy of the particle, but also plays a role of the media or coupling between the phase particle and "environment" or "heat bath", through which, the noise β feeds energy to the system so that thermal equilibrium can be established, while the variation of the bias current η characterizing the motion of the washboard potential well tends to break the equilibrium. The inverse of α has another name, called "quality factor", $Q \equiv \omega_{j0}RC$, which is the ratio of stored energy to dissipated energy in one cycle of oscillation. It is worth noting here, however, that the damping term α is just a parameter for the analogous phase particle or pendulum, instead of the junctions in reality; the value of α and its origin is always a chicken and egg problem in junctions. The Langevin equation (1.29) and the white noise properties (1.30a) and (1.30b) will be the basis of our discussion and calculation in the following chapters.

1.3.3 Average potential energy at $\eta = 0$

To solve the classical second-order differential equation (1.29) numerically, it is natural to ask what the initial conditions (φ_0, $\dot{\varphi}_0$) should be. In the following chapters, we will see if the bias current changes linearly with a constant rate $\dot{\eta}$ in time, that is, $\eta = \dot{\eta}\tau$, the system can be maintained in (or near) equilibrium state under high damping, $\alpha > \dot{\eta}$, and high temperature, $k_B T/E_{j0} > \hbar\omega_{j0}$ as $\eta \to 1$, and the information of the initial state of the phase particle will be wiped out; otherwise, it can be preserved (energy conserves).

That means, to consider the evaluation of the initial conditions, we just need to consider the case when the system is in non-equilibrium state. As we have seen, to have the phase particle escaped from the potential well, one could feed energy to the system by ramping up the bias current η, or by increasing the temperature with finite damping. Now let's take an extreme situation, in the absence of thermal fluctuation ($T = 0$) and extreme low damping ($\alpha \ll \dot{\eta}$), the thermal effect from the environment is gone, but the energy from the initial state is preserved since the RCSJ model described by (1.29) now becomes pure mechanical without dissipation, guaranteeing the switching takes place prior to the moment when the bias current reaches unity.

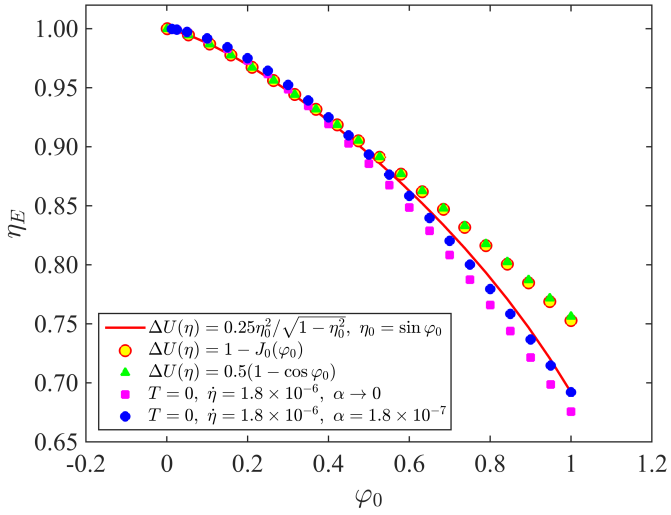

Figure 1.4. The relation between initial phase and escape current from different expressions, comparing with simulations. The red curve is from the average potential given in [42]; the green and yellow dots are from expressions (1.37) and (1.36), and the purple and blue dots stand for the simulation with $\dot{\eta} = 1.8\times10^{-6}$, $T = 0$, and $\alpha = \{0,\ 1.8\times10^{-7}\}$.

Initially, when $\eta = 0$ and assuming the oscillation is small near the bottom of the well, by

(1.31), the potential energy of the phase particle is

$$e_p = 1 - \cos\varphi \approx \varphi^2/2 \tag{1.34}$$

Based on the Virial theorem, the kinetic energy $\langle e_k \rangle = \frac{1}{2}\langle \varphi \partial_\varphi e_p \rangle = \langle e_p \rangle$. For a certain initial phase φ_0, the total energy stored in the junction given by (1.12) will be

$$\langle E_j \rangle / E_{j0} = 1 - \cos\varphi_0 = \langle e_k \rangle + \langle e_p \rangle \tag{1.35}$$

which gives the average potential energy

$$\langle e_p \rangle = \frac{1}{2}(1 - \cos\varphi) \tag{1.36}$$

On the other hand, for small-amplitude approximation, assuming $\varphi(t) = \varphi_0 \cos\omega t$, another expression for the average potential energy can be obtained as

$$\langle e_p \rangle = \frac{1}{T}\int_0^T [1 - \cos\varphi(t)]\, dt = 1 - J_0(\varphi_0) \tag{1.37}$$

where J_0 is the zero's order Bessel function of the first kind. This is equivalent to (1.36) under small φ_0. As a by-product, the average kinetic energy can be calculated by the Virial theorem:

$$\langle e_k \rangle = \frac{1}{2}\langle \varphi \partial_\varphi (1 - \cos\varphi) \rangle = \frac{\varphi_0}{2} J_1(\varphi_0) \tag{1.38}$$

where J_1 is the first's order Bessel function of the first kind. To verify (1.36) or (1.37), we can relate them to the height of the well (1.33), obtaining a relation between the initial phase angle φ_0 and escape current η_E. In Figure (1.4), we see that when φ_0 is small enough (< 0.5 rad), (1.36) is a good approximation comparing to the results from simulation, providing us a hint about how to determine the value of the initial phase for the Langevin simulation in the following chapters, i.e., if a value for the $\langle e_p \rangle$ is provided, then φ_0 is known.

1.3.4 The Current-Voltage Characteristics

The Current-Voltage (I-V) characteristics contains the information of the physical processes occurring in junctions. The influences from the bias current I and its changing rate $\dot{I}$, the resistance $R(\sim 1/\alpha)$, the magnetic field $\mathbf{B}$, temperature T, energy gap Δ_g, capacitance C, etc., can be reflected on the I–V characteristics. This was how Anderson [4] and Shapiro [5] respectively observed the DC and AC Josephson effects.

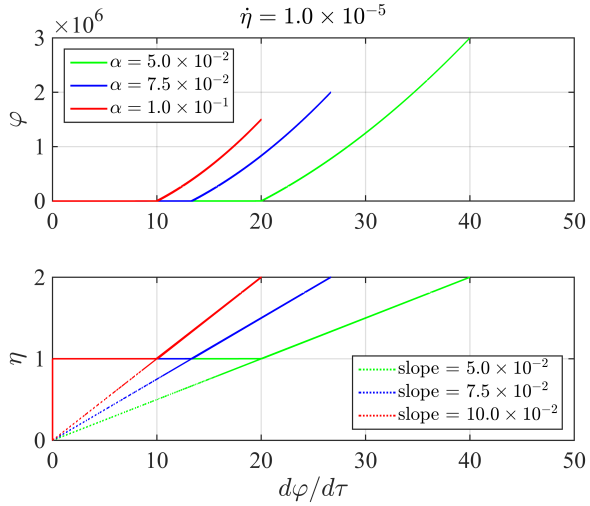

Figure 1.5. I-V curves for various damping coefficients (overdamped) with sweep rate $\dot{\eta} = 10^{-5}$. The curves are generated by solving the Langevin equation (1.29). After $\eta = 1$ the junction switches to normal state (running state), whose slope is exactly the normalized damping coefficient α.

If slowly increasing the bias current η from zero with a constant rate $\dot{\eta}$, one may see the voltage drop being zero initially but after the bias current gets to a critical value, $\eta = 1$ or $I = I_c$, the voltage then increases dramatically, indicating that the phase particle escaped from the well, or the junction has switched from S state to R state. Figure1.5 shows the normalized I-V curves ($\eta \sim \dot{\varphi}$) and the corresponding phase space ($\varphi \sim \dot{\varphi}$) under $T = 0$ and $\dot{\eta} = 10^{-5}$. Before the bias current η reaches one, the phase particle is trapped in the well with small oscillation; once the switching occurs around $\eta = 1$, the finite voltage can be seen and the slope, $\eta/\dot{\varphi} = \alpha$, implies that the current and voltage satisfies the Ohm's law, since based on the Josephson relations and the definition of the damping coefficient, $\alpha = \frac{\hbar\omega_{J0}}{2eI_cR}$, one has

$$\frac{V}{I} = \frac{\frac{\hbar\omega_{J0}}{2eI_c}\frac{d\varphi}{d\tau}}{I/I_c} = R\alpha\left(\frac{\dot{\varphi}}{\eta}\right) = R \tag{1.39}$$

in which, $\dot{\varphi} = \frac{d\varphi}{d\tau}$. It is worth noting here that, in general, the junction resistance R is not constant. It has different names corresponding to different states where the junction is. For example, the junction resistance in R state is "normal resistance", R_N; the resistance in S state is "effective resistance", R_{eff}. Some other also includes "subgap resistance" R_{sg}, "quasiparticle resistance" Rqp, etc. For instance, for some low-damping cases, the junction resistance was found to follow [19, 43, 44]:

$$R = R_0 \mathrm{e}^{\Delta/k_B T} \tag{1.40}$$

in which, Δ is energy gap, R_0 is a constant fitting parameter and T is temperature. This means the corresponding damping coefficient becomes $\alpha = \alpha_0 \mathrm{e}^{-\Delta/k_B T}$, where $\alpha = \frac{1}{\omega_{j0} R_0 C}$. In [45], however, the temperature-independent normal resistance R_N is considered to be the best to fit the MQT theory at low temperatures.

1.4 Escape rate theory of Brownian particle

Since the phase of the junction can be analogous to a Brownian particle moving in a washboard potential, the escape theory of Brownian particle may provide an angle of view for understanding the switching mechanism of Josephson junction. We will use the terminology for these two situations equivalently, e.g., the junction switches from superconducting (S) state to resistive (R)/normal state, corresponds to that the Brownian/phase particle escapes from the trap state to running state.

The Brownian particle in the well can escape ultimately due to thermal noise or random force exerting to the particle through the media characterized by the damping or dissipation term. In 1940, H.A. Kramers [15] derived the well-known simple expression of the escape rate, $\Gamma(t)$, of the Brownian particles escaping over a potential well for calculating a chemical reaction rate. The base of Kramers' escape theory is actually the Langevin equation (1.29), that yields an equivalent form as

$$\dot{v} = -\alpha v - \sin\varphi + \beta \tag{1.41}$$

$$\dot{\varphi} = v \tag{1.42}$$

where $v \equiv \frac{d\varphi}{d\tau}$. Since the property of the white noise β implies the motion of the Brownian particle is a Markov-Gauss stochastic process, hence, one can obtain a corresponding Fokker-Planck equation [15, 46] as

$$\partial_\tau \rho = -\partial_\varphi (v\rho) + \partial_v [(\alpha v + \sin\varphi - \eta)\rho] + \alpha k_B T \partial_v^2 \rho \tag{1.43}$$

in which, $\rho \equiv \rho(\varphi, v)$ is the phase-space density at energy E. Sometimes equation (1.43) can be expressed as an equivalent form in terms of position (φ) and momentum ($p = m\dot{\varphi}$), called

Klein-Kramers equation:

$$\partial_\tau \rho = \frac{du}{d\varphi}\partial_p \rho - p\partial_\varphi \rho + \alpha \partial_p (\rho p + k_B T \partial_p \rho) \tag{1.44}$$

where $u = 1 - \cos\varphi - \eta\varphi$ is the washboard potential (1.31) in the absence of noise term. Equation (1.44) was obtained by Kramers and then was used in many literature when studying the statistical properties and escape mechanism of a Brownian particles over a potential well [16, 30]. From the Klein-Kramers equation to the expression of escape rate Γ, the detailed derivation can be found in [47]. The idea is using the canonical transformation in Hamiltonian mechanics to transform the variable from (φ, p) to (E, w), where w is the angular variable. Then erasing w due to its fast variation results in the "energy control diffusion equation":

$$\partial_\tau \rho = \partial_I (\alpha \rho I + k_B T \alpha I \partial_E \rho) \tag{1.45}$$

in which, $I \equiv \oint p d\varphi$ is the action [48]. By the continuous equation $\partial_\tau \rho = -\partial_I J$, the phase flux J reads

$$J = -\alpha \rho I - k_B T \alpha I \partial_E \rho \tag{1.46}$$

where the first term on the right-hand side is the dissipation pulling the particle down to the local minimum of the well and the second term is due to thermal fluctuation that leads to a diffusion process driving the particle away from the minimum. If ρ is constant along constant E in the phase space and $J = 0$, then a thermal equilibrium or Boltzmann distribution will be set up: $\rho(E) = \rho_0 \mathrm{e}^{-E/k_B T}$, where ρ_0 is a constant of integration.

1.4.1 Kramers and BHL escape rates

Equation (1.45) was obtained by Kramers and in his work [15], he gave the most well-known and simplest close form for the escape rate in weak-damping limit:

$$\Gamma_K = \frac{\omega_j}{2\pi\omega_b}\left[\sqrt{\frac{\alpha^2}{4} + \omega_b^2} - \frac{\alpha}{2}\right] \mathrm{e}^{-\frac{\Delta U}{k_B T}} \tag{1.47}$$

$$\approx \begin{cases} \left(\frac{\alpha I_b}{k_B T}\right)\frac{\omega_j}{2\pi}\mathrm{e}^{-\frac{\Delta U}{k_B T}}, & \text{"}\textit{heavy damping}\text{"} \\ \frac{\omega_j}{2\pi}\cdot \mathrm{e}^{-\frac{\Delta U}{k_B T}}, & \text{"}\textit{weak damping}\text{"} \end{cases} \tag{1.48}$$

in which ω_j is the bias dependent resonant frequency given in (1.13); $\omega_b \equiv |U''(\varphi_b)|^2$, the frequency near the maximum of the potential $U(\varphi)$; ΔU, the height of the potential barrier

(1.33); k_BT, the Boltzmann energy of the phase particle. Kramers's escape rate was built up on several assumptions, including (1) the system is in equilibrium state and Maxwell-Boltzmann distribution holds, (2) the phase particle starts moving from the bottom and the height of the barrier is sufficiently large: $\Delta U \gg k_BT$; (3) the particle is not retrapped after escaping. Equation (1.48) is also a starting point for deriving an expression for the escape rate with flux theory [16, 49, 50]. In 1983, Büttiker, et al. [16] gave a damping-dependent form (BHL) as

$$\Gamma_{BHL} = \frac{\sqrt{1+\frac{4\xi k_BT}{\alpha I_b}}-1}{\sqrt{1+\frac{4\xi k_BT}{\alpha I_b}}+1}\left(\frac{\alpha I_b}{k_BT}\right)\left(\frac{\omega_j}{2\pi}\right)\mathrm{e}^{-\frac{\Delta U}{k_BT}} \tag{1.49}$$

where α is the normalized damping coefficient in equation (1.42); ξ is an adjustable parameter approximately equals to unity[2]; I_b is the action near the barrier peak, given by $I_b = 4.8E_{j0}\left[2(1-\eta)\right]^{5/4}$. The form of I_b is not unique; for example, for cubic potential approximation [52], $I_b = \frac{7.2\Delta U}{\omega_j}$, and for a harmonic oscillator having an almost periodic motion at the saddle point of the potential [15, 47], $I_b = \frac{2\pi\Delta U}{\omega_j}$. The Kramers escape rate is an approximation of the BHL escape rate under a large damping. In the following chapters they will be used as a reference of equilibrium state, comparing to the results from the reported experiments and those from our own simulations that numerically solve the Langevin equation (1.29).

1.4.2 The limitations of Kramers and BHL escape theories

Both of the Kramers and BHL escape rates successfully give an interpretation for the thermal activation of the Brownian particle escaping from a metastable potential well, providing a nice reference for the switching mechanism of Josephson junction in the past four decades. Two limitations should be reminded.

(1) *Fails to interpret the switching behaviours of the junction at low temperatures compared to the experimental data*. As the temperature-independence (saturation) phenomenon of the switching current distribution at low temperature ($k_BT \ll \hbar\omega_{j0}$) was first observed [20, 21] in 1981, the Kramers/BHL theory is considered no longer valid for the low-temperature regions. This is quite obvious since both of expressions (1.48) and (1.49) are carrying a Boltzmann factor k_BT, implying the distribution functions generated by these escape rates are also temperature

[2] In [51] it was suggested that for metastable potential (Fig.1.3), $\xi = 1.474$, and for symmetric double well, $\xi = 4.293$; the escape time should be doubled due to the halved probability to bounce back. Here, we just use ξ=1.

dependant. On the theory side, Caldeira and Leggett [25,26] proposed a model for the quantum Brownian particle motion, predicting at $T = 0$ K, the escape rate follows

$$\Gamma_{MQT} = a_q \left(\frac{\omega_j}{2\pi}\right) \mathrm{e}^{-7.2\frac{\Delta U}{\hbar\omega_j}\left(1+\frac{0.87}{Q}\right)} \tag{1.50}$$

where $a_q = 864\pi\Delta U/\sqrt{\hbar\omega_j}$; $Q \equiv \frac{1}{\omega_j RC}$ is the quality factor. For more details on the saturation of SCD and experimental results, please see Chapters 3 and 4.

(2) *Fails to give a correct SCD compared to the results of numerical methods (Langevin simulation) under a relatively low damping*. This has been emphasized by Kramers in his own work and a number of literature have tried give an improvement for the escape rate in the past eight decades, e.g., [16,32,49–51,53]. Since in this thesis we will use the Kramers/BHL escape rate as a reference, a comparison among the Kramers (1.48), BHL (1.49), and Langevin (1.29) simulations are plotted in Figure (1.6). The escape rate for Langevin simulation here is defined to be the inverse of the average lifetime of the particle in S state: $\Gamma_{Lan} = 1/\langle\tau_s\rangle$; the potential well is static, that is, for each dot on the plots, the bias current η is constant for each escape event. It can be seen that as the potential well gets shallower ($\eta \to 1$), at the given temperature $\theta = k_B T/E_{j0}$ and damping α as shown in (a), the Kramers/BHL follows the Langevin curve up to $\eta > 0.996$. However, as the temperature and damping increase for one order of magnitude as shown respectively in Figure 1.6 (b) and (c), the Kramers and BHL curves deviate from the Langevin curve. This makes sense since based on the definition of the escape rate in terms of lifetime, as $\eta \to 1$, $\tau_s \to 0$ so that $\Gamma \to \infty$, however, the Kramers and BHL escape rate approach a finite value instead.

On the other hand, in a typical Josephson junction switching experiments, the bias current is a function of time, continuously increasing in a sweep rate, i.e., $\eta = \dot{\eta}\tau$. The dynamically titling of the well will disturb the equilibrium built up by the dissipation and fluctuation. This raises a question that whether the Kramers/BHL theory can still hold under this condition, and if so, what the requirement should be. In Chapter 2, this can be answered by observing the switching current distribution. It is reasonable to expect that a requirement is that the speed of the motion of the well must be slow enough, so that when the thermal equilibrium can be re-built before the phase particle escape, i.e., $\alpha/\dot{\eta} < 1$ [52,54].

This phenomenon is attributed to the failure of the Kramers/BHL theory in the description

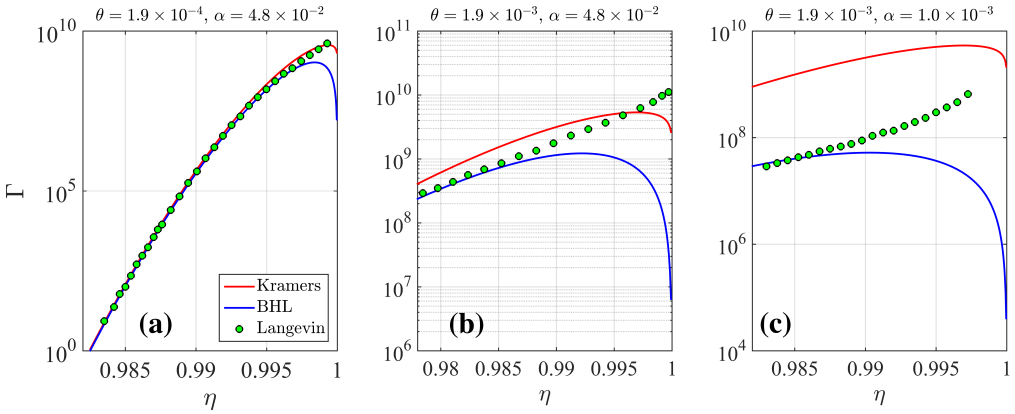

Figure 1.6. Comparison among the escape rates of Kramers, BHL and Langevin simulations. The horizontal axis is the normalized bias current, and the normalized temperature and damping coefficient are shown on the top of each plot.

of the non-equilibrium effect of the system; as the external bias current approaches unity, the potential well gets shallower so during this process, some non-equilibrium effects take place, such as the so-called "finite-barrier effect". [31, 50, 52, 55]. We also have a discussion on this issue [56], however, in the present thesis, the Kramers/BHL theoty is merely for providing a reference for the equilibrium state, and the point of the note above is for emphasizing the importance of the damping-sweep ratio $\alpha/\dot{\eta}$ in the following chapters.

1.5 Conclusion

In this chapter we present some historical and physical backgrounds of Josephson junction. In terms of RCSJ model, the phase variable of the junction is governed by the Langevin equation (1.29), which allows the switching problem of Josephson junction to be analogous to a Brownian particle escaping from a washboard potential. This means that besides numerically solving the Langevin equation, one can also discuss the switching problem with the existing escape theory of Brownian particle, e.g., the Kramers and BHL escape rates theories. On the other hand, some other properties of the Langevin equation, including the washboard potential well, average potential energy, current-voltage relation, etc. are presented. At the end of this chapter, the limitations of the Kramers and BHL escape rates are also mentioned.

Chapter 2

Non-equilibrium Transient Phenomena

This chapter will dedicate to discuss some non-equilibrium transient phenomena reflected from the *switching current distribution (SCD)* where the switching mechanism of the junctions is encoded. On the theory side, the *thermal activation (TA)*, together with *macroscopic quantum tunneling (MQT)*, currently provide a complete interpretation for the switching mechanism for the Josephson junctions. In this chapter, we will focus on the former - the analogous phase particle driven by the thermal noise as the bias current ramps up gets close to the critical current I_c ($\eta = 1$) crosses over the potential barrier, resulting in the escape (switching of junctions) from trap state (zero-voltage state, S state) to running state (finite-voltage state, R state). In the absence of noise, the phase particle will escape at $\eta = 1$ where the potential well becomes flat, while the existence of the thermal noise will lead to early escape, forming a switching/escape distribution (SCD) at $\eta \lesssim 1$.

In this chapter, the non-equilibrium transient phenomena will be presented and the effects of the parameters that appear in the Langevin equation (1.42), including the damping, temperature, initial conditions, sweep rate, will be investigated. The discussion in this chapter has been published in [54]. Based on the understanding on the escape mechanism under non-equilibrium state, in the following chapters, we will be able to perform further discussion on the "saturation" phenomenon observed in experiments.

2.1 Method: Construction of SCD Peaks

The dynamics of the phase particle moving in the tilting potential well, especially near the barrier when the well is very shallow, is very complex, due to the highly nonlinearity of the governing equation, the tilting motion of the potential well, the existence of noise, etc. For instance, conventional methods, such as perturbation approach [57], which gives an escape rate obtained from the corresponding one-dimensional Fokker-Planck equation versus nearly conserving energy rather than spatial coordinate, are always approximate, and will lead to deviation from experiments under low temperature and low damping limit; in some situations, the interaction between chaos and noise may increase the spectral linewidth by almost an order of magnitude [58]. Fortunately, however, the switching current distribution that reflects the statistics of the escape event has some nice and stable properties that could be easily visualized or measured, so the SCD has become one of the most important tools for the investigation. In experiments and numerical simulation, SCD is a histogram constructed by many switching events; the horizontal axis is the bias current and the vertical axis is the count or probability density of how many switching events dropping in the intervals of bias current. Measuring the position and width, or other characteristics of the shape of the distribution can provide us information on the switching mechanism.

In *experiments*, starting from the zero-voltage state (S state) of the junction, the bias current as an input or force term, is ramped up slowly and linearly at a constant rate of $\frac{dI}{dt}$ (or $\dot{\eta} = \frac{d\eta}{d\tau}$) until the junction switches to the finite-voltage state (R state), where the output voltage signal is detected proportional to the input external bias current. The current at the moment when the switching occurs is recorded as I_{sw} and the junction is then reset. Usually the input bias current is a periodic saw-tooth wave with a certain repetition frequency, and between two neighboring ramps, there is a waiting time. The rate of ramping up $\dot{\eta}$ is therefore called the *sweep rate* of the bias current. To reduce the statistical uncertainty, this process is usually repeated $M = 10^4 \sim 10^5$ times so a histogram or switching distribution of the ensemble of junctions is acquired from the set of $\{I_{sw}\}$. Measuring the mean and standard deviation of all I_{sw} provide us the information of the peak position and peak width under a certain temperature; a position curve ($\langle I_{sw} \rangle \sim T$) and a width curve ($\sigma_{sw} \sim T$) then can be plotted.

In *numerical simulation*, the Langevin equation (1.29) given in Chapter 1:

$$\ddot{\varphi} + \alpha\dot{\varphi} + \sin\varphi = \dot{\eta}\,\tau + \beta(\tau)$$

is discretized and solved using the GJF algorithm provided in Ref. [59]. It has been shown that the improved GJ algorithm is able to produce accurate configurational and kinetic statistics in Langevin simulations even for large time step size within the stability limit of the Verlet algorithm [60,61], and this good property enables us to simulate those experiments with extreme low sweep rate. Letting the normalized time be τ, the discrete-time variables are introduced as $r_n = \varphi(\tau_n)$ and $v_n = \dot{\varphi}(\tau_n)$, the GJF scheme reads

$$r_{n+1} = r_n + b\Delta\tau_n\left(v_n + \frac{\Delta\tau}{2}f_n + \frac{\beta_{n+1}}{2}\right) \tag{2.1a}$$

$$v_{n+1} = av_n + \frac{\Delta\tau}{2}(af_n + f_{n+1}) + b\beta_{n+1} \tag{2.1b}$$

$$u_{n+\frac{1}{2}} = \frac{r_{n+1} - r_n}{\sqrt{b}\Delta\tau} \tag{2.1c}$$

in which, $\Delta\tau = \tau_{n+1} - \tau_n$, $a = \frac{1-\alpha\Delta\tau/2}{1+\alpha\Delta\tau/2}$, $b = \frac{1}{1+\alpha\Delta\tau/2}$, $f_n = -\sin r_n$; $u_{n+\frac{1}{2}}$ is the half-step velocity at $\tau_{n+\frac{1}{2}}$, which guarantees correct kinetic statistics; the integrated thermal fluctuation $\beta_{n+1} = \int_{\tau_n}^{\tau_{n+1}}\beta(\tau')d\tau'$ relates to the damping α and temperature $\theta = k_BT/E_{j0}$ as $\beta_n = \sqrt{2\theta\alpha\Delta\tau}\cdot\sigma_n$, where σ_n is a Gaussian random number generated by the "*ran2()*" random number generator given in [62], satisfying

$$\langle\sigma_n\rangle = 0 \tag{2.2a}$$

$$\langle\sigma_m\sigma_n\rangle = \delta_{mn} \tag{2.2b}$$

in which, δ_{mn} is the Kronecker delta with integers $m,\ n$. At $\tau_0 = 0$, the phase particle starts moving near the bottom of the well $\varphi = 0$ with an initial condition $\{\varphi_0, \dot{\varphi}_0\}$ and simultaneously, the bias current is increased with the rate of $\dot{\eta}$ until the phase particle escapes out of the potential well at η_E. The signature for a single escape event taking place is $\varphi > \varphi_m = \pi - \sin^{-1}\eta$, where φ_m is the local maximum of the potential. From Fig.1.5 we can see that after the phase particle crosses over the barrier, it starts rolling down and enters the running state, so the derivative of phase (voltage), $\dot{\varphi}$, starts shooting up, having a proportional relationship with η. Hence, besides monitoring whether the phase φ gets larger than φ, another criterion applied in the simulation

for an escape event is that $\dot{\varphi}$ reaches a finite value, and here we take $\dot{\varphi} > 1$. Similar to experiment, computing the mean and standard deviation of $\{\eta_E\}$ allows to plot the position curve ($\langle\eta_E\rangle \sim \theta$) and a width curve ($\sigma_E \sim \theta$), where $\theta = k_B T/E_{j0}$ is the normalized temperature. To reduce the uncertainty, the number of escape event is taken $M = 10^4$ and the time step size is $\Delta\tau = 0.02$, if not specified.

The third approach to construct a SCD peak is based on the theoretical knowledge on the escape mechanism of the phase particles, namely, *escape rate,* Γ, which is defined as the inverse of the life-time (τ) of the zeros-voltage state, i.e., $\Gamma \equiv 1/\tau$. Once the escape rate Γ is known, the switching current distribution function $P(I)$ can be obtained as [37]

$$P(I) = \Gamma(I)\left(\frac{dI}{dt}\right)^{-1}\left[1 - \int_0^I P(I')dI'\right] \tag{2.3}$$

where I is the current and the distribution function $P(I)$ is normalized to unity. To perform the calculation numerically, expression (2.3) needs to be discretized [63]. Assume the bias current is swept from 0 to I_c and this range is divided into N interval uniformly; in the n^{th} interval, e_i out of the total number of M junctions switch (or phase particles escape). From (2.3) it can be seen that the number of particles dropping in an interval is proportional to the escape rate $\Gamma(I)$, the duration time Δt in that interval, and the number of remaining phase particles that haven't escaped, thus, the number of escaped phase particle in each interval is as follows:

$$\begin{aligned} e_1 &= \Gamma(I_1)\Delta t M \\ e_2 &= \Gamma(I_2)\Delta t\,(M - e_1) \\ &\cdots \\ e_n &= \Gamma(I_n)\Delta t\left(M - \sum_{i=1}^{n-1} e_i\right) \end{aligned} \tag{2.4}$$

Assuming the bias current increases with a constant rate $\dot{I} = \frac{dI}{dt}$, the duration time in each interval is $\Delta t = T/N = \frac{\int_0^{I_c} dI}{\dot{I}N} = \frac{I_c}{\dot{I}N}$, where T is the total time required for a phase particle to escape starting from $t = 0$. It is worth noting that $\{e_i\}$ is a histogram that satisfies $\sum_{i=1}^N e_i = M$ or $\sum_{i=1}^N \left(\frac{e_i}{M\Delta I}\right)\Delta I = 1$, which, as $\Delta I \to 0$, becomes $\int_0^{I_c} P(I)dI = 1$. This implies the distribution given in (2.4) under $\Delta I \to 0$ can go back to the original one in (2.3).

In this chapter, the damping-dependent BHL escape rate given by expression (1.49), i.e.,

$$\Gamma_{BHL} = \frac{\sqrt{1+\frac{4\xi k_B T}{\alpha I_b}}-1}{\sqrt{1+\frac{4\xi k_B T}{\alpha I_b}}+1}\left(\frac{\alpha I_b}{k_B T}\right)\left(\frac{\omega_j}{2\pi}\right)\mathrm{e}^{-\frac{\Delta U}{k_B T}}$$

will be used as a reference for the equilibrium state of the ensemble. Here we take $\xi = 1$ and $I_b = 4.8E_{j0}\left[2(1-\eta)\right]^{5/4}$.

2.2 Results: Observation of non-equilibrium effects

In this section, the non-equilibrium transient phenomena occurring in the washboard potential will be presented. Transient state is a state of a system approaching steady state under effect of fluctuation and dissipation. A Brownian particle moving in a heat bath mimicked by damping and thermal noise, will reach thermal equilibrium within a certain transient time. For the phase particle discussed in Josephson terms, however, it also subjects to an external force or bias current due to the titled potential well. Since the position of the minimum of the well is $\varphi_{min} = \sin^{-1}\eta$, taking derivative yields the velocity of the phase $\dot{\varphi}_{min} = \frac{\dot{\eta}}{\sqrt{1-\eta^2}}$. This implies even for a constant sweep rate, the minimum of the well moves toward $\varphi = \pi/2$ with an acceleration, which tends to delay the time of reaching equilibrium, having the transient time extended. To get to the equilibrium within the same transient time, a higher damping will be required; if the phase particle failed to reach the equilibrium state prior to the escape of the potential well, this information would be encoded by the switching/escape current.

2.2.1 Effect of sweep rate

The sweep rate $\dot{\eta}$ reflects the speed of the motion of the potential well. Figure 2.1 shows the simulated probability density ρ for the escape events with $\dot{\varphi}_0 = 0$ and $\alpha = 10^{-4}$; the bias current η ramps up with sweep rate $\dot{\eta}$ linearly from zero according to $\eta = \dot{\eta}\tau$. Figure 2.1(a) shows a standard switching distribution obtained for $\dot{\eta} = 5\times10^{-4}$ and $\varphi_0 = 0$. Figure 2.1(b) is under the same sweep rate with Figure 2.1(a), but an non-zero initial phase, $\dot{\varphi}_0 = \pm 0.2$, is imposed; for this case, peaked distributions are observed. From (a) to (b), it is reasonable to say that this resonant feature is triggered by the initial condition that induces the oscillation at the beginning of the tile of the well, and the distributions with positive and negative values of

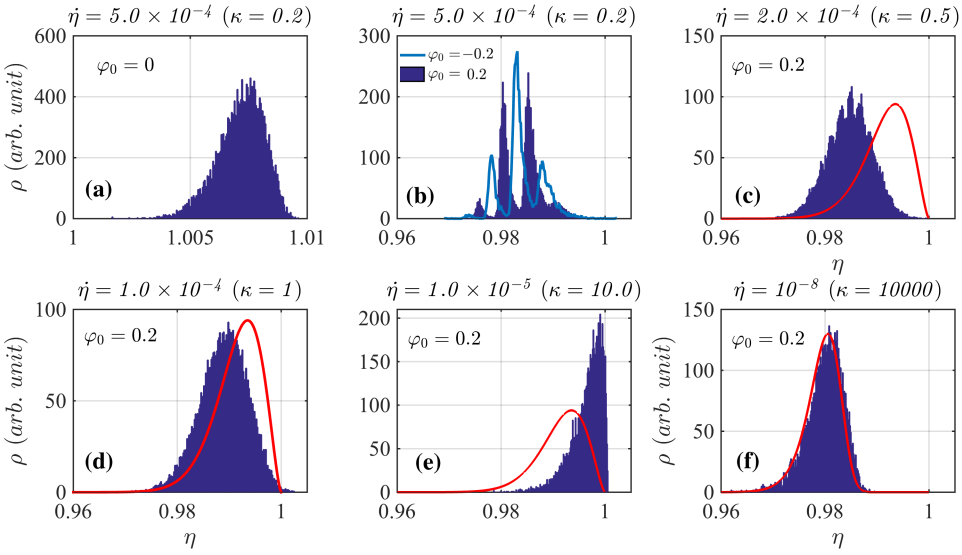

Figure 2.1. Simulated probability density distributions of escape from the potential well as the tilt is increased from $\eta(0) = 0$. Parameters are $\dot{\varphi} = 0$, $\alpha = 10^{-4}$, and normalized temperature $\theta = k_B T / E_{j0} = 10^{-3}$. The specific parameters for the subplots are (a) $\dot{\eta} = 5 \times 10^{-4}$ and $\varphi_0 = 0$; (b) $\dot{\eta} = 5 \times 10^{-4}$ and $\varphi_0 = \pm 0.2$; (c) $\dot{\eta} = 2 \times 10^{-4}$ and $\varphi_0 = 0.2$; (d) $\dot{\eta} = 10^{-4}$ and $\varphi_0 = 0.2$; (e) $\dot{\eta} = 10^{-5}$ and $\varphi = 0.2$, and (f) $\dot{\eta} = 10^{-8}$ and $\varphi = 0.2$. κ is the ratio of damping to sweep rate, $\alpha / \dot{\eta}$. The number of escape events is $N = 10^4$. The red curve is generated by the BHL escape rate theory with the same parameters

the initial phase would be complementary to each other, i.e., peaks becomes valley, vice versa. From Figure 2.1 (d) to (f), the sweep rate is lowered from $\dot{\eta} = 2 \times 10^{-4}$ to 10^{-8}, while the initial phase is $\varphi_0 = 0.2$ and the other parameters are unchanged. The peaked features gradually become insignificant as the ratio of damping to sweep rate $\kappa = \alpha / \dot{\eta}$ approaches unity. When κ gets to 10^4, the switching distribution agrees well with the BHL curve, which indicates the ensemble has been in equilibrium state. To demonstrate the relation between the peaked feature and oscillation of the particle, we plot the $\varphi \sim \eta(t)$ curves in Figure 2.2, which corresponds to Figure 2.1 (a) (b) and (e) but the temperature is set to zero in order to exclude the effect of fluctuation. The parameters for each case is as shown in the plots. The black dash curve stands for the position of the local minimum; when it crosses the trace of the oscillation (blue and red), the phase particle escapes out of the well and enters the running state. It can be seen that when the initial phase is zero so that the oscillation is not induced, or when the damping is larger than sweep rate so the particle is over-damped - as long as the oscillation dies out at the moment when the particle escapes, the peaked distribution won't show up. In fact, when $\kappa = 1$, the

multi-peaks have been invisible. On the other hand, in Figure 2.2(a), one might have noticed that the the escape distribution of the phase particle is located outside of $\eta = 1$, where the well has disappeared. This can be explained by Figure 2.2 (a), in which, the red line goes beyond $\eta = 1$ as well. Due to the inertia of the non-oscillating phase particle and the fast-moving minimum of the potential ($\dot{\varphi}_{min} = \dot{\eta}/\sqrt{1-\eta^2}$) near $\eta = 1$, the instant when the particle starts rolling down could be later than the moment when potential well gets flat at $\eta = 1$.

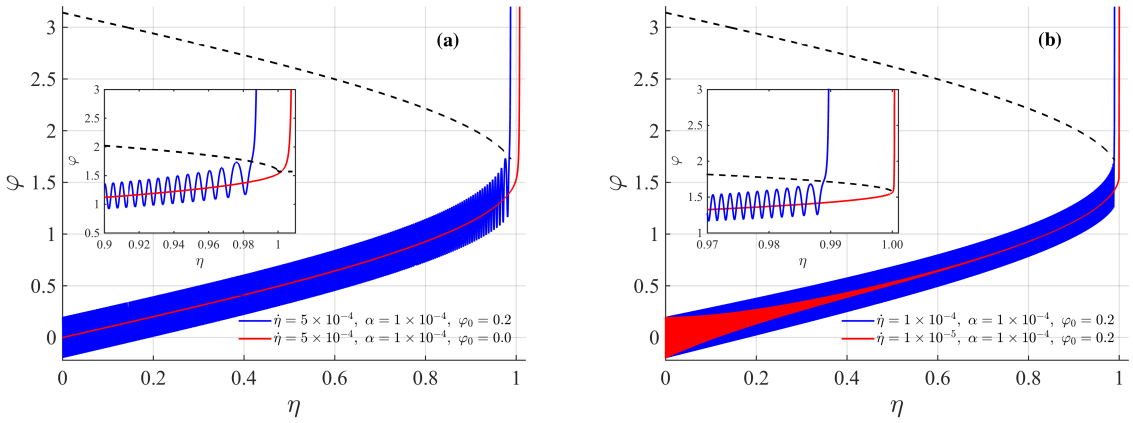

Figure 2.2. The bias current (time) dependent oscillation of the phase corresponding to Figure 2.1 (a) (b) and (e), but the normalized temperature $\theta = k_B T/E_{j0}$ is set to 0. In (a) the blue and red curves have the same sweep rate ($\dot{\eta} = 5 \times 10^{-4}$) and damping ($\alpha = 10^{-4}$), while the initial phase are respectively $\varphi_0 = 0.2$ and 0. In (b), the red and blue curves share the same damping and initial phase, but the sweep rate of the red one is 10^{-5}, 10 times lower that the blue. The dash curve stands for the position of the maximum of the potential, $\varphi_{max} = \pi - \sin^{-1}\eta$, and the inset is the zoomed-in plot showing the oscillation near $\eta = 1$.

Thus, up to here, we have a first impression for the multi-peak feature, that is, non-zero initial phase (oscillation for inducing resonant) and small value of κ (under-damped and fast-moving potential well, so $\kappa = \alpha/\dot{\eta} \leq 1$) might be the sufficient conditions for the appearance of the peaked distribution, which implies the ensemble of escape particles is in non-equilibrium state since it doesn't match the BHL one. However, the absence of multi-peaks doesn't mean it is not in non-equilibrium state, because the invisibility of the multi-peaks might be due to the low resolution or small spacing between the peaks (caused by slow sweep). In experiments, multi-peak feature was reported in late 1990s [64, 65] as an evidence of the existence of energy levels quantization in underdamped Josephson junctions under high sweep rate. However, here we can see the multi-peaks can be a result of classical resonant induced by the oscillation and

fast sweep in under-damped condition.

2.2.2 Effect of damping

The linear damping term, $\alpha\varphi$, on the left-hand side of the Langevin equation (1.29) mimics the media of the heat bath, and the thermal noise β exerts its influence to the particle through it. In reality, α could be more complex. For example, it can be the function of temperature as we have seen in Chapter 1. On the other hand, it is dissipation of energy. For a particle oscillating in a potential well with a friction force $f = -\alpha\dot{x}$ (x is a Cartesian coordinate), the energy varies as $I(t) = I(0)\mathrm{e}^{-\alpha t/m}$, where m is the mass of the particle, α is damping, I is the action defined as $I \equiv \oint pdq/2\pi$ with position q and momentum p [48]. Above we have seen that the ratio $\alpha/\dot{\eta}$ may play a key role in determining the state of the escape phase particle. Here we analyze the effect of the damping α on the switching/escape current distributions. With the same numerical method, in Figure 2.3 the parameters are $\dot{\eta} = 10^{-5}$, $\varphi_0 = 0.2$, $\dot{\varphi}_0 = 0$, and $\theta = k_B T/E_{j0} = 10^{-3}$. It is clear that when the damping α is near 10^{-9}, i.e., 10000 times lower than the sweep rate, the peaked distribution is observed; as α increases, the spacing of the peaks is unchanged, but the widening of each peak diminishes the resolution. This is because the noise term $\beta \propto \sqrt{\alpha}$, the increase of the magnitude of the noise can higher the standard deviation of the peaks, filling up the spacing in between. When $\alpha = 10^{-8}$, the multi-peak feature has been invisible. Again, in (e), we can see at $\alpha/\dot{\eta} = 1$, the distribution is still on the way to the agreement with the BHL curve, and until this ratio gets sufficiently high by 10^4 in plot (f), the escape distribution agrees perfectly with the BHL curve.

Similar to Figure 2.3, Figure 2.4 represents the escape distributions but under a slightly lower sweep rate, $\dot{\eta} = 10^{-6}$. For this case, although α is down to 10^5 times smaller than the sweep rate, the multi-peaks are still insignificant due to low resolution (low sweep rate). At $\alpha = 0.1$ or $\alpha/\dot{\eta} = 10^5$, the distribution matches the BHL curve. On the other hand, from Figure 2.3 and 2.4, one might have noticed that when the ratio $\alpha/\dot{\eta} \ll 1$, the positions of the center of distribution look approximately at $\langle\eta_E\rangle \sim 0.973$. A guess about this number is, it might relates to the initial phase and/or temperature that these two figures share, and for an extremely low temperature case, the escape distribution should depend on the former only. It is also found that relating expressions (1.33) and (1.36), i.e., $2(\sqrt{1-\eta^2} - \eta\cos^{-1}\eta) = 0.5(1-\cos\varphi_0)$, resulting

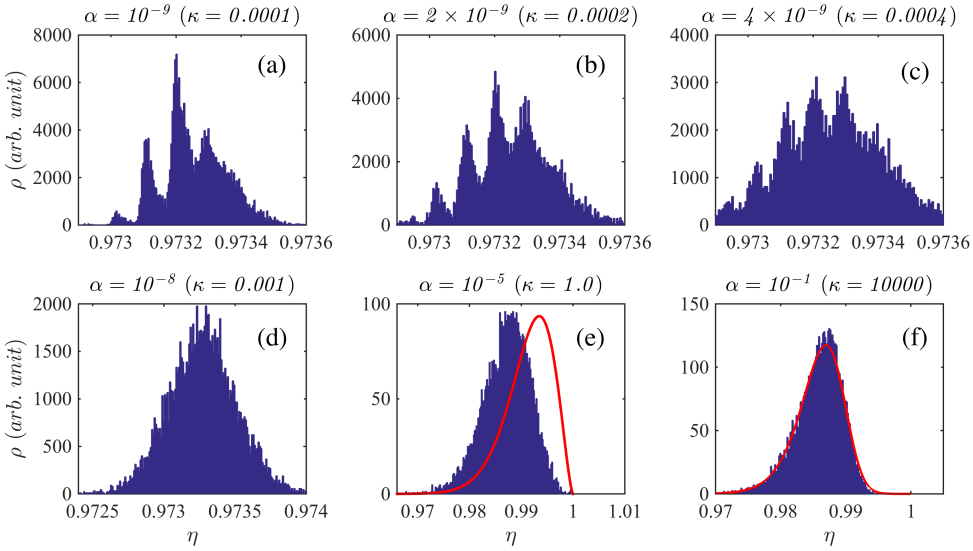

Figure 2.3. Escape distribution for various values of damping. For all subplots, $\dot{\eta} = 10^{-5}$, $\varphi_0 = 0.2$, $\dot{\varphi}_0 = 0$, and $\theta = k_B T/E_{J0} = 10^{-3}$; the damping parameter α is varied from 10^{-9} to 10^{-1} as shown together with the corresponding ratio $\kappa = \alpha/\dot{\eta}$. The number of escape events is $N = 10^4$. The red curve is the theoretical prediction by the BHL theory with the same parameters.

in a solution, which is $\varphi_0 = 0.970$, having percentage error of 0.34%. This indicates that when the damping and temperature are absent, η_E is purely initial-phase dependent as we guess. In the following discussion we can see that this phenomenon is one of the characteristics of non-equilibrium state due to $\alpha/\dot{\eta} < 1$, for which, the memory on the initial perturbation is encoded by the escape current η_E. Once the oscillation induced by the initial perturbation is gradually wiped out by the noise due to the increasing temperature and/or damping, the escape distribution will approach the BHL curve, matching which is a sufficient condition of equilibrium state [see Figure 2.4 (e) and (f)].

Figure 2.5 represents damping dependence of the peak positions and widths of the escape distributions extracted from Figure 2.4 but with more damping parameters that vary from 10^{-10} to 10^{-1}. Since under the sweep rate $\dot{\eta} = 10^{-6}$, even if the ensemble is in non-equilibrium, no multi-peaks can be observed, so it is meaningful to measure the position and width of a single peak in the SCD as the experiments did. It shows that $\alpha = 10^{-6}$, i.e., $\alpha/\dot{\eta} = 1$ is a watershed for these two curves. For the peak position curve (blue), as α is down to 10^{-8}, a flattening is observed and keeping lowing the α won't change the peak position, while the width gets

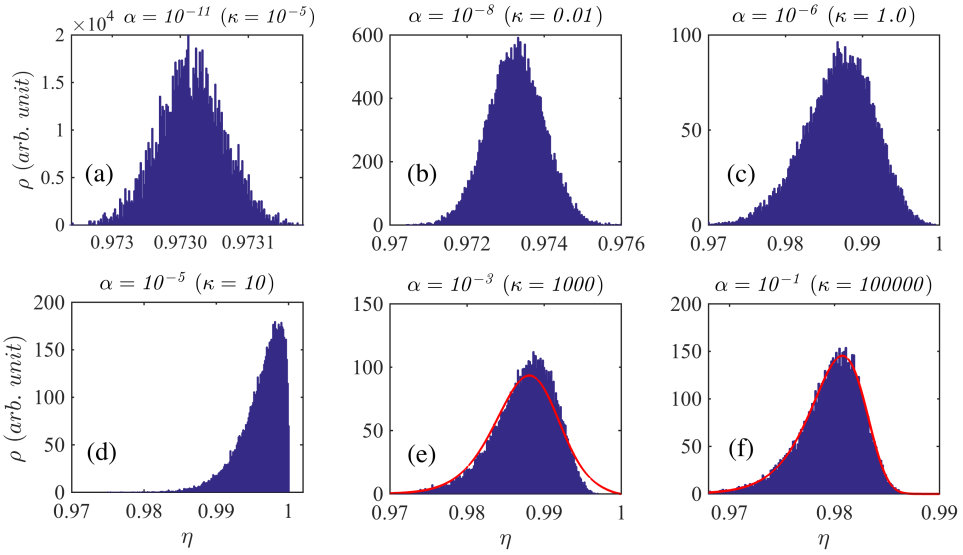

Figure 2.4. Escape distribution for various values of damping. The parameters are $\dot{\eta} = 10^{-6}$, $\varphi_0 = 0.2$, $\dot{\varphi}_0 = 0$, and $\theta = k_B T/E_{j0} = 10^{-3}$; α is varied from 10^{-7} to 10^{-1} and $\kappa = \alpha/\dot{\eta}$ is the corresponding ratio. The number of escape events is $N = 10^4$. The red curve generated by the BHL escape theory.

narrower and no flattering is seen. In this regime, the phase particle is extremely under-damped and the noise term is so weak that the oscillation induced by the initial condition still survives even dominant over the fluctuation, and finally determines the SCD. This is why the width of SCD approaches zero since at this point, it depends only on the initial phase, $\varphi = 0.2$, whose width or standard deviation, however, is zero. Around $\alpha = 10^{-6}$ $(\alpha/\dot{\eta} = 1)$ with increasing α, the peak positions keep moving toward $\eta = 1$ until reaching a maximum, where the width curve gets to a valley. In Figure 2.4 (d) it can be seen that the peak moves to the right, but can not cross $\eta = 1$, since the phase particles have escaped out of the well and its escape current has been record as one; thus, the distributions are squeezed until the damping gets sufficiently large so that the distribution starts moving back toward the left (the direction of decreasing η) due to the increasing noise term that provides energy for the early escape. After the maximum of the position curve and the valley of the width curve around $\alpha = 10^{-5}$ $(\alpha/\dot{\eta} = 10)$ are reached, the peak keeps moving away from $\eta = 1$, while the width recovers to normal (not squeezed) and decreases again due to the increasing damping that results in increasing energy loss. We see again as the damping α gets larger than the sweep rate, the influence from initial condition is gradually wiped out; after a short period of the transient state around $\alpha = 10^{-5}$, the thermal

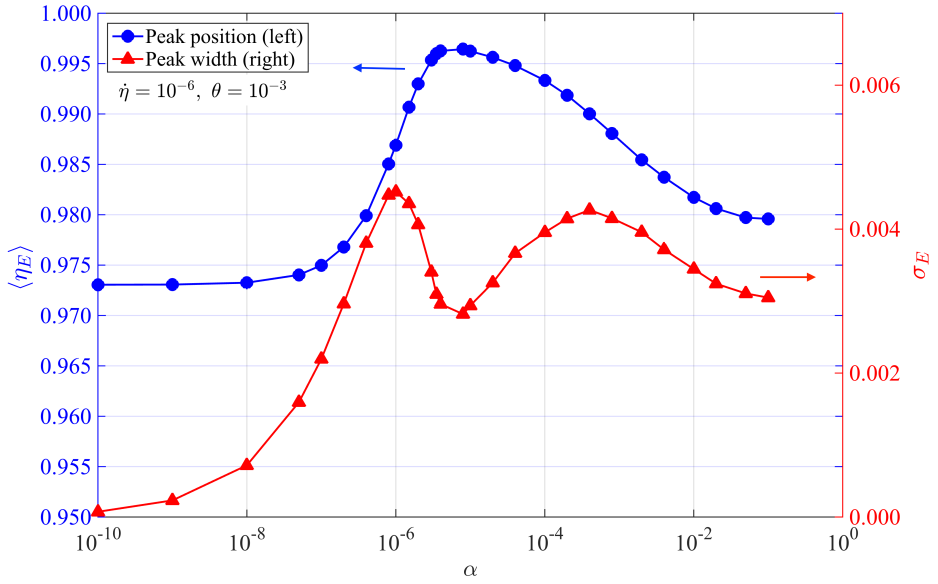

Figure 2.5. Peak position and width of the escape distributions extracted from Figure 2.4 but with more damping parameters. The left vertical axis stands for the peak position $\langle \eta_E \rangle$ with blue color, and the right vertical axis is for the peak width σ_E with red color; the horizontal axis stands for the various damping parameters α. The temperature is $\theta = 10^{-3}$ and the initial condition is $\varphi_0 = 0.2$ and $\dot{\varphi}_0 = 0$.

noise becomes dominant, becoming the main factor that triggers the escape of the particle.

2.2.3 Effect of temperature

Temperature shows up in the noise term on the right-hand side of the Langevin equation (1.29), determining the strength of the noise together with the damping: $\beta \propto \sqrt{\alpha k_B T}$. Besides tilting the potential well or increasing the bias current to higher the potential energy of the phase particle, increasing temperature is another way to pump energy into the system through exerting the random impact to the phase particle from the noise. This enables the particle to overcome the potential barrier at a certain instant when the well is still deep. This escape mechanism is called "thermal activation (TA)". Hence, it is naturally expected that given constant damping coefficient α, a higher temperature can make the particle escape from the potential well earlier, and as a result, the escape distribution moves toward the direction of decreasing η.

This idea is shown in the left plot of Figure 2.6, in which, the parameters are $\dot{\eta} = 10^{-6}$, $\alpha = 0.05$, $\varphi_0 = 0.2$ and $\dot{\varphi}_0 = 0$. We can see in the left plot that when the normalized temperature is $\theta = 10^{-4}$, the phase particle escapes slightly lower than $\eta = 1$, where the potential well nearly

gets flat, while as the temperature is increased, the peak position moves to the left, meaning that the particle escapes from the well earlier than the bias current reaching the critical current as expected. Meanwhile, the peak width gets wider as the temperature gets higher, and this makes sense because the distribution is spanned due to the strength of the noise, and increasing temperature means increasing the strength, resulting in a larger width of SCD. The ratio of damping to sweep for this case is $\alpha/\dot{\eta} = 50000 \gg 1$, implying the ensemble based on the specific parameters above is in equilibrium state; this is why the result from simulation agrees well with the BHL theory. We extract the data from the left plot of Figure 2.6 (but adding more cases) and show the position and width curves in Figure 2.7, which gives us a big picture for the temperature dependence of the SCD peak position and width. This plot is a standard form for showing the escape (switching) mechanism of the phase particle (Josephson junction). The only escape mechanism here is thermal activation, thus, as the temperature approaches zero, the width gets narrower, approaching zero as well, and the particle can only escape until the well gradually gets flat at $\eta = 1$. However, this is not consistent with what we will see in the experiments and we will discuss it in the following chapters.

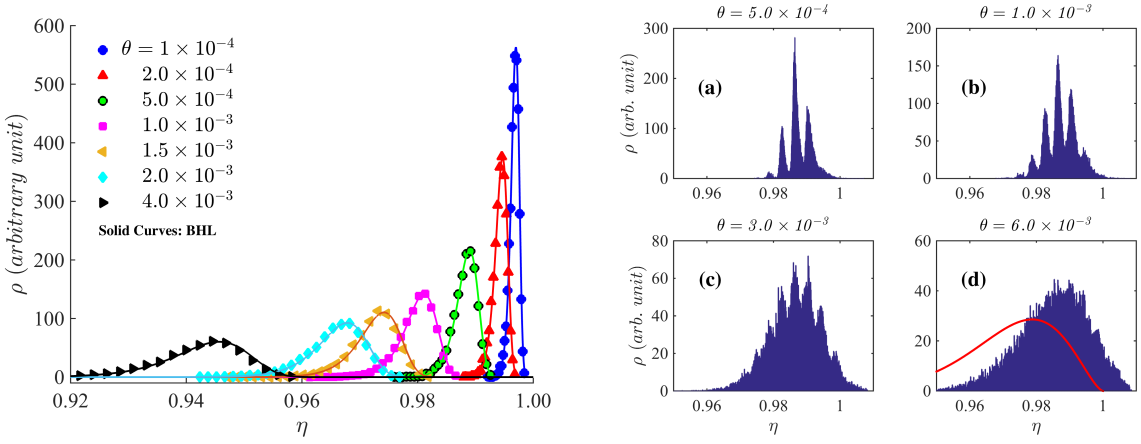

Figure 2.6. Escape distribution for equilibrium (left) and non-equilibrium (right) states. For the distributions on the left plot, the parameters are $\dot{\eta} = 10^{-6}$, $\alpha = 0.05$, $\varphi_0 = 0.2$ and $\dot{\varphi}_0 = 0$; the normalized temperature $\theta = k_B T/E_{j0}$ is varied from 10^{-4} to 4×10^{-3}; the dots stand for the data from Langevin simulation, and the solid curves are generated by the escape rate of the BHL theory. For the plots (a)$\sim$(d) on the right-hand side, the parameters are $\dot{\eta} = 4 \times 10^{-4}$, $\alpha = 2 \times 10^{-4}$, $\varphi_0 = 0.2$ and $\dot{\varphi} = 0$; the temperature is varied from $\theta = 5 \times 10^{-4}$ to 6×10^{-3}.

Above we discussed the temperature dependence of the peak properties in equilibrium state. Now let's see what if the ensemble is in non-equilibrium state. In the right plot of Figure 2.6,

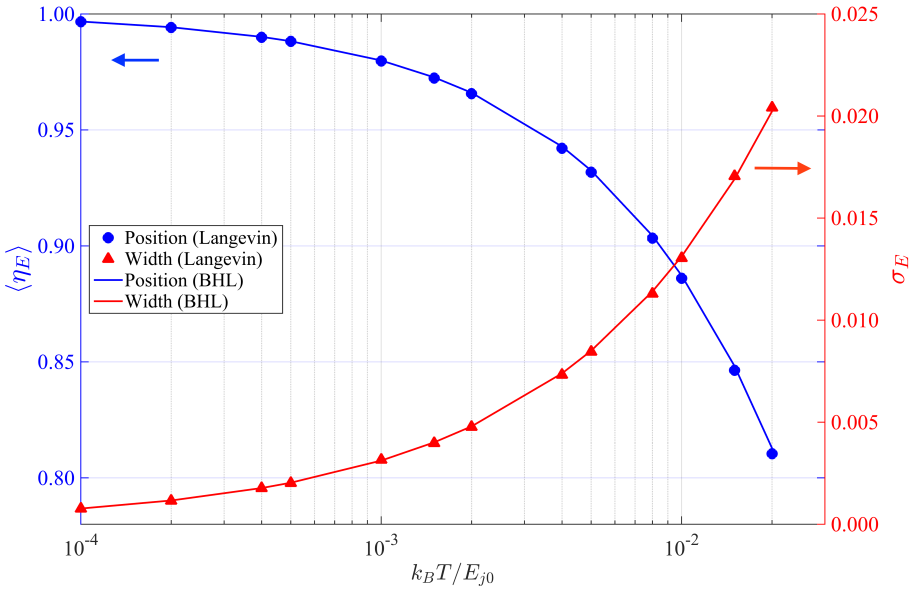

Figure 2.7. Peak position and width curves for the left plot in Figure 2.6 (includes more cases). The blue color stand for the peak position scaled with the left vertical axis (blue); the red color stand for the peak width scaled with the right vertical axis (red). The horizontal axis is the normalized temperature. The dots corresponds the data from Langevin simulation while the solid curves are generated by the BHL theory.

the fast sweep rate is applied ($\dot{\eta} = 10^{-4}$) and the damping α is set to 2×10^{-4}, so that the ratio is $\alpha/\dot{\eta} = 0.5 < 1$, which guarantees the ensemble is in non-equilibrium state. The initial condition is $\varphi_0 = 0.2$ and $\dot{\varphi}_0 = 0$ and four distributions under various normalized temperatures $\theta = \{5, 10, 30, 60\} \times 10^{-4}$ are presented. Again, peaked distribution is observed, and it is found that under this setting, increasing temperature won't change the main body of the multi-peak structure and the position of the entire distribution, but will fill up the space between the multi-peaks and enlarge the width of the entire distribution. When the temperature gets sufficiently high, the multi-peak structure vanishes, as shown in (d) of the right plot, in which, the red curve corresponds to the distribution generated by the BHL theory. The deviation between Langevin simulation and BHL curve indicates the failure of the BHL for describing a non-equilibrium state. That is, under a damping lower than the sweep rate, the initial energy given by $\varphi_0 = 0.2$ is dominant over the thermal energy from the noise; the medium characterized by the damping is not dense enough to establish the thermal equilibrium, regardless of the change of the temperature in the present range. In consequence, as what we see, the position of the

main body of the distribution is determined by the initial phase only.

2.2.4 Effect of initial conditions

Solving the Langevin equation (1.29) requires initial conditions, which in the previous sections, were set to $\dot{\varphi}_0 = 0$ and $\varphi_0 = constant$. In the case of very under-damping, this initial energy determines the magnitude of the oscillation of the particle. However, it can be wiped out by sufficiently large dissipation and/or noise. Anyways, besides bias current and temperature, initial condition is the third way to provide energy for the particle in the potential well. On the other hand, we have seen that the ratio of damping to sweep rate, $\alpha/\dot{\eta}$, is a characteristic quantity for determining whether the initial conditions are still having influence on the escape statistics.

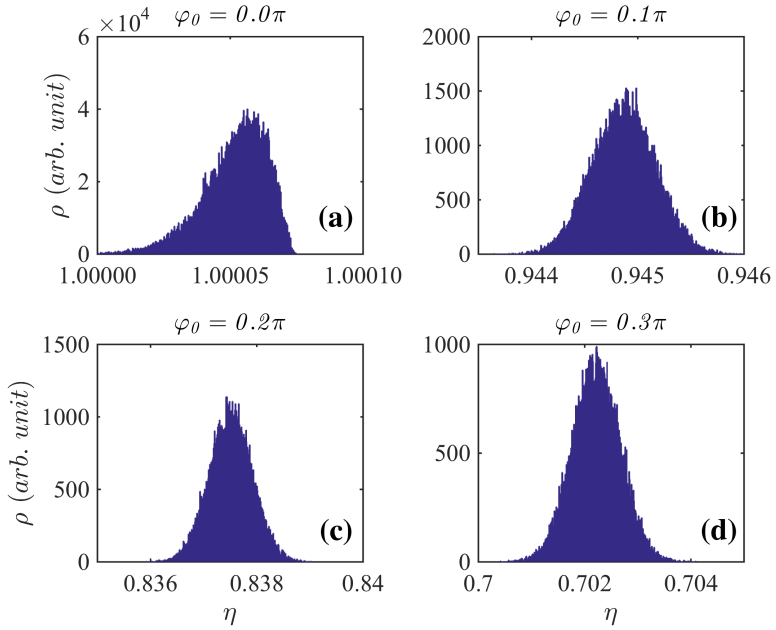

Figure 2.8. Escape distributions under various initial conditions. The initial phase φ_0 is set to $\{0,\ 0.1\pi,\ 0.2\pi,\ 0.3\pi\}$. The other parameters are $\dot{\varphi}_0 = 0$, $\dot{\eta} = 10^{-6}$, $\alpha = 10^{-9}$ and $\theta = k_B T/E_{j0} = 10^{-3}$.

Figure 2.8 shows the case for $\alpha/\dot{\eta} = 10^{-3} \ll 1$. The ensemble is in non-equilibrium state, although the sweep rate is low ($\dot{\eta} = 10^{-6}$) so the multi-peaks are insignificant under this resolution. The point is, however, as the value of the initial phase φ_0 increases from 0 to 0.3π, the escape distribution moves to the direction of decreasing η. This is consistent with the observation of Figure 2.6 (left), which shows a higher temperature can shift the distribution to

the downstream of η, that is, more (initial or thermal) energy the particle has, earlier can the particle escape out of the potential well.

Figure 2.9 shows the case for $\alpha/\dot{\eta} = 10^4 \gg 1$ with high damping $\alpha = 0.01$. The excellent agreement between Langevin simulation and BHL theory indicates thermal equilibrium has been established. As anticipated, the large dissipation wipes out the information from the initial disturbance, or say, the thermal energy from the noise dominates over the initial energy; thus, as long as the temperature remains constant, the peak position and width remain unchanged.

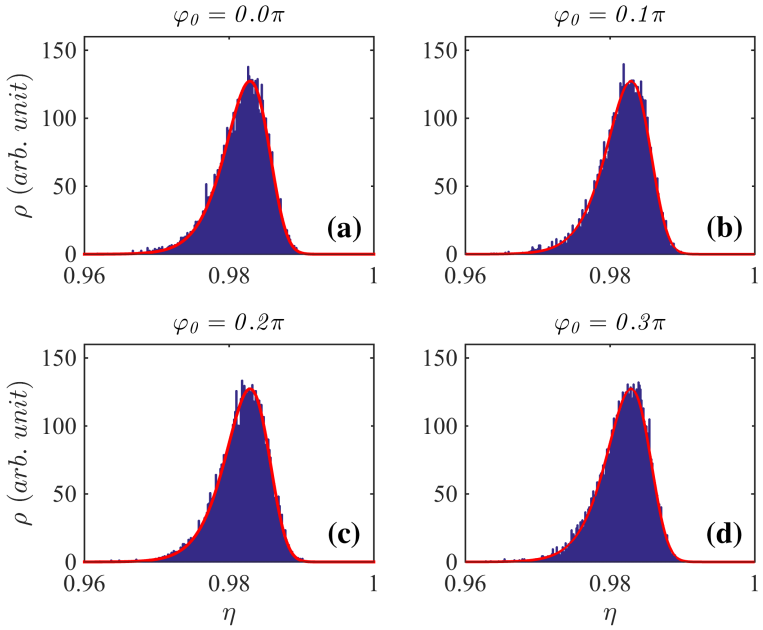

Figure 2.9. Escape distributions under various initial conditions. The initial phase is $\varphi_0 = \{0,\ 0.1\pi,\ 0.2\pi,\ 0.3\pi\}$. The other parameters are $\dot{\varphi}_0 = 0$, $\dot{\eta} = 10^{-6}$, $\alpha = 10^{-2}$ and $\theta = k_B T/E_{j0} = 10^{-3}$. The red curves are the escape distribution functions generated by the BHL theory.

Figure 2.10 provides another angle of view for the relations among the initial conditions, temperature and damping-sweep-ratio. Since the input η is actually a periodic saw-tooth wave - in each period, η linearly ramps up and then is reset after a particle escapes, we can draw a Poincare map[1] and observe the "competition" between initial energy (from initial conditions) and thermal energy (from noise) by checking φ and $\dot{\varphi}$ at the same point η. In Figure 2.10 section, the section is taken at $\eta = 0.5$ and then the trajectory of the particle is reset following

[1] In Figure 2.10 are actually "pseudo-Poincare maps", since the trajectory is reset when each particle escapes in a period.

the reset of the bias current. The initial conditions are $\varphi_0 = 0.2$ and $\dot{\varphi}_0 = 0$. In (a), the ratio is $\alpha/\dot{\eta} = 10^{-4}$, so the system is very under-damped. For a pure mechanical system with $\alpha = \theta = 0$, one can expect that the motion of the particle is periodic and on the map it would be a single point. Here, with low but non-zero dissipation, when the temperature is $\theta = 10^{-5}$, the trajectory spreads (red) and forms an circular arc, while $\theta = 10^{-3}$ (blue), it has been a close path. Both of these two trajectories are located on a circle with radius of 0.2, implying that oscillations are quasi-periodic and the energy of the phase particle given from φ_0 is almost conserved. In (b), the damping equals to the sweep rate ($\alpha/\dot{\eta} = 1$). For $\theta = 10^{-5}$ (red), the circular trajectory shrinks, meaning a portion of initial energy has been dissipated. For $\theta = 10^{-3}$ (blue), a significant dispersion of the trajectory on the map can be observed, although the oscillation still looks regular. In (c), the oscillations become totally chaotic, and the trajectories on the map is dependent only on the Gaussian noise. Higher temperature will produce larger the area of dispersion or amplitude of the oscillation.

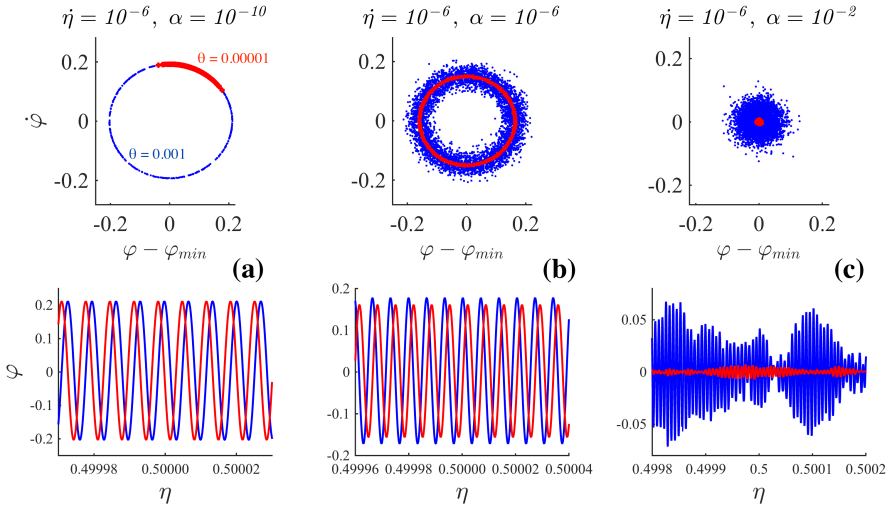

Figure 2.10. Pseudo-Poincare maps and oscillations (time domain) under various temperatures and $\alpha/\dot{\eta}$. The sweep rate for (a), (b), and (c) are 10^{-6} and initial conditions are $\varphi_0 = 0.2$ and $\dot{\varphi}_0 = 0$; the damping $\alpha = 10^{-10}$, 10^{-6} and 10^{-2} respectively. The blue color represents normalized temperature $\theta = 10^{-3}$ and the red color is for $\theta = 10^{-5}$. In the three subplots at the top, the Poincare section is taken at $\eta = 0.5$, and the three subplots at the bottom are the corresponding oscillations of the phase particle in time domain.

It is worth noting that the initial phase could be a distribution, instead of a single value φ_0. For instance, due to the existence of thermal noise, both of φ_0 and $\dot{\varphi}_0$ follow a Gaussian

distribution, namely, thermal distribution, which centered at zero but has a standard deviation of $\sqrt{k_B T/E_{j0}}$. Or it is possible that φ_0 follows a certain distribution, such as thermal distribution or uniform distribution, but $\dot{\varphi}_0$ is determined by the constrain $E = \varphi_0^2/2 + \dot{\varphi}_0^2/2$, where the constant E is the total initial energy of the phase particle. Figure 2.11 (a)∼(d) show the comparison of the escape distributions with distributed/non-distributed initial conditions. The damping-sweep ratio is set to be $\alpha/\dot{\eta} = 0.25$, so that the peaked feature is visible. In (a), the initial phase is a single value $\varphi_0 = 0.2$, while (b) and (c) respectively use uniform and Gaussian distributions centered at 0.2 as shown on the top of each subplots. The temperature for (d) is zero, while for others $\theta = 10^{-3}$. Comparing (a) to (b), (c) and (d), it seems that distributed initial phase may generate more peaks so reducing the spacing. For all cases, the positions of the entire distributions looks the same; the reason is, since $\alpha/\dot{\eta} < 1$, as we have seen in the previous sections, the ensembles are in non-equilibrium state, so the position of distribution only depends on the value of initial phase φ_0; here, similarly, it depends on the center of initial phase $\langle\varphi_0\rangle$. Comparing (c) to (d), which is for $T = 0$, we see temperature only fills up the space between the peaks but doesn't change its basic structure.

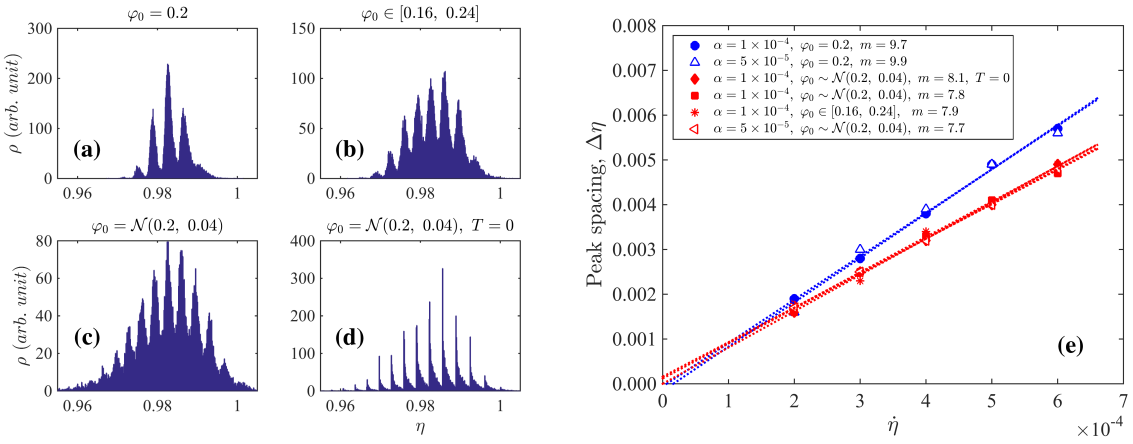

Figure 2.11. Comparison of the escape distributions with distributed/non-distributed initial conditions. For all subplots, the parameters are $\dot{\eta} = 4 \times 10^{-4}$, $\alpha = 10^{-4}$ and $\dot{\varphi}_0 = 0$; the temperature is $\theta = 10^{-3}$, except for (d), where $T = 0$. Specifically, for (a), $\varphi_0 = 0.2$; for (b), the initial phase is chosen uniformly in the interval $[0.16,\ 0.24]$ that also centered at 0.2; for (c), φ_0 follows Gaussian distribution centered at 0.2 with standard deviation being 0.04; (d) has the same setting as (c), but setting $T = 0$. (e) demonstrates the factors that determine the spacing between the multi-peaks. The red/blue color respectively stands for the distributed and non-distributed initial phases. The parameters are shown on the plot.

We measure the peak spacing of distributions similar to those in (a)∼(d), but consider more cases and show the results in Figure 2.11 (e). The parameters can be found in the legend of the plot. The red and blue color respectively stands for distributed and non-distributed initial phases. We can see the peak spacing $\Delta\eta$ between each small peaks in a single distribution is proportional to the sweep rate (affecting the resolution of the peaked distribution, as seen above), and the same type (distributed or non-distributed) of initial phase will produce a straight line with the same slope, that is, only the sweep rate and the type of initial condition can affect the spacing, while damping and temperature are not effective factors.

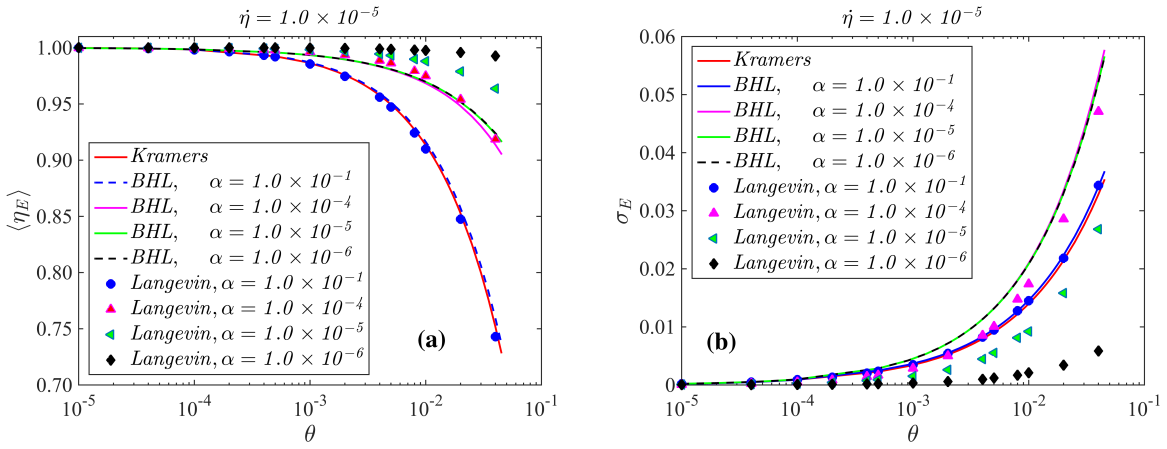

Figure 2.12. Comparison of the results of Langevin and Kramer/BHL simulations. Plots (a) and (b) respectively present the temperature ($\theta = k_B T/E_{j0}$) dependence of the peak position and width. The sweep rate is $\dot{\eta} = 10^{-5}$ and the initial conditions for Langevin simulatin are $\varphi_0 = \dot{\varphi}_0 = 0$. The dots stands for the results from Langevin simulation and the curves are generated by the Kramers/BHL escape rate. The various values of damping coefficient are shown in the legend.

2.3 Limitations of Kramers and BHL escape theory (continued)

In the previous chapter, we have seen the ratio $\alpha/\dot{\eta}$ is a criterion for distinguishing the state of the system in performing Langevin simulation, and we will see here that this ratio also plays the important role in the Kramers/BHL simulation, which is built up on the assumption of equilibrium state. Hence, if the value of $\alpha/\dot{\eta}$ is down to less than one, that means, as we observed in this chapter, the system would be away from equilibrium and one should be able to see the failure of the Kramers/BHL theory. In Figure 2.12, we compare the curves of peak

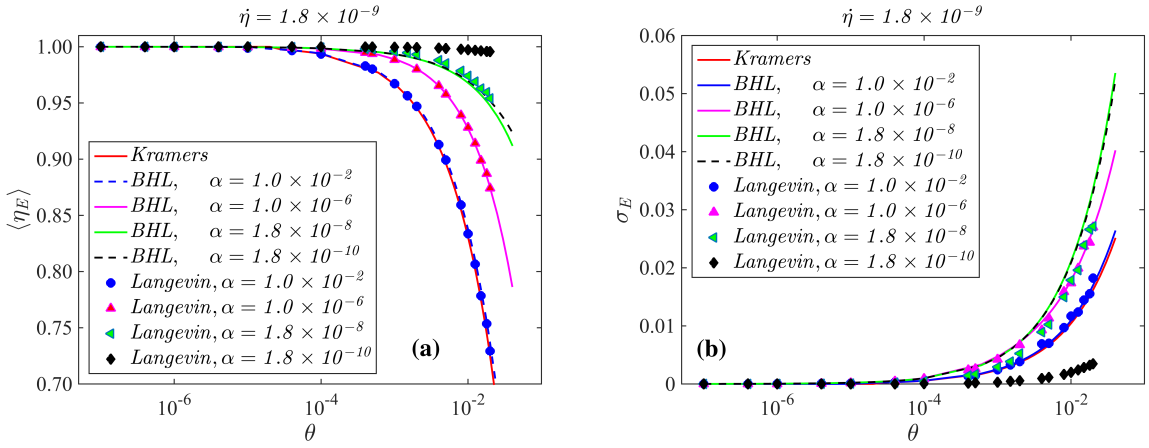

Figure 2.13. Comparison of the results of Langevin and Kramer/BHL simulations. (a) and (b) respectively present the temperature dependence of the peak position and width for $\dot{\eta} = 1.8 \times 10^{-9}$. The initial conditions for the Langevin simulation are $\varphi_0 = \dot{\varphi}_0 = 0$.

position and width from the Langevin and Kramers/BHL simulations for sweep rate $\dot{\eta} = 10^{-5}$, and specifically, for the Langevin one, the initial conditions are $\varphi_0 = \dot{\varphi}_0 = 0$. It can be seen that all of the results agree well to each other at low temperatures; for the case of large damping, the results of Kramers, BHL and Langevin simulations are basically identical. However, as the damping gets smaller, obviously, the Kramers fails first since it doesn't contain any damping term in its expression of the escape rate and only works for large damping as mentioned in Chapter 1, while the BHL follows the Langevin ($\alpha = 10^{-4}$) until the ratio $\alpha/\dot{\eta}$ gets closer to one; after that, e.g., for $\alpha = 10^{-5}$, the BHL curves have been significantly deviated from the Langevin ones. In Figure 2.13, the settings are the same as Figure 2.12 except for the sweep rate, which is lowered to $\dot{\eta} = 1.8 \times 10^{-9}$. We can see that for this time, the BHL works well even when the damping is very low, $\alpha = 10^{-8}$, and gets worse after crossing $\alpha/\dot{\eta} = 1$ as expected. Figure 2.13 shows that this deviation of the BHL/Kramers escape rate from the accurate Langevin simulation doesn't depend on the damping α solely, but on the ratio of damping to the sweep rate, $\alpha/\dot{\eta}$. Therefore, a necessary condition for safely performing the BHL/Kramers simulation is $\alpha \gg \dot{\eta}$. Fortunately, in the typical swithing experiments, the values of damping are sufficiently large (see Table 4.1).

2.4 Conclusion

In this chapter, we investigated the effects of the parameters, including sweep rate, damping, temperature and initial conditions, in the Langevin equation (1.29) on the escape/switching distribution, where the escape information of the phase particle is encoded. It was found that the escape statistics has two distinct properties, corresponding to, namely non-equilibrium and equilibrium states. The damping-sweep ratio $\alpha/\dot{\eta}$, which characterizes the competition between the damping and bias current, or, thermal effect and initial perturbation, plays a key role as a boundary between these two states. When $\alpha/\dot{\eta} \gg 1$, the ensemble of phase particles is in equilibrium state, and a sign is the good agreement of the results of the Langevin simulation and the BHL/Kramers escape theory, which is based on equilibrium-state assumption. In this case, the thermal energy dominates over the energy given from the initial perturbation, thus the peak position and width of the escape distribution is temperature dependent. On the other hand, when $\alpha/\dot{\phi} < 1$, the ensemble is in non-equilibrium state, the sufficient condition of which is the peaked escape distribution. It should be emphasized, however, that the peak feature is observable only under fast sweep, but it doesn't mean it doesn't exist for lower sweep ($\dot{\eta} < 10^{-5}$), since the spacing between depends on sweep rate $\dot{\eta}$ - when it is low, the peak feature will become invisible due to the issue of resolution, but we would say the ensemble is still in non-equilibrium state, as long as $\alpha/\dot{\phi} < 1$. For this case, the position and width of the escape distribution is almost temperature independent, since the initial energy dominates over thermal energy due to the too low damping, i.e, the position and width of the escape distribution are determined by the initial condition.

This observation on non-equilibrium state of the escape statistics provides us a new angle of view to understand the escape/switching mechanism of the phase particle/Josephson junction in low damping and low temperature. In the next chapter, we will further analyze the effect of initial condition on the escape statistics, and see if it is possible to reproduce some phenomena observed in experiments.

Chapter 3

Saturation Phenomenon in Switching Current Distribution

In experiments, saturation or "flattening" phenomenon is one of a characteristics of the escape/switching current distribution (SCD) in low temperature regime, where the peak position and width of SCD become temperature independence. Any theory only based on "thermal activation" (TA) seems to fail to describe this property of Josephson junctions; to resolve this problem, the theory of "macroscopic quantum tunneling" (MQT) was proposed [25,26]. Nowadays, when reading literature on switching experiments on Josephson junction, one may see the theoretical curves of peak position and width of SCD consist of two parts - for high temperature regime, the curve is generated by thermal activation, and at low temperatures, it is produced by MQT (e.g., Fig.2 in Ref. [66] and Fig.1 in Ref. [67]). The temperature corresponding to intersection of the TA and MQT curves is called "crossover temperture", T_{cr}, which distinguishes two different kinds of switching mechanisms, characterized by two quantities - $\hbar\omega_{j0}$ and k_BT; roughly speaking, lower than T_{cr}, the former will be dominant.

We noticed this is similar to the competition between the initial energy and thermal energy that we saw in the last chapter - when the damping-sweep ratio $\alpha/\dot{\eta}$ is lower than 1, the ensemble of the phase particles is in non-equilibrium state, and the position and width of the distribution depends on the initial condition. In this chapter, our objective is to reproduce a "saturation" phenomenon similar to those observed in experiments, according to the understanding on non-equilibrium state of the ensemble of phase particles. This is a prepared chapter for the

next one, where we will propose a classical model to produce switching current distribution that agrees well with the published experimental data. The contents of this chapter has been published in [42].

3.1 Methods

The same as in Chapter 2, the tool for the analysis is numerically solving the normalized Langevin equation using the GJ algorithm. Here we just briefly mention the basic ideas and more details can be found in the first section of Chapter 2. The normalized Langevin equation is given by (1.29)

$$\ddot{\varphi} + \alpha\dot{\varphi} + \sin\varphi = \eta + \beta$$

where φ is the phase difference between the two superconductors of a Josephson junction; α is the damping coefficient; η is the normalized external bias current, and β is the thermal noise term, whose discrete form is given as $\beta_n = \sqrt{2k_BT\,\alpha\Delta\tau/E_{j0}}\cdot\sigma_n$, where σ_n is a Gaussian random number generated by the "ran2()" algorithm from [62] and satisfies

$$\langle\sigma_n\rangle = 0 \tag{3.1a}$$

$$\langle\sigma_m\sigma_n\rangle = \delta_{mn} \tag{3.1b}$$

where δ_{mn} is the Kronecker delta with integers $m,\ n$. On the other hand, the Kramers or BHL will be also used as a reference for equilibrium state, for which, the escape rates are respectively given by expressions (1.48) and (1.49). Perticulary, the Kramers escape rate reads $\Gamma_{Kr} = f_j\cdot \mathrm{e}^{-\frac{\Delta U}{k_BT}}$, where $f_j = \frac{\omega_j}{2\pi}$ is the plasma frequency of the junction and $\Delta U = 2E_{j0}(\sqrt{1-\eta^2} - \eta\cos^{-1}\eta)$ is the depth of the potential well. The algorithm for generating the escape current distribution based on escape rate has been given by (2.4).

3.2 Further investigation for initial condition

In Chapter 2, the effect of initial condition has been analyzed. Here we focus on the the low-temperature regime, where the "saturation" phenomenon may appear.

3.2.1 Dependence of escape current upon initial phase for zero temperature and zero damping

Let's first consider a simplest case in the limit of $\alpha,\ T \to 0$. Given the temperature-independent peak position and width of the escape distribution under $\alpha/\dot{\eta} < 1$, we assume there exist a limit for each of the position and width as $\alpha,\ T \to 0$. This means the dissipation and noise terms in the Langevin equation (1.29) are dropped and the problem now becomes purely mechanical. Since the non-zero initial phase φ_0 ($\dot{\varphi}_0 = 0$) is equivalent to an initial energy, which is assumed to be given by the average potential energy $\langle e_p \rangle$ present in Chapter 1 and shallows the depth of the well. Hence, the expression for ΔU in (1.33) has to modified as

$$\Delta u_e = 2\left(\sqrt{1-\eta^2} - \eta \cos^{-1}\eta\right) - \langle e_p \rangle \tag{3.2}$$

$$\approx \frac{4\sqrt{2}}{3}(1-\eta)^{3/2} - \langle e_p \rangle,\ \ \eta \to 1 \tag{3.3}$$

where $\langle e_p \rangle$ is given by Equation (4) of Ref. [42] or equation (1.36) as an approximation for small φ_0 (Figure 1.4):

$$\langle e_p \rangle = \frac{\eta_0^2}{4\sqrt{1-\eta_0^2}} \tag{3.4}$$

$$\text{or}: \quad \langle e_p \rangle \approx \frac{1}{2}(1-\cos\varphi_0),\ \ \varphi_0 \to 0 \tag{3.5}$$

where $\eta_0 = \sin\varphi_0$ and φ_0 is the initial phase. Now we can see, due to the existence of this portion of initial energy, when the effective potential well gets flat so the phase particle can escape, the bias current has not reached $\eta = 1$, thus, letting $\Delta u_e = 0$ gives a solution η_E, which can be treated as the approximate escape current η_E for $\alpha,\ T \to 0$. Figure 3.1 (a) shows the dependence of the escape current on initial phase with sweep rate $\dot{\eta} = 10^{-7}$ under variation of damping α at $T = 0$. The same as we have seen in Chapter 2, a larger initial phase may make the particle escape earlier. Here, the red curve is the estimated η_E by solving for η_E from $\Delta u_e(\eta) = 0$. As we can see that the curve of estimated η_E agrees well with the simulation data for $\alpha \ll \dot{\eta}$ and $\varphi_0 < 1$, which is much larger than the calculated φ_0 from the literature on experiments. This oversimplified model gives us a good approximation for the escape current in the limit of $\alpha,\ T \to 0$ if the initial energy is known.

On the other hand, if the relation between the two variables, η_E and φ_0, is known by taking the approximate closed forms in expressions (3.3) and (3.5), as

$$\varphi_0 = \cos^{-1}\left[1 - \frac{8\sqrt{2}}{3}(1-\eta)^{3/2}\right] \tag{3.6}$$

and if the initial phase is some distribution, then the distribution for the escape current, $P_\eta(\eta)$, can be derived. Assuming the initial phase is a Gaussian distribution satisfying

$$P_\varphi(\varphi) = \frac{1}{\sqrt{2\pi}\sigma_{\varphi_0}} \mathrm{e}^{-(\varphi-\varphi_0)^2/2\sigma^2} \tag{3.7}$$

where φ_0 and σ_{φ_0} are respectively the mean (center) and standard deviation (width) of the distribution of the initial phase, and according to the relation between two random numbers, $P_\eta(\eta) = -P_\varphi[\varphi(\eta)] \cdot \varphi'(\eta)$, we have

$$P_\eta(\eta) = \frac{3}{\sqrt{\pi}\sigma_{\varphi_0} \cdot \sqrt{3\sqrt{2(1-\eta)} - 8(1-\eta)^2}} \mathrm{e}^{-\frac{\cos^{-1}\left[1-\frac{8\sqrt{2}}{3}(1-\eta)^{3/2}\right]-\varphi_0}{2\sigma_{\varphi_0}^2}} \tag{3.8}$$

That is, if the initial distribution of the phase P_φ is given, then the escape distribution (SCD) is known as well, under the limit of $\alpha,\ T \to 0$.

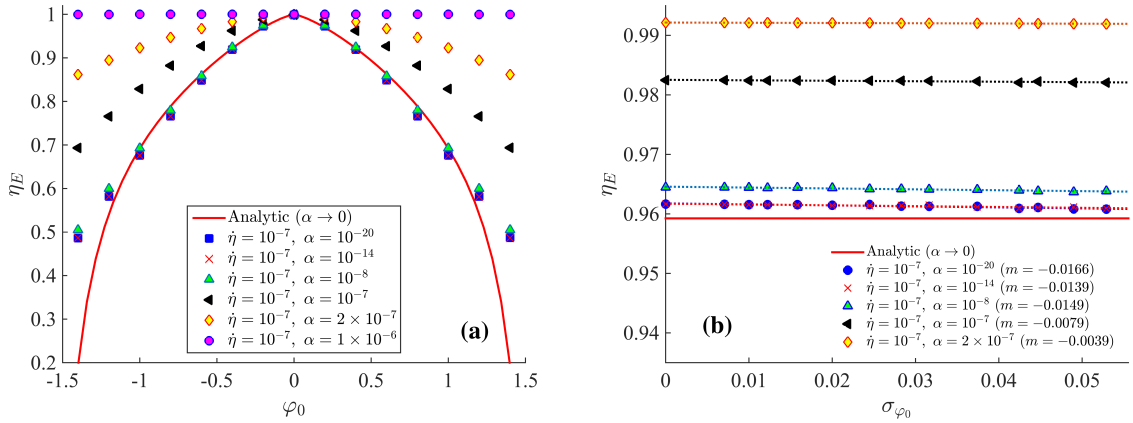

Figure 3.1. (a) Initial phase dependent escape current η_E under $T = 0$, $\dot{\eta} = 10^{-7}$, $\dot{\varphi}_0 = 0$. (b) Effect of the width of initial (Gaussian) distribution to the escape current, under $T = 0$, $\dot{\eta} = 10^{-7}$, $\dot{\varphi}_0 = 0$, and the distribution of the initial phase centered at $\varphi_0 = 0.25$. Different sets of data corresponds to various α's as shown in the legend. The dots represent the data from Langevin simulation, while the red curve is the estimated η_E obtained by solving for η_E from letting Δu_e in expression (3.2) be zero.

3.2.2 Dependence of escape current on initial phase for zero temperature but non-zero damping

If the damping α is increased from very low to a value equal to the sweep rate $\dot{\eta}$, again, in Figure 3.1 (a) the role of the criterion $\alpha/\dot{\eta}$ can be observed. For $\alpha < \dot{\eta}$, the system is in non-equilibrium state and the escape current depends on the initial condition φ_0. Once this ratio gets larger than one, the response becomes less sensitive to φ_0 and the curve ultimately gets flat for $\alpha = 10^{-6}$, which is ten time of the value of sweep rate. This is completely consistent with the observation of Figures 2.8 and 2.9. On the other hand, since the initial phase can be a distribution, in Figure 3.1 (b) we double check the effect of the width of the (Gaussian) initial phase distribution to η_E, using the same parameters in (a) but fixed $\varphi_0 = 0.25$. It shows that the effect of the width of initial distribution upon the escape current is almost negligible, i.e., in Langevin simulation, the peak position of the escape current distribution depends only on the center of initial distribution of phase under a certain damping coefficient. The previous simulations with single value of φ_0 can be treated as a special case with $\sigma_{\varphi_0} = 0$.

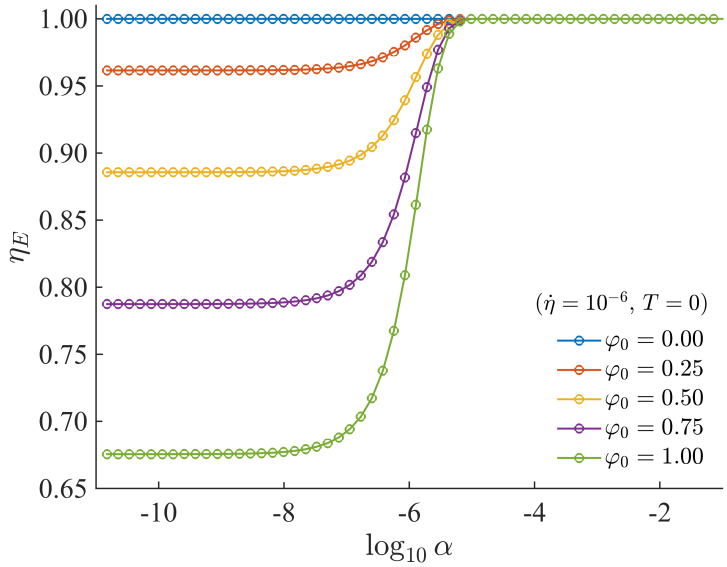

Figure 3.2. Dependence of escape current η_E upon damping α and initial phase φ_0. The plots are obtained for $\dot{\eta} = 10^{-6}$, $\dot{\varphi}_0 = 0$ and $T = 0$. The horizontal axis is the damping coefficient in logarithmic scale; each curve corresponds to a single φ_0.

Figure 3.2 shows the damping dependent escape current η_E under various initial phase φ_0 with $\dot{\eta} = 10^{-6}$. It can be seen that for $\alpha \ll \dot{\eta}$, the escape current η_E only depends on φ_0 - a

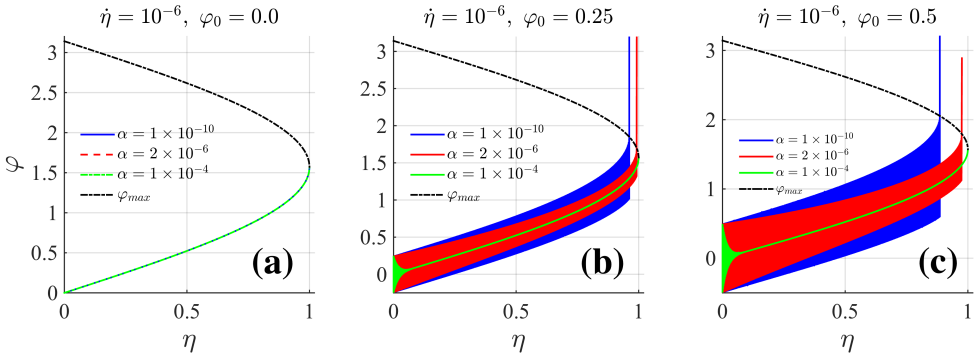

Figure 3.3. Phase oscillations with various damping and initial phases for $T = 0$ and $\dot{\eta} = 10^{-6}$; each subplot contains three values of damping: 10^{-10}, 2×10^{-6} and 10^{-2}, which are represented with blue, red and green colors; from (a) to (c), the initial phases φ_0 respectively equal to 0, 0.25 and 0.5. The black dash line denotes the position of the local maximum of the potential, and once it touches the trace of oscillation, the phase particle escapes. For $\alpha = 10^{-10}$, in (a), (b) and (c), the intersections (blue and black) are measured to be at $\eta_E = 0.9998$, 0.9624 and 0.8859.

larger φ_0 results in lower η_E as seen previously, and as $\alpha \to \dot{\eta}$, the system undergoes an abrupt transition around $\alpha/\dot{\eta} = 1$, larger than which, the effect of the initial condition on the over-damped phase particle will be rapidly diminished; due to zero temperature, the escape takes place only at $\eta_E \sim 1$. Figure 3.3, shows how the oscillation induced by the initial phase lowers the escape current η_E under the same sweep rate. In (a), the initial phase is $\varphi_0 = 0$. The absence of initial perturbation means the particle can only stay at the bottom of the well, moving with the minimum of the potential as the bias current ramps up, no matter how the damping changes within six orders of magnitude. Thus, the escape event won't take place until the well disappears at $\eta = 0.9998 \approx 1$, the cross of the curves of the local maximum and minimum. Between (b) and (c), the only difference is the nonzero initial phase φ_0 - respectively 0.25 and 0.5. For the case of $\alpha = 10^{-10} \ll \dot{\eta}$, these two values yield corresponding escape currents of 0.9624 and 0.8859. This is consistent with the reading from Figure 3.2. As the damping increases, the oscillation is damped out, resulting in the delay of escape or the increase of η_E. When $\alpha = 10^{-4} = 100\dot{\eta}$, the curves (green) in (b) and (c) look the same as the case of zero initial phase in (a), that is, the particle can only escape when the well gets flat at $\eta = 1$.

To summarize the response of the escape current η_E to the damping α and initial phase φ_0 under zero temperature, we make a 3D plot in Figure 3.4, which synthesizes Figures 3.1(a) and 3.2. It is clear that for $\alpha < \dot{\eta} = 10^{-6}$, the surface is a bell shape as seen in 3.1(a); the escape

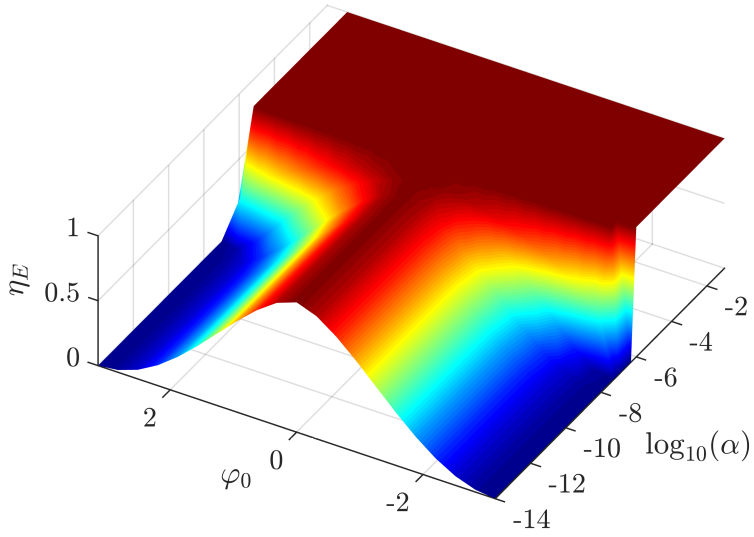

Figure 3.4. 3D plot showing the dependence of escape current η on damping α and initial phase φ_0. The plot is obtained for sweep rate $\dot{\eta} = 10^{-6}$ and $T = 0$.

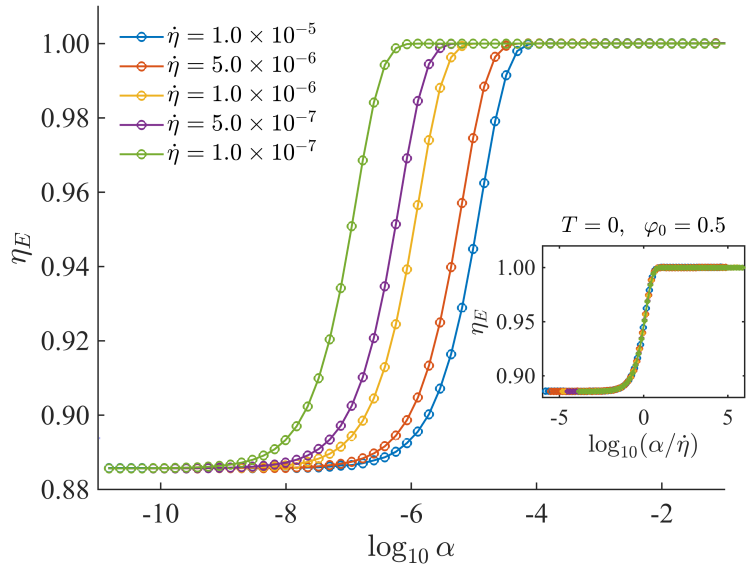

Figure 3.5. Dependence of the escape current η_E on the damping α and sweep rate $\dot{\eta}$ at $T = 0$, with initial phase $\varphi_0 = 0.5$. The plot in the inset is based on the same data but α is scaled by $\dot{\eta}$. The blue star stands for the estimated η_E obtained from $u_e = 0$.

current depends on the absolute value of the initial phase. For $\alpha/\dot{\eta} > 1$, it becomes a plateau, indicating the response is insensitive to the initial phase so the particle escape at $\eta = 1$. Figure 3.5, we show a more direct evidence for the dependence of the escape current upon the ratio

$\alpha/\dot{\eta}$. The plot is obtained for $\varphi_0 = 0.5$ and $T = 0$. A transition similar to Figure 3.2 is observed but here each curve denotes a sweep rate. As we can see that the position of the transition seems to move with the value of damping. However, if the horizontal axis is scaled by "normalizing" the damping by sweep rate, it is found that all of the curves collapse to a single one, as shown in the inset, that is, given a specific initial phase φ_0 at $T = 0$, the escape current η_E depends on the ratio of damping to sweep rate, $\alpha/\dot{\eta}$, instead of either of them solely.

3.2.3 Effect of the width of the initial phase distribution

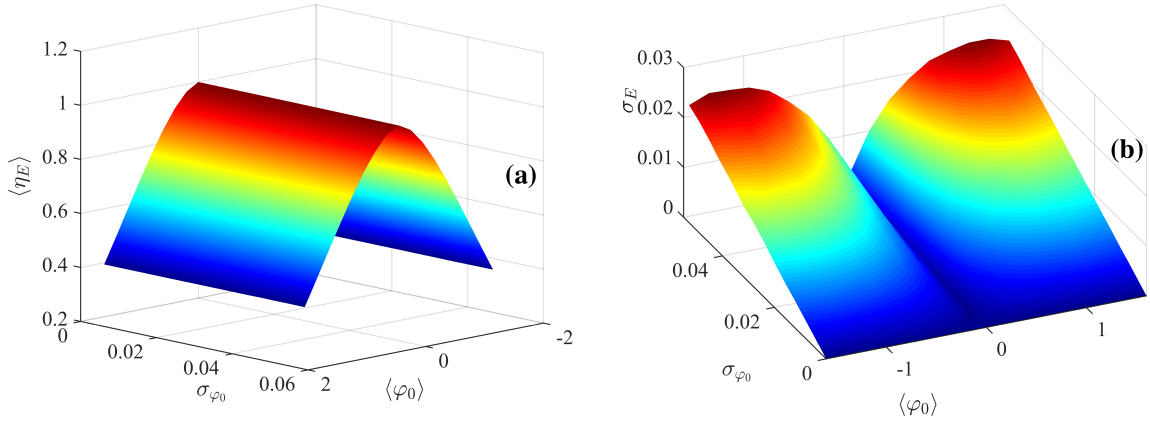

Figure 3.6. Effect of the center/mean ($\langle \varphi_0 \rangle$) and width/standard-deviation (σ_{φ_0}) of the distribution of initial phase to the escape statistics, $\langle \eta_E \rangle$ and σ_E. The other parameters used for the simulation are $\dot{\varphi}_0 = 0$, $\dot{\eta} = 10^{-6}$, $\alpha = 10^{-10}$ and $T = 0$.

Generally speaking, if the the initial phase is a distribution, when running a Langevin simulation, one must provide the information about its center (mean) and width (standard deviation), namely, $\langle \varphi_0 \rangle$ and σ_{φ_0}. In Figure 3.1(b) we have shown that the position of escape current distribution, $\langle \eta_E \rangle$, is independent of σ_{φ_0} and merely relies on $\langle \varphi_0 \rangle$. This property is summarized in Figure 3.6 (a), where we can see that each cross-section (the bell shape seen above) of any values of σ_{φ_0} is identical.

On the other hand, however, the response of the width of the escape current distribution σ_E on the initial condition looks more complicated. In Figure 3.6 (b) we can see σ_E is simultaneously determined by the $\langle \varphi_0 \rangle$ and σ_{φ_0}. There is a valley at $\langle \varphi_0 \rangle = 0$, where the width of the escape current distribution is a small number, regardless of the change of the σ_{φ_0}. The σ_E increases as $\langle \varphi_0 \rangle$ and σ_{φ_0} go up, and reaches a maximum around $\langle \varphi_0 \rangle = 1.5$. Figure 3.7 shows

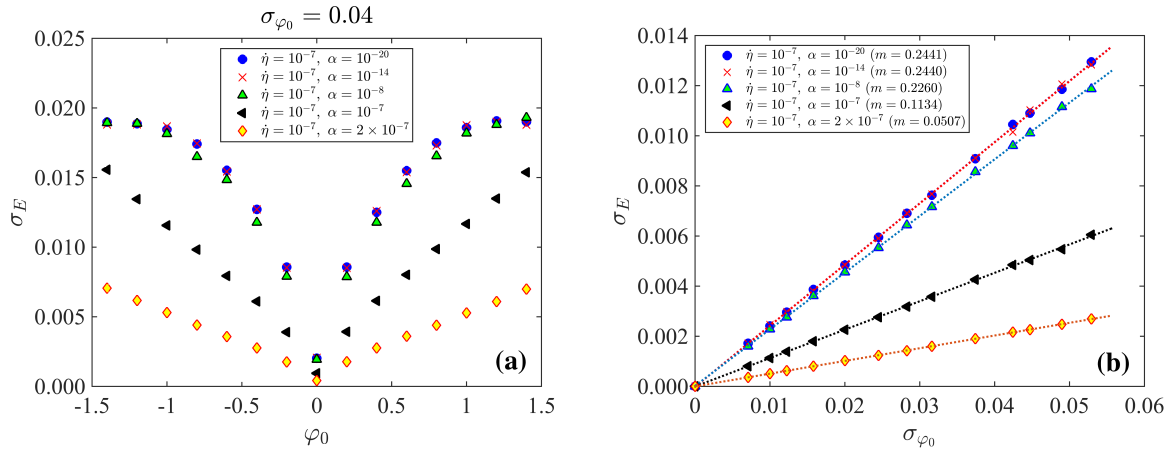

Figure 3.7. The response of the width of the escape current distribution σ_E to the position ($\langle\varphi_0\rangle$) and width (σ_{φ_0}) of the initial phase distribution, for $\dot{\eta} = 10^{-7}$, $T = 0$ and $\dot{\varphi}_0 = 0$. In (a), the width of initial phase distribution is fixed to $\sigma_{\varphi_0} = 0.04$, while in (b), the position of the initial phase distribution is $\langle\varphi_0\rangle = 0.25$. Each curve corresponds a single value of α.

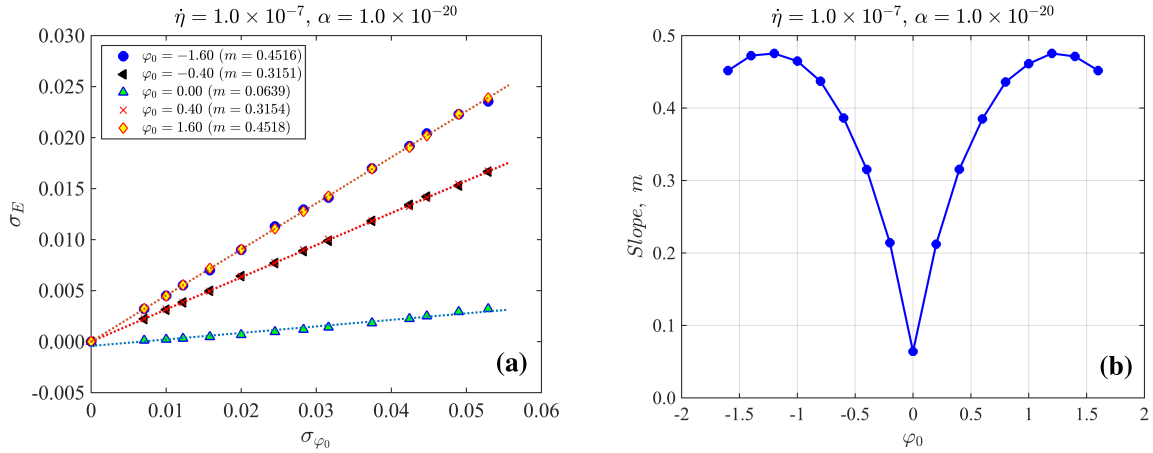

Figure 3.8. (a): Linear relation between the width of escape current, σ_E, and the width of initial phase distribution, σ_{φ_0}, under a fixed position of initial phase distribution, σ_{φ_0}, as shown in the legend. The parameters are $\dot{\eta} = 10^{-7}$, $\alpha = 10^{-20}$ and $T = 0$. (b) The slopes extracted from (a), but more data points are contained.

the projections of the similar surface in Figure 3.6 (b), but containing more cases for various damping α. From (a), it can be seen that for $\alpha/\dot{\eta} \ll 1$, the curves overlap, meaning σ_E only depends on φ_0. Besides, by fixing $\langle\varphi_0\rangle = 0.25$, we observe a linear relation between η_E and σ_{φ_0} in Figure 3.7 (b). For all values of damping, once the width of the initial phase distribution is zero, the width of the escape current distribution is also zero, due to the absence of noise. For $\alpha/\dot{\eta} \ll 1$, the curves tend to the same slope, which, however, as we know, is actually σ_{φ_0}-dependent. In Figure 3.8 (a), we just focus on the limit case with the extreme low damping,

by taking $\alpha = 10^{-20}$, and change the value of the position of the initial phase distribution φ_0. Again we can see the linear relation between σ_E and σ_{φ_0}, but the slope, m, is dependent on $\langle\varphi_0\rangle$. The slope m in Figure 3.8 (a) is measured and plotted in (b). In a word, unlike η_E that solely depends on $\langle\varphi_0\rangle$, the dependence of σ_E upon the both of the $\langle\varphi_0\rangle$ and σ_{φ_0} seems more complicated - it seems there is an expression: $\sigma_E = m(\langle\varphi_0\rangle)\cdot\sigma_{\varphi_0}$ - even for the limit case with $\alpha/\dot{\eta} \ll 1$.

3.3 Saturation phenomenon of escape current distribution

In the last section we discussed the dependence of the escape statistics on the initial condition at zero temperature. When $\alpha/\dot{\eta} < 1$, the position and width of the escape distribution largely rely on the initial position and width of the initial phase distribution. In this section, we will consider the case of non-zero temperature. In the presence of temperature or noise and a damping satisfying $\alpha > \dot{\eta}$, the thermal energy becomes dominant over the initial energy. The competition of these two kinds of energy together shapes the position and width curves of the escape current distribution.

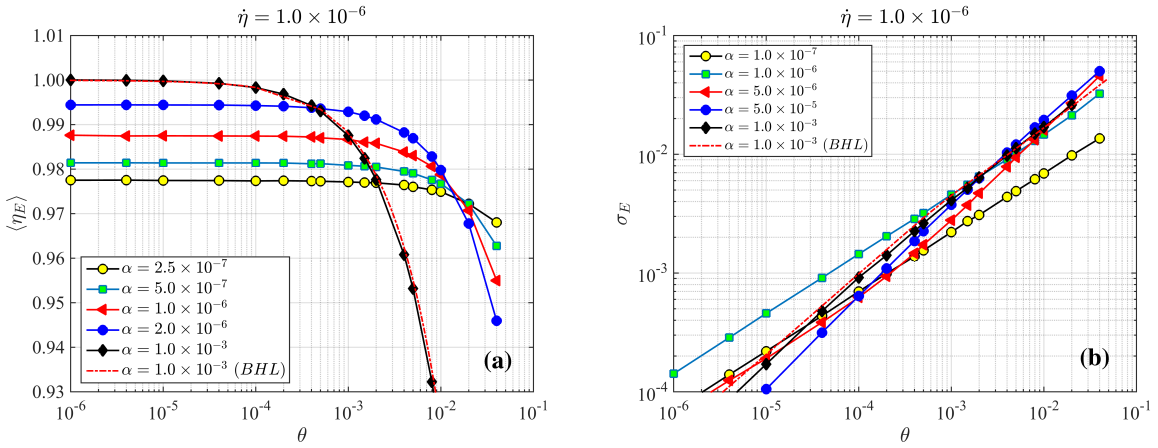

Figure 3.9. The dependence of the position (a) and width (b) of the escape distribution upon temperature ($\theta = k_B T/E_{j0}$) for non-distributed initial phase. The initial conditions are $\varphi_0 = 0.2$ and $\dot{\varphi}_0 = 0$; the sweep rate is $\dot{\eta} = 10^{-6}$. Each curve corresponds to a value of damping indicated in the legend. The red dash curves stand for the results produced by the BHL escape theory.

In Figure 3.9 (a) shows the temperature dependence of the position of the escape distribution. The initial phase is a single value, $\varphi_0 = 0.2$, with $\dot{\varphi}_0 = 0$; the sweep rate is $\dot{\eta} = 10^{-6}$. The

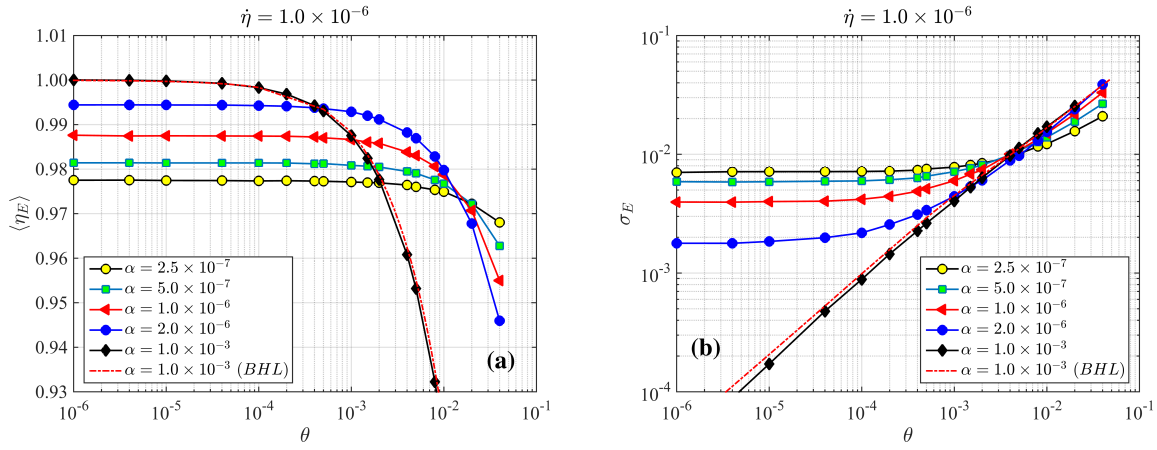

Figure 3.10. The dependence of the position (a) and width (b) of the escape distribution upon temperature ($\theta = k_B T / E_{j0}$) for distributed initial phase. The initial conditions are $\varphi_0 \sim \mathcal{N}(0.2,\ 0.04)$ and $\dot{\varphi}_0 = 0$; the sweep rate is $\dot{\eta} = 10^{-6}$. Each curve corresponds to a value of damping indicated in the legend. The red dash curves stand for the results produced by the BHL escape theory.

values of damping α are selected from 10^{-3} to 2.7×10^{-7}, crossing the ratio $\alpha/\dot{\eta} = 1$. We see that when $\alpha = 10^{-3} \gg \dot{\eta}$, the phase particle escapes at $\eta = 1$ at very low temperatures, as we have seen in Figure 3.3 - the oscillation induced by the initial perturbation has been damped out when the bias current reaches the one. This curve agrees well with the result of the BHL theory, which stands for the equilibrium state of the ensemble. When the damping is not too large, the position of the escape distribution presents "saturation" from a certain temperature ($\sim 10^{-4}$). As the value of damping decreases, the saturated peak of escape distribution moves toward the direction of decreasing bias current, because more initial energy can be preserved as the system becomes more under-damped and becomes a major factor that triggers the early escape. In (b), the temperature dependence of the width of escape distribution is shown. No saturation is observed, and as temperature decreases, the peak of the escape distribution keeps getting narrower; this is because the initial phase is a single number with zero standard deviation (width).

The setting of Figure 3.10 is similar to Figure 3.9, except that the initial phase becomes a normal distribution, $\varphi_0 \sim \mathcal{N}(0.2,\ 0.04)$, meaning that the initial phase distribution centered at $\varphi_0 = 0.2$ with a standard deviation being $\sigma_{\varphi_0} = 0.04$. Plot (a) looks the same as Figure 3.10, however, in (b), we observe the saturation of the peak width of the escape distribution, which

seems to only take place for $\alpha/\dot{\eta} < 1$, as expected. The peak of the escape distribution gets wider as the damping decreases, until getting to the limit $\alpha/\dot{\eta} \to 0$. For $\alpha/\dot{\eta} \gg 1$, we again see the straight curve that agrees with the BHL theory.

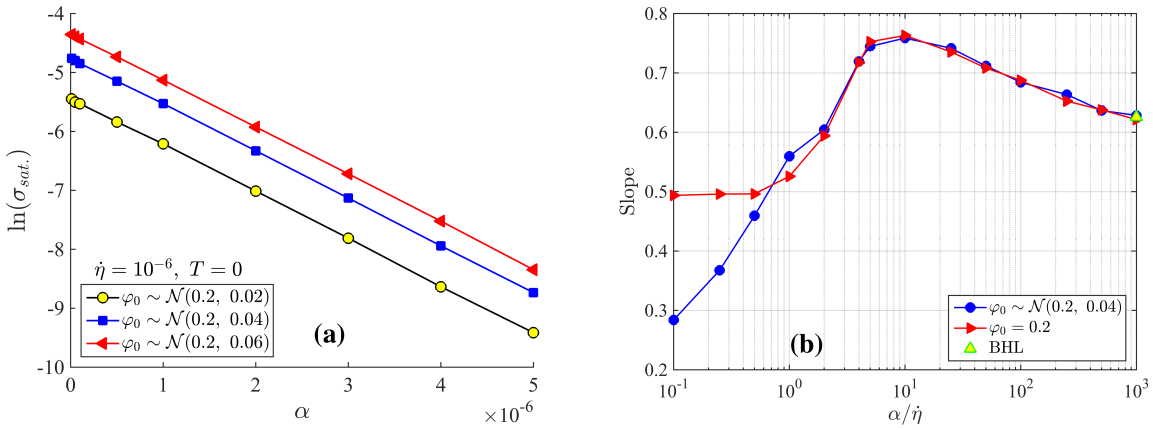

Figure 3.11. (a) Dependence of the saturated width of the escape current distribution upon damping for different initial conditions as shown in the legend, with $T = 0$ and sweep rate $\dot{\eta} = 10^{-6}$. (b) Dependence of the slope of the width curve in high temperature regime, for distributed and non-distributed initial phases as shown in the legend. The green triangle at the right end indicates the slope of the width curve predicted by BHL theory. The other settings are the same as Figures 3.9 (b) and 3.10 (b).

For the width curves in Figures 3.9 (b) and 3.10 (b), we also concern about the behaviors at low and high temperature. One measurable is the damping-dependence of the "saturated width" (σ_{sat}), which is defined as the peak width of the escape distribution for $T \to 0$. In Figure 3.11 (a), we can see that given an initial phase with certain width, the logarithm of the saturated width of the escape current distribution has a linear relation with the damping, and a larger width of the initial phase distribution can shift the straight line downward but the slope is unchanged, that is, we have $\sigma_{sat} = \sigma_0 e^{-s\alpha}$, where s is the slope and σ_0 is the value of σ_{sat} for $\alpha \to 0$. Another measurable is the damping-dependence of the slope of the width curve of the escape distribution in high temperature regime. In Figure 3.11 (b), we compare the slope-damping relation for the two kinds of initial conditions - Gaussian φ_0 (blue) and single value of φ_0 (red). It is found that these two curves are almost overlap for $\alpha/\dot{\eta} > 1$ especially as the influence of the initial condition is damped out, and as this ratio starts getting lower than one, they deviate - the curve with distributed initial phase saturates at $slope = 0.5$, while the curve with $\varphi_0 = 0.2$ keeps going down. For $\alpha = 10^{-3}$, we also mark the prediction of the BHL theory (green triangle) that

agrees well with the results of simulation and is close to the prediction $\sigma_E \sim (k_B T)^{2/3}$ in the literature [68].

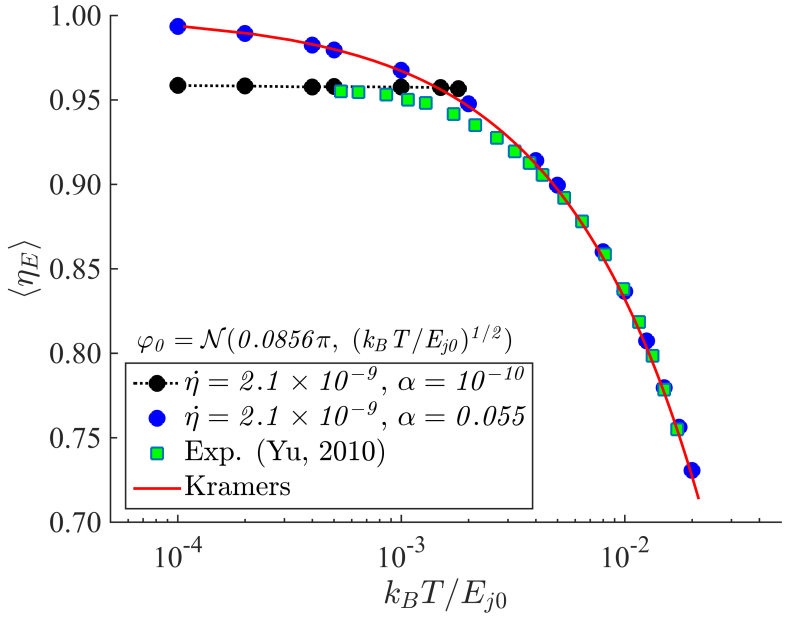

Figure 3.12. Temperature-dependent peak position of escape current distribution. The green dots stand for the experimental data from [66] with sweep rate $\dot{\eta} = 2.1 \times 10^{-9}$ and $\alpha = 0.055$; the blue and black dots stand for the result from the Langevin simulation with the same sweep rate as the experimental data but the damping coefficients α are respectively 0.055 and 10^{-10}; the initial phase distribution for the Langevin simulation centers at $\varphi_0 = 0.0856\pi$ with a standard deviation $\sigma = \sqrt{k_B T/E_{j0}}$, where $E_{j0} = 6.44 \times 10^{-22} J$. The red curve is generated by the Kramers escape theory.

3.4 Experimental background

Up to now we have shown that it is possible to accomplish "satutaration" at low temperatures using the effect of initial conditions under $\alpha/\dot{\eta} < 1$, while in high temperature regime, the results by Langevin simulation and BHL/Kramers theory show an excellent agreement. Hence, one may ask: to match the experimental data, how should we tune the two free parameters in the initial conditions - the center φ_0 and standard deviation σ_{φ_0} of the initial phase distribution? What are these parameters determined by? For example, Figure 3.12 illustrates the experimental data of the peak position of the switching current distribution (green dots) extracted from [66], in which, the relevant parameters are $C = 0.62\ pF$, $R = 300\Omega$, $I_c = 1.957\ \mu A$ and $dI/dt = 0.4\ mA/s$. We see the results of the Langevin ($\alpha = 0.055$) and Kramers simulations agree

well with the experimental data at high temperatures, but fail as the temperature decreased. To obtain a saturated escape/switching current that agrees with the experiment or the "MQT" result, based on the previous discussion in this chapter, we have set $\varphi_0 \approx 0.0269$ (black dots) and taken $\alpha = 10^{-10} < \dot{\eta}$ so that the effect of initial conditions can be persisted until the escape event occurs, but what does this value of initial phase mean? If it exists as a form of energy, then using the mean potential energy given by equation (1.36), one can obtain $\langle e_p \rangle = 0.018$. On the other hand, according to the experimental parameters in [66], we notice $\hbar\omega_{j0}/E_{j0} = 0.016$. Are these two values of energy actually identical or just coincidentally close? What does the $\hbar\omega_{j0}$ mean?

3.5 Conclusion

In this chapter we further discussed the effects of initial conditions for phase particles escaping out of the Josephson potential well by numerically solving the Langevin equation. For the limit of zero temperature and zero damping, there exists an analytic expression relating the (mean of) initial phase φ_0 and escape current η_E, and by comparing to the numerical simulation, it is found that this expression works well for $\varphi_0 < 0.5$, giving us a convenient way for estimate the saturation current for comparing to the experimental one.

For the case of zero temperature and non-zero damping, we confirmed that the response of the system only depends on the the ratio of the damping coefficient to the sweep rate, $\alpha/\dot{\eta}$, instead of one of them (Figure 3.5) solely. When $\alpha/\dot{\eta} < 1$, the responses of the system, i.e., the mean/position and the standard deviation/width of the escape current distribution ($\langle \eta_E \rangle$ and σ_E, respectively), are sensitive to the initial conditions, including the mean/position and the standard deviation/width of the initial phase distribution ($\langle \varphi_0 \rangle$ and σ_{φ_0}). As the damping coefficient increases, crossing $\alpha/\dot{\eta} = 1$, the influence of the initial condition will be rapidly diminished so the escaping can only take place at $\eta = 1$ in the absence of noise.

For the general cases with non-temperature and non-zero damping, the "saturation" of secape distribution is observed. If the initial phase is a distribution, the position and width of the escape distribution become independent of temperature when the temperature is low and the damping gets much smaller than the sweep rate. In experiments, this phenomenon is interpreted

by the theory of macroscopic quantum tunneling (MQT). At the end of this chapter, however, we showed that it is possible to produce such a saturation based on a classical RCSJ model in Langevin simulation, by imposing an initial phase distribution with specific mean and standard deviation. We will discuss this question in the next chapter.

Chapter 4

Comparison to Experiments

The behaviors of Cooper pairs of Josephson junction is described by the fundamental laws of quantum mechanics, resulting in the Josephson relations (1.8a) and (1.8b). Based on these two basic equations, the Resistively Capacitance Shunted Junction (RCSJ) model, which gives the dynamics of the phase difference across the junction, was proposed. The governing equation of the phase (1.29) is a stochastic second order ordinary differential equation (Langevin equation) that consists of macroscopic parameters, including temperature, capacitance, resistance, and current; the phase difference φ, the solution of the equation, is continuous and no discrete energy levels will be obtained. Since 1980s, a series of experiments were reported and it was found that the RCSJ model only worked in the high temperature regime, giving one of the mechanisms of switching of junction, called thermal activation (TA). As temperature was lowered, however, the peak position and width of the switching (escape) current distribution (SCD) and the escape rate of the phase particle were found to become constant, independent of temperature [20, 21, 45]. Thus, in the same decade, to interpret these phenomena, the theory of macroscopic quantum tunnelling (MQT) was proposed [25–28]. This school of approach concludes that quantization of the Josephson potential is necessary to describe the "tunneling" at low temperatures, as opposed to thermal escape at higher temperatures; the description of Josephson relations (1.8a) and (1.8b) are incomplete or just an approximation, so a more accurate quantum theory of the phase should exist [38]. A well-known MQT escape rate for

zero-temperature and absence of dissipation has been given by (1.50):

$$\Gamma_{MQT} = a_q \left(\frac{\omega_j}{2\pi}\right) \mathrm{e}^{-7.2\frac{\Delta U}{\hbar\omega_j}\left(1+\frac{0.87}{Q}\right)} \tag{4.1}$$

where $a_q = 864\pi\Delta U/\sqrt{\hbar\omega_j}$; ΔU is the height of the potential barrier; $Q \equiv \frac{1}{\omega_j RC}$ is the quality factor with plasma frequency ω_j. The MQT and TA together are considered forming a complete description for the behaviors for the phase difference in the theory side at present.

In this chapter, we will explore a classical activation (switching) mechanism for the escape of the phase particles (junctions) at low temperatures based on the ideas discussed in Chapters 2 and 3, where the "saturation" of peak position and width of escape current distribution has been observed in the Langevin simulations with an initial phase distribution imposed. The remaining question from chapter 3 is that, how the position and width of the initial phase distribution should be determined. If the initial phase relates to an energy, what is value of that energy? If this works for Langevin simulation, how is this idea reflected on the expression of Kramers or BHL escape rate?

4.1 Chemical potential induced by plasma oscillation

We have seen in Chapter 3 that adjusting the position and width of the initial phase distribution allows to produce "saturation" for the escape/switching distribution of the phase particle/Josephson junction. We now explore the source of the energy that provides this non-zero initial conditions. At the end of Chapter 3, we also noticed that the initial phase that makes the position of the escape current distribution in the Langevin simulation match the reported experimental data in [66] is close to the normalized energy $\hbar\omega_{j0}/E_{j0}$, which is a special but natural quantity worth investigation. In fact, the energy "$\hbar\omega$" has been our old friend and can be seen in many scenes - energy of photon, spacing of energy of level of quantum harmonic oscillator, mean energy of phonon, intensity of quantum fluctuation, or expression (1.22) etc.

We recall that the plasma frequency of the S state of Josephson junctions given by (1.13) as $\omega_j = \omega_{j0}(1-\eta^2)^{1/4}$, where $\omega_{j0} = (2eI_c/\hbar C)^{1/2}$. This can be derived from the analogous LC circuit or RCSJ model [8,69] as seen in Chapter 1. In the absence of the external current source ($\eta = 0$), the oscillation with the frequency of ω_{j0} is called "Josephson plasma mode" [9,10,70], first observed by A. J. Dahm et al. in 1968 [11]. At this point, the energy oscillates between the

equivalent inductor and capacitor of the junction, and the junction is unstable so the supercurrent may fluctuate between $\pm I_c$. According to the Anderson equation [7, 9, 41]

$$\hbar \frac{d\varphi}{dt} = \partial_N E \equiv \mu, \tag{4.2}$$

this zero-bias plasma frequency implies there exists an energy in the form of chemical potential μ across the junction under zero external voltage, instead of zero as indicated by the ΔU in (1.33). Integrating equation (4.2), we have $\varphi = \frac{\mu t}{\hbar} + const.$, which yields $\omega = \mu/\hbar$. For the case of zero-bias, we have $\mu_0 = \hbar\omega_{j0}$. Therefore, when performing Kramers/BHL and Langevin simulations, in principle, it is necessary to take into account this chemical potential, which actually plays a role of lowering the depth of the potential well ΔU and may influence the switching of the junction. Following is some of our suggestion on the improvements to the typical Kramers/BHL and Langevin simulations:

(a) For Kramers or BHL simulation, the effective height of the well should take the form $\Delta U_{\text{eff}} = \Delta U - \hbar\omega_{j0}$. However, considering the observation in Chapters 2 and 3 that in high temperature regime, the information from the starting point of the motion of phase particle will be covered by the thermal noise, we introduce a correction factor: $\mathrm{e}^{-k_B T/\hbar\omega_{j0}}$, for simulating the competition between the thermal fluctuation characterized by $\alpha k_B T$ and the energy $\mu_0 = \hbar\omega_{j0}$, whose influence will be diminished as the temperature goes up. Hence, as a minor modification to the Kramers/BHL escape rate, the depth of the potential well reads[1]

$$\Delta U_{\text{eff}} = \Delta U - \hbar\omega_{j0} \cdot \mathrm{e}^{-\frac{k_B T}{\hbar\omega_{j0}}}. \tag{4.3}$$

(b) For Langevin simulation, the chemical potential acts as the average potential energy. Assuming the phase particle is released at position φ_0 with velocity $\dot{\varphi}_0 = 0$ initially, the total energy will be $E_{tot} = 1 - \cos\varphi_0$, which yields an average potential energy given by equation (1.36) in Chapter 2 with small oscillation approximation (supported by experimental data). Thus, relating (1.36) and the chemical potential μ_0 as

$$\frac{1}{2}(1 - \cos\varphi_0) E_{j0} = \hbar\omega_{j0} \tag{4.4}$$

[1] In [42] we took the form $\Delta U_{\text{eff}} \approx \Delta U - \hbar\omega_{j0}(1 - k_B T/\hbar\omega_{j0})$ for $T \ll T_c$, where T_c is the critical temperature of the junction.

results in the initial phase φ_0 that should be used for Langevin simulation ($\dot{\varphi} = 0$). Since the trajectory of the phase particle with harmonic oscillation around the minimum of the well is a circle in the phase plane: $H \approx \frac{1}{2}\dot{\varphi}^2 + \frac{1}{2}\varphi^2$, the same value for φ_0 calculated from (4.4) can be imposed to $\dot{\varphi}_0$ alternatively (with $\varphi_0 = 0$). On the other hand, a temperature-dependent thermal initial condition satisfied the Maxwell-Boltzmann distribution can be applied to the initial phase derivative $\dot{\varphi}_0$.

4.2 Effect of μ_0 on Kramers simulation

In this section we will investigate the effects of the chemical potential $\mu_0 = \hbar\omega_{j0}$ on the Kramers simulation with the considerations above by replacing the ΔU in the exponential with ΔU_{eff} in (4.3). Since the difference between the Kramers and BHL model is the prefector, this improvement works for the BHL as well. Let's start with a simplest case.

4.2.1 Switching current solved from $\Delta U_{\text{eff}}(\eta) = 0$

Since the chemical potential lowers the depth of the original well, when the effective well becomes flat, i.e., when the following equation holds:

$$\Delta U_{\text{eff}} = 2E_{j0}(\sqrt{1-\eta^2} - \eta\cos^{-1}\eta) - \hbar\omega_{j0} = 0, \tag{4.5}$$

it is expected that the phase particle escapes. Thus, a corresponding switching current η_{sw} can be solved from equation (4.5). Note that this is just an oversimplified model with the initial and final states considered. The complex dynamic processes are neglected and the key factors for the switching mechanism, such as temperature, damping, sweep rate are not involved, that is, the switching current η_{sw} is actually a limit under the case of zero temperature and low damping, which is also the quantum limit in the MQT rate calculated in the Wentzel-Kramers-Brillouin (WKB) approximation [27]. We solved the values of η_{sw} from equation (4.5) based on the junction parameters from ten selected experiments [45, 66, 67, 71–77], and compared to the reported values. The results are plotted in Figure 4.1, in which, the calculated switching currents are recorded on the vertical axis and on the horizontal axis are the corresponding experimental value of the peak position of the switching current distribution. It can be seen that the the points well align along a straight line (red) with linear correlation coefficient $R = 0.9727$. It

slightly deviate from the ideal line (dash) standing for the experimental and calculated switching currents being equal, and the cause is that the calculated η_{sw} is the limit for zero temperature and damping, while the corresponding experiential values are for low but finite temperature and damping. By t-test, the probability that the predictions based on (4.5) are not related to the experimental data is less than 10^{-5}. The high linear correlation shows that the chemical potential $\mu_0 = \hbar\omega_{j0}$ does have some kind of effect in determining the position of the SCD peaks.

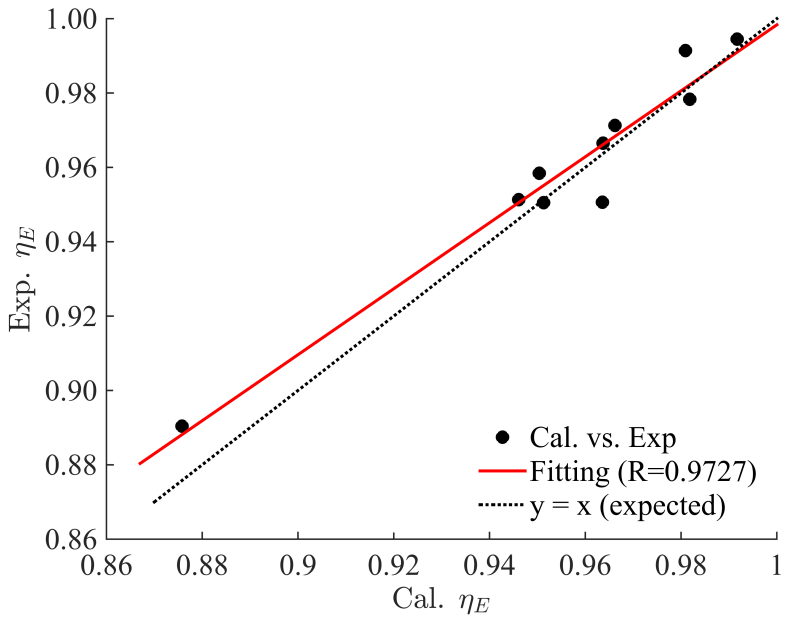

Figure 4.1. The estimated switching current η_{sw} v.s. the corresponding reported experimental values from [45, 66, 67, 71–77]. The horizontal and vertical coordinates of a dot respectively correspond to the calculated and experimental switching currents; the red line is the linear fitting curve of the data points, and the dash line denotes the ideal situation with experimental and calculated switching currents being equal.

4.2.2 Effect of the chemical potential μ_0 on Kramers model for $T = 0$

If the chemical potential is imposed to the Kramers escape rate by replacing ΔU with ΔU_{eff} in (4.3) but setting $T = 0$, it can be expected that the peak position curve of SCD in this limit will be consistent with the calculated η_{sw} solved from (4.5). We selected the experimental data from [66, 72] and plot the comparison in Figure 4.2. As we see, the dash straight line obtained by solving for η_{sw} from (4.5), the red peak position curves generated by the modified

	Washburn (1985)	Wallraff (2003)	Inomata (2005)	Männik (2005)	Li (2007)
C $[pF]$	0.15	1.6	0.07626	0.26	0.088
I_c $[\mu A]$	57.4	325	48.54	2.90	0.748
eff.R $[\Omega]$	23	240	942.9	75	250
dI/dt $[mA/s]$	0.4	245	42.4	0.088	0.16
$(\dot{\eta})$	6.5×10^{-12}	9.6×10^{-10}	6.3×10^{-10}	1.7×10^{-10}	1.3×10^{-9}
f_{j0} $[Hz]$	171.6	125.0	221.3	29.3	25.58
α	0.269	0.00332	0.01	0.279	0.283
E_{j0} $[J]$	4.6×10^{-22}	1.1×10^{-19}	1.6×10^{-20}	9.5×10^{-22}	2.5×10^{-22}
Exp. I_{sat} $[\mu A]$	56.35	322.3	46.90	2.7586	0.6551
Cal. I_{sat} $[\mu A]$	56.16	323.2	47.76	2.7568	0.6660
Exp. T_{cr} $[K]$	600	~ 300	~ 750	~ 90	110
Cal. T_{cr} $[K]$	510.6	604.9	872	100.5	94.2

	Cui (2008)	Yu (2010)	Yu (2013)	Oelsner (2013)	Massarotti (2015)
C $[pF]$	0.18	0.62	0.26	0.33	4.5
I_c $[\mu A]$	12.87	1.957	2.9	2.2	30.41
eff.R $[\Omega]$	200	300	2090	440	N/A
dI/dt $[mA/s]$	2.116	0.4	8.93	0.0001	2.0
$(\dot{\eta})$	3.5×10^{-10}	2.1×10^{-9}	1.7×10^{-8}	3.2×10^{-13}	4.8×10^{-13}
f_{j0} $[Hz]$	74.18	15.59	29.30	22.65	22.81
α	0.0596	0.0549	0.0010	0.0484	0.4653
E_{j0} $[J]$	4.2×10^{-21}	6.4×10^{-22}	9.5×10^{-22}	7.2×10^{-22}	1.0×10^{-20}
Exp. I_{sat} $[\mu A]$	12.402	1.86	2.7435	2.12	29.83
Cal. I_{sat} $[\mu A]$	12.438	1.8756	2.7586	2.0914	30.15
Exp. T_{cr} $[K]$	~ 250	65 ± 5	125	~ 56	~ 100
Cal. T_{cr} $[K]$	275.9	65.02	143.7	54.5	62.5

Table 4.1. The main parameters extracted from the selected experiments [45, 66, 67, 71–77], and compared to the reported values. and the comparisons between the corresponding experimental and calculated saturation switching current I_{sat} and crossover temperature T_{cr}.

Kramers model (4.3), and the experimental data (green dots) approach to the same limits of peak position of SCD as $T \to 0$, the low temperature region that the original Kramers model fails (blue solid curves). For higher temperatures, however, discrepancy is significant; this is not surprising, since μ_0 only referred to $T = 0$. Nevertheless, under the zero-temperature limit, it is evident that there is a good agreement among experimental data, modified Kramer model, and the over-simplified model (4.5). The dash straight line generated by (4.5) can be seen as being equivalent to the "MQT line" (see Fig.2 in [66] and Fig.1 in [67]). Naturally, one may ask whether the temperature corresponding to the intersection between the "MQT line" and the Kramers curve is comparable to the "crossover temperature" T_{cr} estimated by equating the escape rate for thermal activation and the escape rate for MQT [29, 78]. Here, we also measure such temperatures corresponding to the intersection on the plots similar to thoese in Figure 4.1 and put them in Table 4.1. It can be seen that the "crossover temperatures" defined in this way are close to the experimental values of T_{cr}.

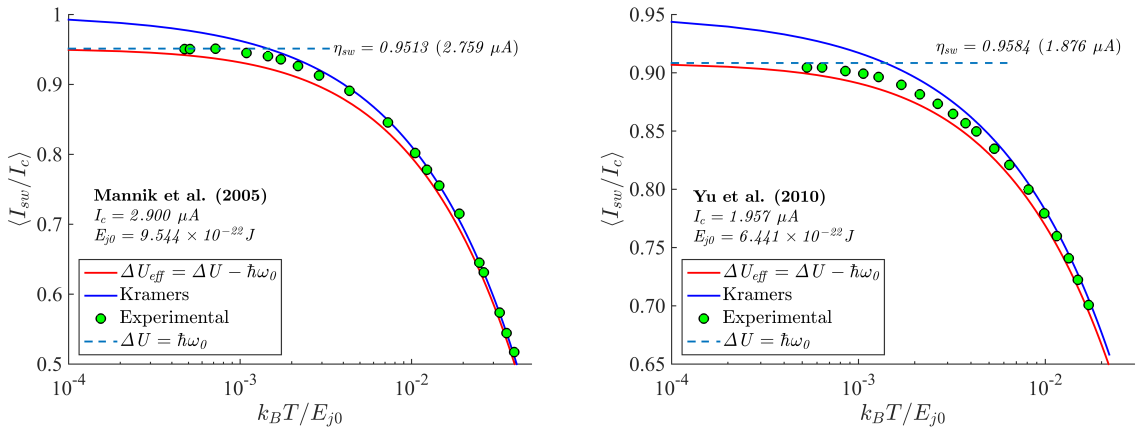

Figure 4.2. The peak positions of SCD from the modified Kramers model by subtracting to the Josephson potential the chemical potential (red curve), compared to the ones extraced from the two experiments in [66, 72]. The horizontal axis is the normalized temperature and the $\langle \eta_{sw} \rangle$ on the vertical axis stands for the mean (peak position) of SCD.

4.2.3 Effect of the chemical potential μ_0 on Kramers model for finite temperature

Now let's consider a more general situation that the chemical potential $\mu_0 = \hbar\omega_{j0}$ plays the role in the way as (4.3) shows:

$$U_{\text{eff}} = \Delta U - \hbar\omega_{j0} \cdot \mathrm{e}^{-\frac{k_B T}{\hbar\omega_{j0}}}.$$

As the temperature increases, the influence of μ_0 will be diminished as seen in Chapters 2 and 3 due to the effects of dissipation and thermal fluctuation, and this is now characterized by the exponential factor, $\mathrm{e}^{-\hbar\omega_{j0}/k_B T}$. The results are plotted in Figures 4.3 and 4.4, in which, our model (red solid) is compared to the original Kramers curve (dashed) and the experimental data (dots) reported in [66, 67, 72, 74]. It can be seen that our theoretical curves with the correction μ_0 agree well with the original Kramers curve in high temperature region, which corresponds to the thermal activation (TA) regime. Meanwhile, the theoretical curves also get closer to the experimental data in low temperature region, where the original Kramers curve deviates from the experimental data and approaches $\eta = 1$. This low-temperature region corresponds to the regime of macroscopic quantum theory (MQT) in the literature, here, however, MQT is not involved. Similar to Figure 4.2, the dotted lines parallel to the horizontal axis in Figures 4.3 and 4.4 denote the switching current where the effective potential well gets flat, treated as a limit under zero-temperature and zero-damping; the intersection between this straight line and the original Kramers curve defines the "crossover temperature", T_{cr} (see the figure legend), and it is shown that they agree with the experimental values in Table 4.1.

So far, we have presented the results produced by the improved Kramers model with ΔU replaced by the ΔU_{eff} in (4.3) agrees well with the experimental data in the whole range of temperature, without introducing any free fitting parameters or any MQT concepts. Just like all experiments so far performed - the critical current I_c is obtained by fitting the experimental switching distribution data taken at the high temperature regime with the Kramers model, the value of I_c here is determined by fitting the experimental data taken at all temperatures with our improved model, but the difference from the reported values is minimal. The specific parameters, including the junction capacitance C, sweep rate dI/dt, are the same as shown in Table 4.1, while the critical currents I_c from the experiments [66, 67, 72, 74] and used for Figures 4.3

and 4.4 are slightly adjusted as $I_{c,m} = \{2.902,\ 0.761,\ 1.967,\ 2.244\}\ \mu A$.

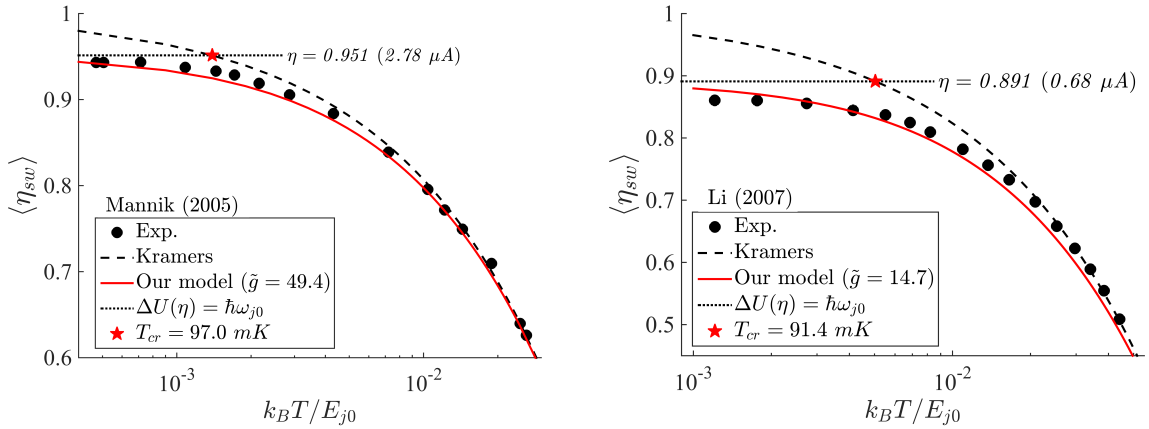

Figure 4.3. The temperature dependence of the position (mean) of SCD from experimental results (dots) reported in [72, 74], original Kramers model (dashed curve) and our models (solid curve). The horizontal dotted line represents the switching current solved from equation (4.5) at $T = 0$; the intersection with Kramers curve defines T_{cr} , identified by a star.

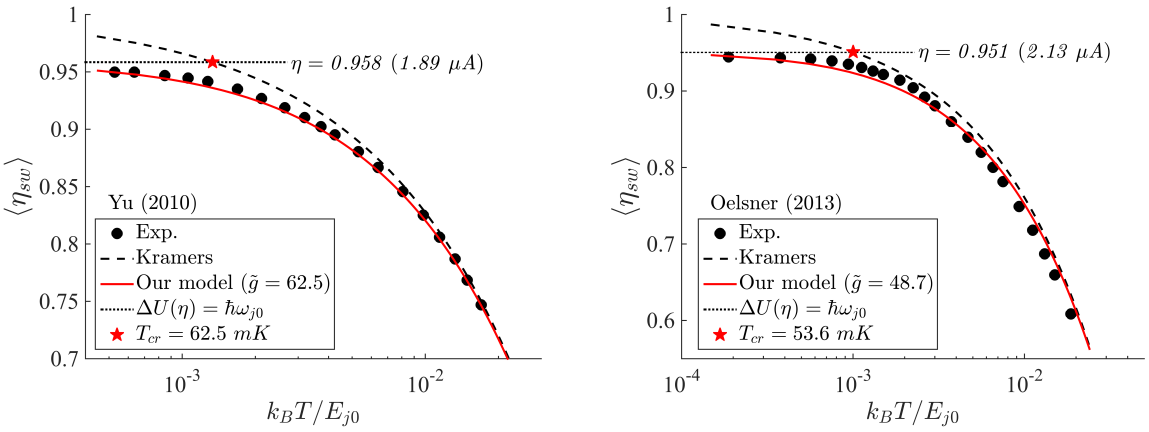

Figure 4.4. The temperature dependence of the position (mean) of SCD from experiments, original Kramers model (dashed curve) and our models (solid curve), similar to Figure 4.3 except that the parameters are based on experimental data from [66, 67].

We should note here that the improved model presented above is a minimum modification to the Kramers (and BHL) model, in order to show that there objectively exists a chemical potential $\mu_0 = \hbar\omega_{j0}$ that can give a correct prediction for the peak position η_{sw} of SCD. However, since we merely corrected the depth of the potential well in the escape rate, in which, the denominator of the exponential, $k_B T$, indicates the peak width of SCD would still be temperature dependent. In Figure 4.5 we can see that the data points from each experiments are aligned along straight

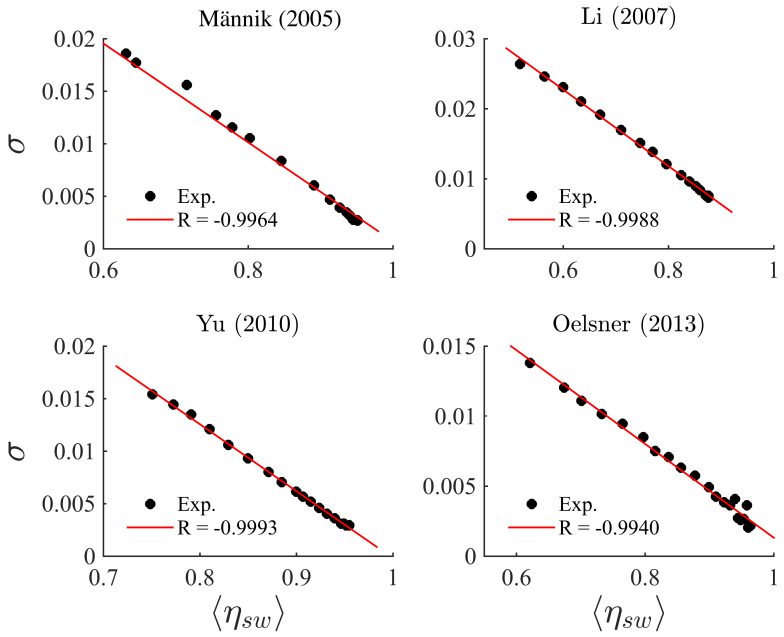

Figure 4.5. Experimental switching current distribution width vs average switching current, obtained from the experiments [66, 67, 72, 74]. The R in each legend indicates the linear correlation coefficient of the data points.

lines (red) with linear correlation coefficients R very close to one, meaning that the peak position and width of SCD have the same dependence on temperature. A complete improved model is expected to be able to produce saturated SCD peak position and peak width simultaneously, as the experiments show. Ref. [79] may give us a hint on this.

4.3 The effects of μ_0 on Langevin simulation

If the chemical potential μ_0 is a correct consideration and does improve the Kramers/BHL model, then the same success should be able to be replicated in the Langevin simulation at low temperatures. We have assumed the chemical energy μ_0 induced by the zero-bias plasma oscillation enters the RCSJ model as an average potential energy, and according to equation (4.4), we have $0.5(1-\cos\varphi_0) = \hbar\omega_{j0}/E_{j0}$, which gives an initial phase φ_0. For instance, the value of the normalized chemical potential for the experiment in [66] is $\hbar\omega_{j0}/E_{j0} = 0.016$, resulting in $\varphi_0 = 0.2539$. On the other hand, in the previous chapters we have shown that the information of the initial condition can be preserved and affects the switching current distribution only when the damping is lower than the sweep rate, $\alpha/\dot{\eta} < 1$, but it also requires the damping to maintain

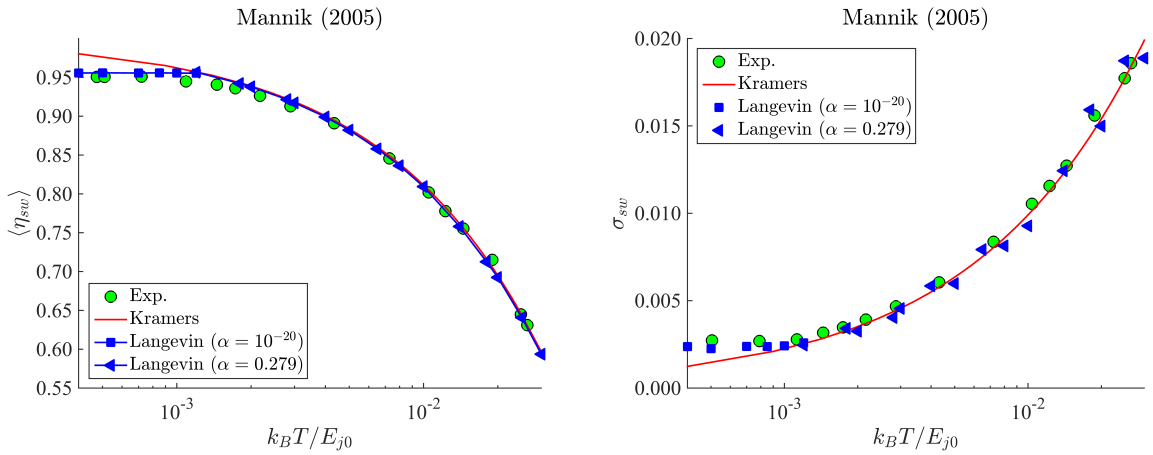

Figure 4.6. Temperature dependence of the mean $\langle \eta_{sw} \rangle$ and standard deviation σ_{sw} of switching current distribution. The red solid curve is generated by Kramers model. The green dots are the experimental data from experiment [72]. The blue square and triangular dots are from the Langevin simulations with $\alpha = 10^{-20}$ and 0.279. The initial conditions are $\langle \varphi_0 \rangle = 0.2833$ and $\sigma_{\varphi_0} = \sqrt{\hbar \omega_{j0}/150}$; the normalized sweep rate is 1.7×10^{-10}.

the thermal equilibrium at high temperature. This means that the damping coefficient α should be a function of temperature. Since the damping in RCSJ model is defined as $\alpha = 1/\omega_{j0} RC$, where R can be a function of temperature, such as $R = R_0 e^{\Delta/k_B T}$ given in (1.40), where Δ is energy gap of the junction. Note that this expression for R is not the unique one, but just consistent with our consideration for the Kramers/BHL model, that is, $\alpha \to 0$ for $T \to 0$ and $\alpha \to \alpha_0$ for high temperature regimes. In the Langevin simulation here, we actually use a discontinuous damping term that based on these two limit due to lack of specific information for the junction resistance in superconducting state.

For the initial phase distribution in the Langevin simulation, we will select a Gaussian one, i.e., $\mathcal{N}(\varphi_0, \sigma_{\varphi_0})$. The reasons are that the experimental data shows that the SCD is also Gaussian, and to guarantee a Gaussian outcome, we have to use a Gaussian initial distribution as an input as well, since although in high temperature regime, the dissipation-fluctuation theorem and central limit theorem will yield a Gaussian outcome [80] no matter what the initial condition is as seen in the previous chapters, at low temperatures and low damping with $\alpha/\dot{\eta} \ll 1$, the initial distribution will be preserved. Thus, in Figures 4.6, 4.7 and 4.8, applying a initial Gaussian distribution centered at φ_0 given by μ_0 with appropriate width σ_{φ_0} (which is an adjustable parameter) as shown in the caption of each figure, we generate such peak position and

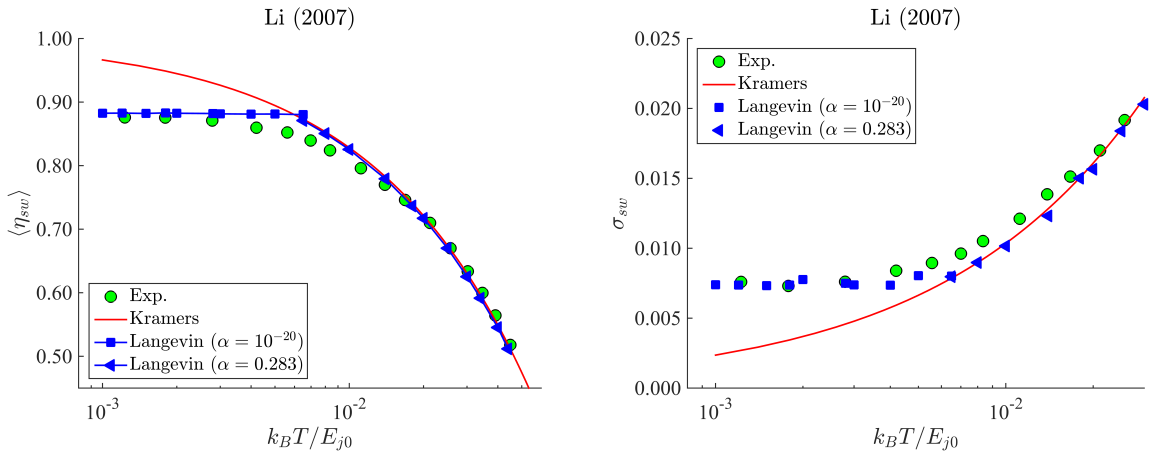

Figure 4.7. Temperature dependence of the mean $\langle \eta_{sw} \rangle$ and standard deviation σ_{sw} of switching current distribution. The red solid curve is generated by Kramers model. The green dots are the experimental data from experiment [74]. The blue square and triangular dots are from the Langevin simulations with $\alpha = 10^{-20}$ and 0.283. The initial conditions are $\langle \varphi_0 \rangle = 0.512$ and $\sigma_{\varphi_0} = \sqrt{\hbar\omega_{j0}/125}$; the normalized sweep rate is $\dot{\eta} = 1.3 \times 10^{-9}$..

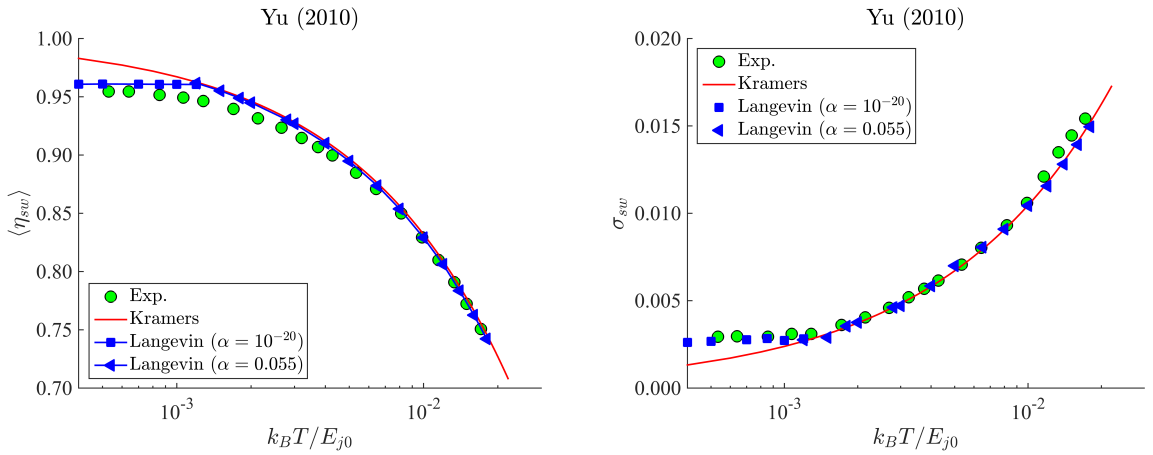

Figure 4.8. Temperature dependence of the mean $\langle \eta_{sw} \rangle$ and standard deviation σ_{sw} of switching current distribution. The red solid curve is generated by Kramers model. The green dots are the experimental data from experiment [66]. The blue square and triangular dots are from the Langevin simulations with $\alpha = 10^{-20}$ and 0.055. The initial conditions are $\langle \varphi_0 \rangle = 0.252$ and $\sigma_{\varphi_0} = \sqrt{\hbar\omega_{j0}/115}$;the normalized sweep rate is $\dot{\eta} = 2.1 \times 10^{-9}$..

peak width curves consisting of two sections - low damping (squared dots, use $\alpha = 10^{-20} \sim 0$ to guarantee $\alpha \ll \dot{\eta}$) for low temperatures, and normal damping for high temperatures (triangular dots) in thermal activation regime. It can be seen that for both of the peak position and peak width curves in each case, the Langevin simulation gives perfect agreement with the experimental data at high temperatures. Although we just use an extreme case for the damping in order to preserve the initial energy (chemical potantial μ_0) for low temperature so that the

SCD "saturation" can be obtained, at the zero-temperatures limit here, it does agree well with the experimental data (green dots) as the Kramers model did. Note again there is no problem that the SCD peak position obtained in the Langevin simulation depends on the position of the initial phase distribution, but the width of of the initial phase distribution σ_{φ_0}, which is expected to determine the SCD width, is a free parameters (see the caption under each plot). Finding a more reasonable description for the damping term $\alpha(T)$ and erasing the free parameter in the width of the initial phase distribution are two of our future missions.

4.4 Conclusion

The RCSJ model is purely classical originally, and then a quantum postulate (see section 1.2.3) was imposed so it gets quantized and is able to describe the behavior of the junctions in low temperatures. This postulate is necessary or not might be questionable, but one who wants to negate it must propose a classical model that works for low temperatures like MQT does. In this chapter, we try to improve the classical Kramers and Langevin simulations by introducing the chemical potential potential $\mu_0 = \hbar\omega_{j0}$ induced by plasma oscillation. In the improved Kramers model, the height of the Josephson potential well ΔU is replaced with the temperature-dependent effective height: $\Delta U_{\text{eff}} = \Delta U - \mu_0 \mathrm{e}^{-k_B T/\mu_0}$, in which, the exponential factor is used to characterize the attenuation of the effect of μ_0 due to thermal fluctuation as temperature increases. In the Langevin simulation, the chemical potential acts as an intrinsic energy that the phase particle carries, leading to a biased initial phase φ_0. Both of these methods can produce peak position curves of SCD that agree well with the experimental data at low temperatures, but there are limitations for each: for the Kramers simulation, the chemical potential in the expression of ΔU_{eff} is not able to produce correct peak width curves; for the Langevin simulation, there is no such an continuous form for the damping term and the factor that determines the width of the initial phase distribution is still unclear.

Nevertheless, we have shown a possibility that the classical RCSJ model can be able to give a complete description for the switching problem of the Josephson junction in full range of temperature, and the finding presented in this chapter - the chemical potential $\mu_0 = \hbar\omega_{j0}$ induced by the plasma oscillation in the junction will be an necessary condition to achieve this.

Chapter 5

Long Josephson junction

Long Josephson junction (LJJ) is a Josephson junction having one or more dimensions longer than the Josephson penetration depth λ_J. Compared to the zero-dimensional single Josephson junction discussed in the previous chapters, LJJ has more complex but interesting mathematical and physical properties, such as fluxon, a quantum of magnetic flux also known as Josephson vortex induced by supercurrent loop and external magnetic field applied perpendicular to the length of the long junction (see Figure 5.1). The governing equation describing the phase difference along the LJJ is the sine-Gordon equation (sGE), a partial differential equation having a travelling wave solution (a.k.a. solitary wave, soliton), $\varphi(\mathbf{r},t)$, representing the fluxons moving along the LJJ. For this reason, the terms - fluxon, soliton and Josephon vortex - refer to the same object in this chapter. The earliest observations of the internal fluxon motion were performed by Scott et al. in 1969 [81] - magnetic and temperature independent slopes seen on the linear branch of the I-V characteristics below 2.2 K, and by Fulton et al. in 1973 [82] - finite V-I steps present in the absence of magnetic field. The perturbation theory of fluxon dynamics and its application has been widely studied during 1980s - 1990s, e.g. Refs. [83–88]. The typical applications of sGE include large arrays of Josephson junctions as microwave generators [89] and detectors, propagation of a crystal dislocation and ultra-short optical pulses [90], magnetic flux propagation along a Josephson-junction transmission line [91], logic circuits (RSFQ [92], RFL [93, 94]), etc. In this chapter, we will focus on a one-dimensional long Josephson junction and present some analytic and numerical results.

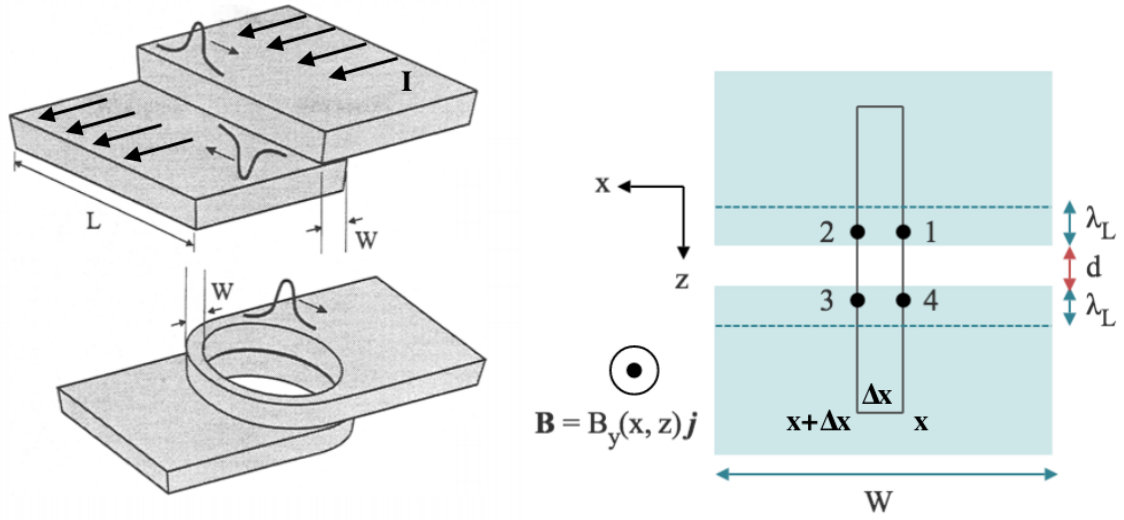

Figure 5.1. Left: Two of the LJJ geometries, overlap and annular junction (from [95]). Right: Cross-section of a long Josephson junction; two superconductor are separated by an insulator of width W; a magnetic field $\mathbf{B}$ is applied as shown; the solid line inside the junction represents an integration contour; λ_L is the London penetration depth and d is the thickness of the insulator.

5.1 Sine-Gordon equation

The details on the derivation of the sine-Gordon equation can be found in Refs. [8, 69, 90, 91]. Here, let's start with the macroscopic wave function that describes superconductivity $\psi = \sqrt{\rho(\mathbf{r},t)}e^{i\varphi}$, where φ is the phase of a superconductor and ρ is the number density of Cooper pairs, and the current density $\mathbf{J}$ given by the Ginzburg–Landau equation:

$$\mathbf{J} = -\frac{i\hbar e^*}{2m^*}(\psi^*\nabla - \psi\nabla^*\psi) - \frac{e^{*2}}{m^*}|\psi|^2\mathbf{A}, \tag{5.1}$$

where $e^* = 2e$ and $m^* = 2m$ are the charge and mass of the Cooper pair with e and m being of a single electron; $\mathbf{A}$ is magnetic potential vector. Substituting the wave function in (5.1), we have

$$\begin{aligned} \mathbf{J} &= \frac{e\rho}{m}(\hbar\nabla\varphi - 2e\mathbf{A}) \\ \Rightarrow \quad \nabla\varphi &= \frac{2e}{\hbar}\left(\frac{m\mathbf{J}}{2e^2\rho} + \mathbf{A}\right). \end{aligned} \tag{5.2}$$

As shown in Figure 5.1 (Right), when the thickness of the insulator d is much smaller than the London penetration depth λ_L, the first term with the supercurrent deep into the superconductor

will be negligible, thus, equation (5.2) becomes

$$\nabla\varphi = \frac{2e\mathbf{A}}{\hbar}. \tag{5.3}$$

Performing path integration respectively from point 1 to 2 and 3 to 4:

$$\varphi_2 - \varphi_1 = \int_1^2 \nabla\varphi \cdot d\mathbf{l} = \frac{2e}{\hbar}\int_1^2 \mathbf{A}\cdot d\mathbf{l}$$
$$\varphi_4 - \varphi_3 = \int_3^4 \nabla\varphi \cdot d\mathbf{l} = \frac{2e}{\hbar}\int_3^4 \mathbf{A}\cdot d\mathbf{l}$$

and summing them up, one gets the difference of the "phase difference" across the junction between x and $x+\Delta x$:

$$\begin{aligned}\varphi(x+\Delta x)-\varphi(x) &= (\varphi_4-\varphi_1)-(\varphi_3-\varphi_2) = (\varphi_2-\varphi_1)+(\varphi_4-\varphi_3)\\ &= \frac{2e}{\hbar}\oint \mathbf{A}\cdot d\mathbf{l} = \frac{2e}{\hbar}\int \mathbf{B}\cdot d\mathbf{S}\\ &= \frac{2e}{\hbar}B_y D\Delta x \ ,\end{aligned} \tag{5.4}$$

in which, $D = 2\lambda_L + d$ and B_y is the y-component of the magnetic field $\mathbf{B} = B_y(x,z)\mathbf{j}$, which has a relation $\mathbf{B} = \nabla\times\mathbf{A}$. Taking the limit $\Delta x \to 0$, we have

$$\partial_x\varphi = \frac{2eB_yD}{\hbar} \ . \tag{5.5}$$

Since the Maxwell's equation gives $\nabla\times\mathbf{B} = \mu_0\mathbf{J} + \mu_0\varepsilon\partial_t\mathbf{E}$, where μ_0 is the magnetic vacuum permeability, ε is electric permittivity of the insulator, and $\mathbf{E}$ is the electric field. Substituting the expression of the magnetic field in the Maxwell's equation above leads to

$$\partial_x B_y = \mu_0 J_z + \mu_0\varepsilon\partial_t E_z \ . \tag{5.6}$$

Taking the x derivative of equation (5.5) and combining it with (5.6), we have

$$\begin{aligned}\partial_x^2\varphi &= \frac{2eD}{\hbar}\partial_x B_y\\ &= \frac{2eD\mu_0}{\hbar}J_c\sin\varphi + \frac{2eD\mu_0\varepsilon}{\hbar}\partial_t E_z\\ &= \frac{1}{\lambda_J^2}\sin\varphi + \frac{\mu_0\varepsilon D}{d}\partial_t^2\varphi \ ,\end{aligned} \tag{5.7}$$

in which, the Josephson equations (1.8a) and (1.8b) have been used; the voltage across the junction is $V = E_z d$, and $\lambda_J = \left(\frac{\hbar}{2eD\mu_0 J_c}\right)^{1/2}$ is the Josephson penetration depth. Further, the spatial variable x and time t in equation (5.7) can be respectively normalized to λ_J and the zero-bias plasma frequency $\omega_{j0} = \sqrt{\frac{2eI_c}{\hbar C}}$, i.e., $x \to x' = x/\lambda_J$, and $t \to \tau = t/t_0$, where, $t_0 = 1/\omega_{j0}$. For convenience, in this chapter we will still use x and t as the variables rather than x' and τ. Thus, equation (5.7) becomes

$$\partial_t^2 \varphi - \partial_x^2 \varphi + \sin\varphi = 0 \tag{5.8}$$

This is the pure or perfect form of sine-Gordon equation in the absence of dissipation, external bias and noise.

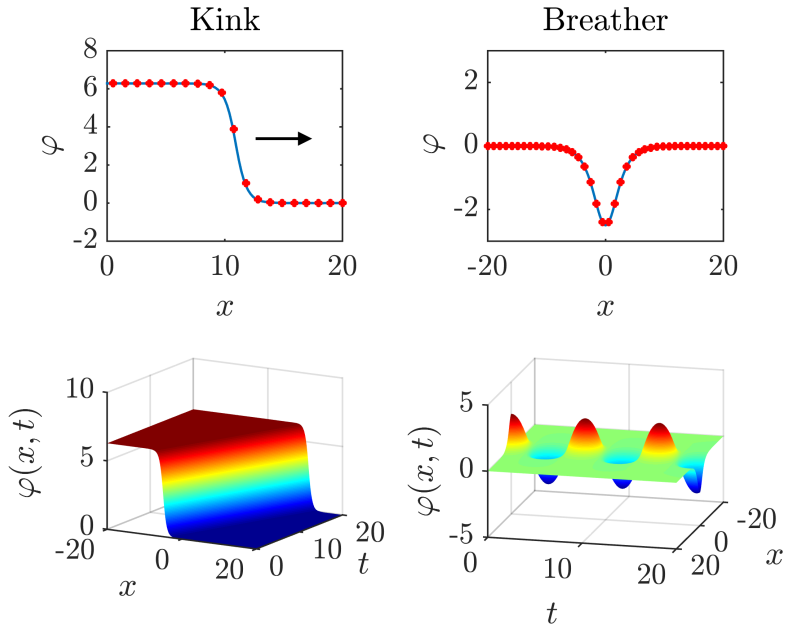

Figure 5.2. The kink (left, $c = 0.8$) and breather (right, $\omega = 0.8$) solitons at $t = 20$, generated by numerically solving the sine-Gordon equation, and the red dots represent the analytic solutions respectively given by (5.9) and (5.11). The lower two subplots are the corresponding 3D spatiotemporal plots.

5.1.1 Exact solution to the sine-Gordon equation

The typical solutions to the sine-Gordon equation include plasma mode, breather and kink solutions [96]. When a bias current, $\eta < 1$, is applied on the right-hand side of equation (5.8), as we have said in the previous chapters, this long junction system with a length L may be undergoing small oscillations around the minimum of potential $\varphi_{min} = \sin^{-1}\eta$, and

this kind of plasma oscillation is also called "phonon mode" [83], having a general solution as $\varphi(x,t) = \sqrt{\frac{2}{L}}\sum A_n(t)\cos(k_n x)$, where $k_n = n\pi/L$ with n being an integer. This is an often-seen model used for studying the vibration of crystal lattice. The other two are solitary waves and can be constructed by the convenient "Direct integration method". Let $\varphi(x,t) = f(x-vt+x_0)$, where v is the group velocity of wave and x_0 is an arbitrary constant. It can be shown that, for $v^2 < 1$, there is an exact travelling wave solution as [97]

$$\varphi(x,t) = 4\tan^{-1}\left[e^{\pm\frac{1}{\sqrt{1-v^2}}(x-vt+x_0)}\right] \tag{5.9}$$

For $v^2 > 1$, similarly, another travelling wave solution reads

$$\varphi(x,t) = -\pi + 4\tan^{-1}\left[e^{\pm\frac{1}{\sqrt{v^2-1}}(x-vt+x_0)}\right] \tag{5.10}$$

Both of these two kinds of solutions are travelling solitary wave solutions, but here we will just focus on the case of $v^2 < 1$, which represents the propagation of a single flux quantum through the junction. The "$\pm$" in the exponential factor represents kink or anti-kink soliton.

For standing wave solution, one can use a transformation $\varphi(x,t) = 4\tan^{-1}\frac{f(x)}{g(t)}$, and finally get

$$\varphi(x,t) = 4\tan^{-1}\left[\pm\sqrt{\frac{1-\omega^2}{\omega^2}}\frac{\sin\omega t}{\cosh(\sqrt{1-\omega^2}\cdot x)}\right] \tag{5.11}$$

where ω is the angular frequency. This solution is called breather soliton, which oscillates at a fixed location x and can be considered as nonlinear oscillating bound state formed by a kink-antikink pair [98]. Figure 5.2 shows the kink and breather solutions. Here, the kink is travelling to the right with speed of $v = 0.8$ and the breather is oscillating at $x = 0$ with angular frequency $\omega = 0.8$. In the following discussion about soliton/fluxon dynamics, we will use the kink solution represented by (5.9) to denote the soliton with initial position of x_0 and speed of v.

5.1.2 Thermal s-G equation, a more general form

In general, the dissipation and thermal fluctuation effects should be taken into account in the sine-Gordon equation. We consider the followings: (1) Like in the Langevin equation, a term $\alpha\dot{\varphi}$ that represents the resistance due to the normal electron current across the junction, $I_N =$

V/R, where V and R are respectively the voltage across the junction and junction resistance, should be added to equation (5.8). For an simple one-dimension long junction, there exists an additional normal electron current flowing parallel to the junction, leading to the surface resistance (skin damping) given by the term $\beta\partial_{xxt}\varphi$ [91, 99]. (2) Correspondingly, we let the noise terms that the damping terms intrinsically associated to respectively be n_α and ν_β, namely, local noise and non-local (surface) noise (see the spring-mass model in the following section). (3) Also, an external bias current $\eta = I/I_c$ can be applied to the junction (along the z-direction in the right subplot in Figure 5.1). Hence, the general one-dimensional sine-Gordon equation reads[1]

$$\partial_t^2\varphi - \partial_x^2\varphi + \alpha\partial_t\varphi - \beta\partial_{xxt}\varphi + \sin\varphi = \eta + n_\alpha(x,t) + \nu_\beta(x,t) \tag{5.12}$$

where the two damping coefficients α and β are positive, and the corresponding noises, n_α and ν_β, are Gaussian white noise [83]:

$$\langle n_\alpha(x,t)\rangle = 0 \tag{5.13}$$

$$\langle n_\alpha(x,t)n_\alpha(x',t')\rangle = 2\alpha\theta\delta(t-t')\delta(x-x') \tag{5.14}$$

and

$$\langle \nu_\beta(x,t)\rangle = 0 \tag{5.15}$$

$$\langle \nu_\beta(x,t)\nu_\beta(x',t')\rangle = 2\beta\theta\delta(t-t')\delta_{xx}(x-x') \tag{5.16}$$

where $\theta = k_BT/E_0$ is the normalized temperature with k_B being the Boltzmann constant; T, the temperature; E_0, the rest energy of the soliton having a form $E_0 = \frac{8\hbar J_c W\lambda_J}{2e}$ where W is the width of the junction [100]. Equations (5.12)$\sim$(5.24) will be the basis of the discussion in this Chapter and we will only concern about the kink soliton in (5.9), which describes the a magnetic flux (fluxon) moving along the junction.

5.2 Analogous mass-spring system

Similar to a small junction that can be analog to a simple pendulum in the gravitational field, the perfect sine-Gordon equation (5.8) is related to a mechanical system that consists of a series

[1]For convenience, in the following sections, we will use subscripts to denote the space and time derivatives of a variable, such as $\varphi_{xt} \equiv \partial_{xt}\varphi$.

of pendulums [99, 101]. Here, assuming the amplitude of the phase oscillation is sufficiently small, we use a linear spring-mass model [102] to investigate the effect of the resistive damping α and the surface damping β, and obtain the expressions of the corresponding discrete noise terms as we have given in (5.86) and (5.87). The detailed discussion and derivation can be found in Ref. [102]. It is worth noting that although this mechanical system is proposed for studying the sine-Gordon equation, it is also expected to applied to the actual physical systems such as periodic particle system, bubble dynamics, etc, like the Frenkel–Kontorova (FK) model did. A discussion on a similar spring-mass system can be found in [103]; inversely, the methods developed in this chapter would be applicable for studying those kinds of systems.

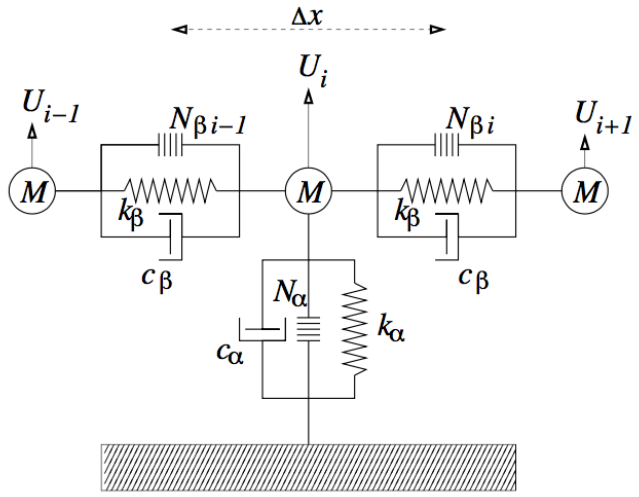

Figure 5.3. Analogous mass-spring system, from [102].

In Figure 5.3, the masses M at x_i can move in x-direction as the arrow indicates and are connected to their neighbors by springs k_β, dampers c_β and associated thermal noise sources $N_{\beta,i-1}$ and $N_{\beta,i}$, in order to simulate the (non-local) surface effects. Meanwhile, locally, a spring k_α, a damper c_α and a noise source N_α are exerted to the mass M at x_i. Thus, assuming the displacement of M is U_i, the equation motion reads

$$\begin{aligned} M\frac{d^2U_i}{dt^2} =& -k_\alpha U_i - c_\alpha\frac{dU_i}{dt} + N_{\alpha,i} - k_\beta(U_i - U_{i-1}) - k_\beta(U_i - U_{i+1}) \\ & - c_\beta\left(\frac{dU_i}{dt} - \frac{dU_{i-1}}{dt}\right) - c_\beta\left(\frac{dU_i}{dt} - \frac{dU_{i+1}}{dt}\right) + (N_{\beta,i-1} - N_{\beta,i}) \end{aligned} \tag{5.17}$$

where all of the noise terms are given by the fluctuation-dissipation theorem

$$\langle N_{*,i}(t)\rangle = 0 \tag{5.18}$$

$$\left\langle N_{*,i}(t)N_{*,j}(t')\right\rangle = 2c_{*,i}k_BT\,\delta(t-t')\delta_{ij} \tag{5.19}$$

where i means the i^{th} block and the "$*$" is α or β.

5.2.1 Normalization of the equation of motion

Measuring the displacement of M in unit of characteristic length r_0, distance Δx in unit of characteristic length x_0, and time in unit of characteristic time t_0, i.e., $U_i = u_i r_0$, $\Delta x = \Delta\xi x_0$ and $t = \tau t_0$, where u_i, $\Delta\xi$ and τ are the corresponding dimensionless quantities, equation (5.17) becomes

$$\begin{aligned}\ddot{u}_i = &-\left(\frac{k_\alpha t_0^2}{\rho\Delta x}\right)u_i - \left(\frac{c_\alpha t_0}{\rho\Delta x}\right)\dot{u}_i + \left(\frac{t_0^2}{\rho\Delta x r_0}\right)N_{\alpha,i} + \left(\frac{k_\beta\Delta x t_0^2}{\rho x_0^2}\right)\frac{u_{i-1}-2u_i+u_{i+1}}{\Delta\xi^2}\\ &+\left(\frac{c_\beta\Delta x t_0}{\rho x_0^2}\right)\frac{\dot{u}_{i-1}-2\dot{u}_i+\dot{u}_{i+1}}{\Delta\xi^2} + \left(\frac{t_0^2}{\rho\Delta x r_0}\right)(N_{\beta,i-1}-N_{\beta,i})\end{aligned} \tag{5.20}$$

where $\rho\Delta x = M$ and $\dot{u} \equiv \frac{du_i}{d\tau}$. Defining

$$\kappa_\alpha = \frac{k_\alpha t_0^2}{\rho\Delta x}, \quad \kappa_\beta = \frac{k_\beta t_0^2\Delta x}{\rho x_0^2}\ ; \tag{5.21}$$

$$\alpha = \frac{c_\alpha t_0}{\rho\Delta x}, \quad \beta = \frac{c_\beta\Delta x t_0}{\rho x_0^2}\ ; \tag{5.22}$$

$$n_{\alpha,i}(\tau) = \left(\frac{t_0^2}{\rho\Delta x r_0}\right)N_{\alpha,i}(t)\ ; \tag{5.23}$$

$$\nu_{\beta,i}(\tau) = n_{\beta,i-1} - n_{\beta,i} = \left(\frac{t_0^2}{\rho\Delta x r_0}\right)\left[N_{\beta,i-1}(t) - N_{\beta,i}(t)\right]\ , \tag{5.24}$$

equation (5.20) becomes

$$\ddot{u}_i = -\kappa_\alpha u_i - \alpha\dot{u}_i + n_{\alpha,i} + \kappa_\beta\frac{u_{i-1}-2u_i+u_{i+1}}{\Delta\xi^2} + \beta\frac{\dot{u}_{i-1}-2\dot{u}_i+\dot{u}_{i+1}}{\Delta\xi^2} + \nu_{\beta,i}, \tag{5.25}$$

where n_α is the local noise and ν_β is the non-local noise constructed by two local noises. On the other hand, based on (5.19), the properties of the normalized local noise now are given as

$$\langle n_{\alpha,i}(\tau)\rangle = 0 \tag{5.26}$$

$$\begin{aligned}\langle n_{\alpha,i}(\tau)n_{\alpha,j}(\tau')\rangle &= \left(\frac{t_0^2}{\rho\Delta x r_0}\right)^2 \langle N_{\alpha,i}(t)N_{\alpha,j}(t')\rangle \\ &= \left(\frac{t_0^2}{\rho\Delta x r_0}\right)^2 2c_{\alpha,i}k_BT\,\delta(t-t')\delta_{ij} \\ &= 2\alpha\theta\left(\frac{\delta_{ij}}{\Delta\xi}\right)\delta(\tau-\tau')\end{aligned} \tag{5.27}$$

where $\theta = k_BT/E_0$ is the normalized temperature with $E_0 = \rho x_0 r_0^2/t_0^2$ (not the rest energy in the last section). Similarly, the autocorrelation of the non-local noise ν_β given in (5.24) is descrived by

$$\langle \nu_{\beta,i}(\tau)\rangle = 0 \tag{5.28}$$

$$\begin{aligned}\langle \nu_{\beta,i}(\tau)\nu_{\beta,j}(\tau')\rangle &= (n_{\beta,i-1}-n_{\beta,i})(n_{\beta,j-1}-n_{\beta,j}) \\ &= \left(\frac{t_0^2}{\rho\Delta x r_0}\right)^2 \langle (N_{\beta,i-1}-N_{\beta,i})(N_{\beta,j-1}-N_{\beta,j})\rangle \\ &= -2\beta\theta\delta(\tau-\tau')\left(\frac{1}{\Delta\xi^3}\right)\times\begin{cases}1, & j=i-1\\ -2, & j=1\\ 1, & j=i+1\\ 0, & \text{else}\end{cases}\end{aligned} \tag{5.29}$$

in which, the local noise (n_β) that constructs the non-local noise (ν_β) satisfies

$$\langle n_{\beta,i}(\tau)\rangle = 0 \tag{5.30}$$

$$\langle n_{\beta,i}(\tau)n_{\beta,j}(\tau')\rangle = 2\beta\theta\left(\frac{\delta_{ij}}{\Delta\xi^3}\right)\delta(\tau-\tau') \tag{5.31}$$

5.2.2 From discrete to continuum

Taking the limit $\Delta\xi \to 0$, we assume the coefficients in (5.21) and (5.22) remain non-zero or finite; meanwhile, the central differences in equation (5.25) become

$$\frac{u_{i-1} - 2u_i + u_{i+1}}{\Delta\xi^2} \to u_{\xi\xi} \tag{5.32}$$

$$\frac{\dot{u}_{i-1} - 2\dot{u}_i + \dot{u}_{i+1}}{\Delta\xi^2} \to \dot{u}_{\xi\xi} \tag{5.33}$$

On the other hand, since the spatial function $f_{\Delta\xi} = \delta_{ij}/\Delta\xi$ in (5.27) satisfies

$$\lim_{\Delta\xi\to 0}\int_{-\infty}^{+\infty}\left(\frac{\delta_{ij}}{\Delta\xi}\right)d\xi = \begin{cases} 1, & |\xi_j - \xi_i| \le \frac{\Delta\xi}{2} \to 0 \ (i = j) \\ 0, & |\xi_j - \xi_i| > \frac{\Delta\xi}{2} \to 0 \ (i \ne j) \end{cases},$$

it is a Dirac δ-function, i.e., $\delta_{ij}/\Delta\xi \to \delta(\xi - \xi')$ for $\Delta\xi \to 0$, so that (5.27) becomes

$$\left\langle n_\alpha(\tau,\xi) n_\alpha(\tau',\xi')\right\rangle = 2\alpha\theta\delta(\tau - \tau')\delta(\xi - \xi') \tag{5.34}$$

Similarly, taking the limit of the integral of the spatial function in (5.29):

$$g_{\Delta\xi}(\xi) = \left(\frac{1}{\Delta\xi^3}\right) \times \begin{cases} 1, & j = i-1, \ \ \xi_j - \xi_i \in (-\frac{3}{2}\Delta\xi, -\frac{1}{2}\Delta\xi] \\ -2, & j = 1, \ \ \xi_j - \xi_i \in (-\frac{1}{2}\Delta\xi, \frac{1}{2}\Delta\xi] \\ 1, & j = i+1, \ \ \xi_j - \xi_i \in (\frac{1}{2}\Delta\xi, \frac{3}{2}\Delta\xi] \\ 0, & \text{else} \end{cases},$$

then results in

$$\lim_{\Delta\xi\to 0}\int_{-\infty}^{+\infty} g_{\Delta\xi}(\xi) = \frac{f_{\Delta\xi}(\xi - \Delta\xi) - 2f_{\Delta\xi}(\xi) + f_{\Delta\xi}(\xi + \Delta\xi)}{\Delta\xi^2} = \delta_{\xi\xi} \ ,$$

thus,

$$\left\langle \nu_\beta(\tau,\xi)\nu_\beta(\tau',\xi')\right\rangle = -2\beta\theta\delta(\tau - \tau')\delta_{\xi\xi}(\xi - \xi') \tag{5.35}$$

Putting the considerations (5.32) $\sim$ (5.35) into equation (5.25), we obtain the continuous form for the governing equation (5.17) of the spring-mass system as

$$\ddot{u} = -\kappa_\alpha u - \alpha\dot{u} + n_\alpha + \kappa_\beta u_{\xi\xi} + \beta\dot{u}_{\xi\xi} + \nu_\beta \tag{5.36}$$

By choosing $\kappa_\alpha = \kappa_\beta = 1$, this equation will be indentical to the linear form of the sine-Gordon equation (5.12). This implies that the forms of the autocorrelations of the local and non-local noises (5.27) and (5.31) tell us what the magnitudes of the noises should be in the simulation (see the section "discretization of the sine-Gordon equation") .

5.3 Fourier analysis for the equation of motion

Let's have a look at the continuous sine-Gordon equation and the discrete governing equation of the spring-mass system in the momentum (k) space.

5.3.1 Continuous sine-Gordon equation

When the amplitude of the oscillation is small, the approximation $\sin\varphi \approx \varphi$ holds, so the the sine-Gordon equation (5.12) becomes

$$\varphi_{tt} - \varphi_{xx} + \alpha\varphi_t - \beta\varphi_{xxt} + \varphi = \eta + n_\alpha(x,t) + \nu_\beta(x,t) \tag{5.37}$$

Applying Fourier transform, such as $\tilde{\varphi}(k,t) = \frac{1}{\sqrt{L}}\int_0^L \varphi(x,t)e^{-ikx}dx$, to each term in this equation, we have

$$\tilde{\varphi}_{tt} + (\alpha + \beta k^2)\tilde{\varphi}_t + (1+k^2)\tilde{\varphi} = \tilde{n}_\alpha - \tilde{\nu}_\beta \tag{5.38}$$

Here, k is the wave number and L is the length of the long junction. Equation (5.38) is the evolution equation of the phase $\varphi(x,t)$ in k-space. In k-space, the mean of the local noise (corresponding to the resistive damping) n_α described by (5.13) and (5.14) with periodic boundary is

$$\langle \tilde{n}_\alpha(k,t)\rangle = \frac{1}{\sqrt{L}}\int_0^L \langle n_\alpha(x,t)\rangle\, e^{-ikx}dx = 0 \tag{5.39}$$

and autocorrelation is

$$\begin{aligned}
\left\langle \tilde{n}_\alpha(k,t)\tilde{n}^*_\alpha(k',t')\right\rangle &= \left\langle \frac{1}{\sqrt{L}}\int_0^L n_\alpha(x,t)e^{-ikx}dx \cdot \frac{1}{\sqrt{L}}\int_0^L n_\alpha(x',t')e^{ik'x'}dx' \right\rangle \\
&= 2\alpha\theta\delta(t-t')\begin{cases} 0, & k \neq k' \\ 1, & k = k' \end{cases} \\
&= 2\alpha\theta\delta(t-t')\delta_{mn}
\end{aligned} \tag{5.40}$$

Here, we have applied the sifting property of δ-function. Since it is finite space, k is discrete, i.e., $k = \frac{2\pi n}{L}$, $k' = \frac{2\pi m}{L}$, where $n, m = 0, 1, 2, ..., N-1$, with N being the number of nodes. Hence, expressions (5.39) and (5.40) show that the local noise n_α in k-space is still white noise. It can be proved that in infinite space $x \in (-\infty, +\infty)$, where k is continuous, following still holds:

$$\langle \tilde{n}_\alpha(k,t) \rangle = 0 \tag{5.41}$$

$$\left\langle \tilde{n}_\alpha(k,t) \tilde{n}^*_\alpha(k',t') \right\rangle = 2\alpha\theta\delta(t-t')\delta(k-k') \tag{5.42}$$

Similarly, for non-local noise that corresponding to the skin damping due to surface resistance, we have

$$\begin{aligned} \left\langle \tilde{v}_\beta(k,t) \right\rangle &= 0 \\ \left\langle \tilde{v}_\beta(k,t) \tilde{v}^*_\beta(k',t') \right\rangle &= -2(\beta k^2)\theta\delta(t-t')\delta_{mn} \end{aligned} \tag{5.43}$$

in which, $k = \frac{2\pi n}{L}$, $k' = \frac{2\pi m}{L}$, with $n, m = 0, 1, 2, ..., N-1$; the derivative theorem of Fourier transform has applied to the δ-function. Still, if the system is infinite, we will have

$$\left\langle \tilde{v}_\beta(k,t) \right\rangle = 0 \tag{5.44}$$

$$\left\langle \tilde{v}_\beta(k,t) \tilde{v}^*_\beta(k',t') \right\rangle = -2\beta k^2 \theta\delta(t-t')\delta(k-k') \tag{5.45}$$

5.3.2 Discrete spring-mass equation

Applying discrete Fourier transform to the discrete equation of motion (5.25), we have

$$\ddot{\tilde{u}}_i + \left[\alpha + \frac{4\beta}{\Delta x^2}\sin^2\left(\frac{k\Delta x}{2}\right)\right]\dot{\tilde{u}}_i + \left[\kappa_\alpha + \frac{4\beta}{\Delta x^2}\sin^2\left(\frac{k\Delta x}{2}\right)\right]\tilde{u}_i = \tilde{n}_{\alpha,i} + \tilde{v}_{\beta,i} \tag{5.46}$$

To deal with the discrete second derivative in (5.25), the shift theorem is applied, that is, $\tilde{u}_{i\pm1} = \tilde{u}_i e^{\pm\bar{i}\left(\frac{2\pi n}{N}\right)i}$, which leads to the $\sin^2(*)$ terms in (5.46). For a finite k and a small Δx ($k\Delta x \to 0$), it is found that the terms with $\sin^2(*)$ will reduce to βk^2, resulting in an similar form identical to (5.38) if setting $\kappa_\alpha = 1$:

$$\ddot{\tilde{u}}_i + \left(\alpha + \beta k^2\right)\dot{\tilde{u}}_i + \left(1 + \beta k^2\right)\tilde{u}_i = \tilde{n}_{\alpha,i} + \tilde{v}_{\beta,i} \tag{5.47}$$

With the expression of discrete local noise in (5.28) and (5.29), we have

$$\langle \tilde{n}_{\alpha,n} \rangle = 0 \tag{5.48}$$

$$\langle \tilde{n}_{\alpha,m} \tilde{n}^*_{\alpha,n} \rangle = 2\alpha\theta\delta(t-t')\frac{\delta_{mn}}{\Delta x} \tag{5.49}$$

noting that the relation between k and n is $k = \frac{2\pi n}{L}$, $n = 0, 1, 2, ..., N-1$. Similarly, for non-local noise, we have

$$\left\langle \tilde{v}_\beta(k,t) \right\rangle = 0 \tag{5.50}$$

and

$$\begin{aligned}
\left\langle \tilde{v}_\beta(k,t)\tilde{v}^*_\beta(k',t') \right\rangle &= \left\langle \frac{1}{\sqrt{N}} \sum_{i=0}^{N-1} (n_{\beta,i-1} - n_{\beta,i}) e^{-\bar{i}kx} \cdot \frac{1}{\sqrt{N}} \sum_{j=0}^{N-1} (n_{\beta,j-1} - n_{\beta,j}) e^{\bar{i}k'x'} \right\rangle \\
&= \begin{cases} 0, & k \neq k' \\ 2\left[\frac{4\beta}{\Delta x^2}\sin^2\left(\frac{k\Delta x}{2}\right)\right]\theta\delta(t-t')\frac{1}{\Delta x}, & k = k' \end{cases} \\
&= 2\left[\frac{4\beta}{\Delta x^2}\sin^2\left(\frac{k\Delta x}{2}\right)\right]\theta\delta(t-t')\frac{\delta_{mn}}{\Delta x}
\end{aligned} \tag{5.51}$$

Noting that the "damping coefficient" is consistent with the one in equation (5.46), if $k\Delta x$ is small enough, the correlation function will become:

$$\left\langle \tilde{v}_\beta(k,t)\tilde{v}^*_\beta(k',t') \right\rangle = 2\beta k^2 \theta\delta(t-t')\frac{\delta_{mn}}{\Delta x} \tag{5.52}$$

Up to now, it has been shown that, besides the equations of motion themselves and the noises are equivalent in physical space (see last section), they are also have equivalent forms in k-space. Particularly, the local and non-local noises in k-space are uncorrelated under different k's, no matter if it is continuous or discrete. This also implies that their solutions should be statistically independent under different modes.

Actually, now we have noticed that, since the spring-mass system in Figure 5.3 is a 3-point system - a mass M is influenced by its two neighbors, thus one may transform its equation of motion with 3-point central finite difference, and then obtain a continuous partial differential equation, which is equivalent to the linear sine-Gordon equation; inversely, the sine-Gordon equation can also be discretized with the 3-point central difference. However, if one approximates the sine-Gordon equation with a 5-point central difference, is there such a spring-mass system and corresponding discrete equation that can get back to the continuous equation and the noises are uncorrelated in k-space? We will put the answer to this question in the appendix.

5.4 Fluxon Dynamics

In long Josephson junctiom, a fluxon is induced by circulating supercurrents and acts like a solitary wave (e.g., kink soliton[2]) described by the sine-Gordon equation, or like a particle centered at its mathematical center, described by an equation of fluxon dynamics, which can be derived from the sine-Gordon equation. As mentioned above, besides the phonon modes (plasma oscillations), if solitons are present in the long Josephson system, it can be found that the soliton itself obeys some kind of equation of motion as well. Let's first define the energy and momentum of sine-Gordon system that satisfies equation (5.12)

$$\varphi_{tt} - \varphi_{xx} + \alpha\varphi_t - \beta\varphi_{xxt} + \sin\varphi = \eta + n_\alpha(x,t) + \nu_\beta(x,t) \quad ,$$

as [91, 104]

$$H \equiv \int_{-\infty}^{\infty} \left[\frac{1}{2}\left(\varphi_t^2 + \varphi_x^2\right) + (1 - \cos\varphi) \right] dx = E \tag{5.53}$$

and

$$P \equiv -\int_{-\infty}^{\infty} \varphi_t \varphi_x dx \tag{5.54}$$

Thus, for the soliton travelling along the long junction, by substituting the kink solution given in (5.9):

$$\varphi(x,t) = 4\tan^{-1}\left[e^{\pm\frac{1}{\sqrt{1-v^2}}(x-vt+x_0)} \right]$$

in the Hamiltonian (5.53) and momentum (5.54), we have

$$E = m\gamma \tag{5.55}$$

$$P = m\gamma v \tag{5.56}$$

where $m = 8$ is the "effective mass" [105] of the soliton with x_0 is being position, and $\gamma = (1-v^2)^{-1/2}$ is the Lorentz factor with v being the speed of soliton. Thus, the kink can be treated as a relativistic particle that satisfies the energy-momentum-mass relation $E^2 = P^2 + m^2$. Note that (5.56) implies the velocity of the soliton in terms of momentum is $v \equiv \frac{dX_0}{dt} = \frac{P}{\sqrt{m^2+P^2}}$, where

[2] In this thesis, we assume solitary wave and soliton refer to the same thing, i.e., the solitary wave solutions of sGE.

X_0 is the position of the soliton or the center of the kink. In the absence of the noise terms, the time derivative of the Hamiltonian (5.53) is

$$\begin{aligned}\frac{dE}{dt} &= \int_{-\infty}^{\infty} (\varphi_{tt}\varphi_t + \varphi_x\varphi_{xt} + \varphi_t \sin\varphi)\, dx \\ &= -\int_{-\infty}^{\infty} \left(\alpha\varphi_t^2 + \beta\varphi_{xt}^2 - \eta\varphi_t\right) dx \end{aligned} \tag{5.57}$$

It can be seen that the damping terms dissipate the energy of the system while the force term or bias current η is adding energy. That is, if $\alpha = \beta = 0$ and $\eta = 0$, it becomes $\frac{dE}{dt} = 0$ - the energy of the fluxon governed by the perfect sine-Gordon equation (5.8) will be conserved. The same procedure can be applied to the the change of the momentum in time. According to the definition (5.54), we have

$$\frac{dP}{dt} = -\alpha\int_{-\infty}^{\infty} \varphi_t\varphi_x dx + \beta\int_{-\infty}^{\infty} \varphi_{xt}\varphi_{xx} dx - \int_{-\infty}^{\infty} \varphi_x(n_\alpha - \nu_\beta) dx + 2\pi\eta \tag{5.58}$$

It is clear that for the undamped and unbias case described by the pure sine-Gordon equation (5.8), the momentum is conserved as well. Inserting the kink solution (5.9) into (5.58) resulting in the equation of motion of the soliton as

$$\frac{dP}{dt} = -\alpha P - \frac{1}{3}\beta P\left[1 + \left(\frac{P}{8}\right)^2\right] + 2\pi\eta + \varepsilon(t) \tag{5.59}$$

where $\varepsilon(t) = \int_{-\infty}^{\infty} \varphi_x(n_\alpha - \nu_\beta) dx$, which can be proved to satisfy

$$\langle\varepsilon(t)\rangle = 0 \tag{5.60}$$

$$\left\langle\varepsilon(t)\varepsilon(t')\right\rangle = 2\gamma\left(\alpha + \frac{\beta}{3}\right)\left(\frac{k_B T}{E_0}\right)\delta(t - t') \tag{5.61}$$

This means $\varepsilon(t)$ is also describing a white noise.

5.4.1 Diffusive soliton

When the bias current η is zero, the soliton is driven by the noise only, so the speed is small ($P \to 0,\ \gamma \to 1$) and (5.59) can be further reduced to

$$\frac{dP}{dt} = -\left(\alpha + \frac{\beta}{3}\right)P + \varepsilon(t) \tag{5.62}$$

This is a typical Langevin equation describing a motion of a Brownian particle. Using a standard method from textbooks of statistical mechanics, we can calculate the quantity: $\left\langle (\Delta P)^2 \right\rangle = \left\langle [P(t) - \langle P(t) \rangle]^2 \right\rangle$, as[3]

$$\left\langle (\Delta P)^2 \right\rangle = \left(\frac{k_B T}{E_0} \right) \left(1 - \mathrm{e}^{-2\bar{\alpha} t} \right) = \begin{cases} 2\bar{\alpha} \left(\frac{k_B T}{E_0} \right) t, & 0 < t \ll 1/\alpha \\ \frac{k_B T}{E_0}, & t \gg 1/\alpha \end{cases} \tag{5.63}$$

where $\bar{\alpha} = \alpha + \beta/3$. We can see that at the beginning of the motion, the momentum of the drifting particle is increasing linearly. Comparing to the Einstein relation for momentum [106], $\left\langle (\Delta P)^2 \right\rangle = 2D_p t$, with D_p being the diffusion coefficient of momentum, one gets $D_p = (\alpha + \beta/3)(k_B T/E_0)$. As the time goes by, the particle will ultimately attain thermal equilibrium, so that $\langle \Delta P \rangle = P(0) = 0$, thus, we have $\left\langle P^2 \right\rangle = k_B T/E_0$, i.e., the kinetic energy of the soliton will be

$$\langle E_k \rangle = \frac{\left\langle (\Delta P)^2 \right\rangle}{2m} = \left(\frac{k_B T}{2mE_0} \right) . \tag{5.64}$$

where $m = 8$ is the effective mass of the soliton. On the other hand, still for the case $t \gg 1/\alpha$, with the displacement of the soliton, $X(t) = \frac{1}{m} \int_0^t P(t')dt'$, one can calculate the quantity $\left\langle (\Delta X)^2 \right\rangle$, which will be[4]

$$\left\langle (\Delta X)^2 \right\rangle = \frac{2k_B T/E_0}{m(\alpha + \beta/3)} t . \tag{5.65}$$

Comparing it to the Einstein relation for displacement, $\left\langle (\Delta X)^2 \right\rangle = 2D_x t$, gives the diffusion coefficient as

$$D_x = \frac{k_B T/E_0}{m(\alpha + \beta/3)} \tag{5.66}$$

5.4.2 Confined soliton

Let's consider a perturbed sine-Gordon equation that reads

$$\varphi_{tt} - \varphi_{xx} + \alpha\varphi_t - \beta\varphi_{xxt} + \sin\varphi = -\kappa(\langle \varphi(t) \rangle - \langle \varphi_0 \rangle) + n_\alpha(x,t) + \nu_\beta(x,t) \quad ,$$

[3]Integrating equation (5.62) and taking time average, we have $\langle \Delta P(t) \rangle = \langle \Delta P(0) \rangle \mathrm{e}^{-\bar{\alpha} t}$; by the definition of $\left\langle (\Delta P)^2 \right\rangle$ and using the autocorrelation (5.61) then leads to (5.63).

[4]Integrating equation (5.62), one has $\Delta P(t) = P(0)\mathrm{e}^{-\bar{\alpha} t} + \int_0^t \varepsilon(t')\mathrm{e}^{-\bar{\alpha}(t-t')}dt$; then the autocorelation function of momentum will be $\langle P(t)P(t') \rangle = (k_B T/E_0)\mathrm{e}^{-\bar{\alpha}|t-t'|}$. Using the definition of $X(t)$ one gets an expression of $\left\langle (\Delta X)^2 \right\rangle$, combining which with the autocorelation function of momentum will lead to (5.65).

that is, the bias current or force term in equation (5.12) takes the form $\eta = -\kappa(\langle\varphi\rangle - \langle\varphi_0\rangle)$, where $\kappa > 0$ is a constant, $\langle\varphi(t)\rangle = \frac{1}{L}\int_0^L \varphi dx$ is the average phase through the long junction with L being its length. Let the equilibrium of the kink be at the mid-point, i.e., $X_0 = L/2$, then correspondingly, $\langle\varphi_0\rangle = (2\pi \cdot L/2)/L = \pi$. Here, η is to simulate an elastic restoring force like "$f = kx$", so we expect that the soliton is an harmonic oscillator trapped in a quadratic potential well. Since the area below the curve of the kink (5.9) at time t is $S(t) = \int_0^L \varphi dx$ and the upper and lower boundary of the kink is 2π, if the kink soliton travels a distance $\Delta X = X(t') - X(t)$ during $\Delta t = t' - t$, the change of area below the curve will be $\Delta S = S(t') - S(t) = 2\pi\Delta X$. With this consideration, the force term can be expressed as

$$\eta = -\kappa(\langle\varphi\rangle - \langle\varphi_0\rangle) = -\frac{\kappa}{L}[S(t) - S(0)] = -\frac{2\pi\kappa}{L}[X(t) - X(0)] \tag{5.67}$$

where $X(t) = L\langle\varphi\rangle/2\pi$, so that the equilibrium position of the soliton is $X_0 = X(0) = L/2$. Hence, inserting η into equation (5.59) leads to

$$\frac{dP}{dt} = -\alpha P - \frac{1}{3}\beta P\left[1 + \left(\frac{P}{8}\right)^2\right] - \left(\frac{4\pi^2\kappa}{L}\right)[X(t) - X_0] + \varepsilon(t) \tag{5.68}$$

Since $P \approx m\gamma(v)v$ with $m = 8$ and $v = \dot{X}$, under small-velocity approximation, one has $\gamma \to 1$ and $P = m\dot{X}$. For convenience, we count the displacement of the soliton relative to the equilibrium position: $X(t) \to X(t)' = X(t) - X_0$, but still use the old notation "$X(t)$" in the equation; thus, the equation of motion of the confined soliton in a potential well is obtained as

$$m\ddot{X} + m\left(\alpha + \frac{\beta}{3}\right)\dot{X} + \kappa_e \cdot X = \varepsilon(t) \tag{5.69}$$

where $\kappa_e = 4\pi^2\kappa/L$ is the effective elastic constant. This means the soliton is oscillating in the quadratic potential $U(X) = \frac{1}{2}\kappa_e X^2$. Once thermal equilibrium is attained, the Boltzmann distribution is satisfied:

$$\rho(X) = \rho_0 \mathrm{e}^{-\frac{U(X)}{k_B T/E_0}} = \rho_0 \mathrm{e}^{-\frac{X^2}{2k_B T/\kappa_e}} \tag{5.70}$$

where ρ_0 is the normalization constant. This gives the standard deviation for the distribution of the position or displacement of the soliton as

$$\sigma_x = \left(\frac{\theta L}{4\pi^2\kappa}\right)^{1/2} \tag{5.71}$$

where $\theta = k_B T/E_0$.

5.5 Discretization of the sine-Gordon equation

To perform numerical simulation for the fluxon dynamics, the continuous sine-Gordon equation (5.12) has to be discretized. An principal requirement is the statistical quantities, such as potential and kinetic energies, can be time-step invariant within the stability range. Inspired by the GJ algorithm [59] used for the Langevin simulations in the previous chapters, here, we generalize it for solving the partial differential equation (sGE).

5.5.1 The u-equation

Letting $u \equiv \varphi$ and $v \equiv \varphi_t = u_t$, following we will derive a scheme for u and v. For equation (5.12) with zero bias, $\eta = 0$:

$$\varphi_{tt} - \varphi_{xx} + \alpha\varphi_t - \beta\varphi_{xxt}\sin\varphi = n_\alpha(x,t) + \nu_\beta(x,t) \ ,$$

integrating the both sides from t_n to t_{n+1} leads to

$$v^{n+1} - v^n = \int_{t_n}^{t_{n+1}} (u_{xx} - \sin u)dt + \beta(u_{xx}^{n+1} - u_{xx}^n) - \alpha(u^{n+1} - u^n) + n_\alpha - \nu_\beta \tag{5.72}$$

where the discrete noise terms read

$$n_\alpha = \int_{t_n}^{t_{n+1}} n_\alpha(x,t')dt' \tag{5.73}$$

$$\nu_\beta = \int_{t_n}^{t_{n+1}} \nu_\beta(x,t')dt' \tag{5.74}$$

On the other hand, integrating the both side of the expression $v = \frac{du}{dt}$ by trapezoidal rule, one has

$$u^{n+1} - u^n = \frac{\Delta t}{2}\left(v^n + v^{n+1}\right) \tag{5.75}$$

Substituting the v^{n+1} in (5.72) and (5.75)

$$\begin{aligned} u^{n+1} - u^n = \frac{\Delta t}{2}\Bigg[2v^n + \int_{t_n}^{t_{n+1}} (u_{xx} - \sin u)dt \\ + \beta(u_{xx}^{n+1} - u_{xx}^n) - \alpha(u^{n+1} - u^n) + n_\alpha - \nu_\beta\Bigg] \end{aligned} \tag{5.76}$$

and letting the integral on the right-hand-side of (5.76) be $(u_{xx} - \sin u)\Delta t$ leading to

$$\begin{aligned} u^{n+1} - u^n = \Delta t v^n + \frac{\Delta t^2}{2}\left[u_{xx}^n - \sin u^n + \frac{\beta}{\Delta t}\left(u_{xx}^{n+1} - u_{xx}^n\right)\right] \\ - \frac{\alpha\Delta t}{2}\left(u^{n+1} - u^n\right) + \frac{\Delta t}{2}\left(n_\alpha - \nu_\beta\right) \end{aligned} \tag{5.77}$$

Combining the $u^{n+1}-u^n$ terms in (5.77) yields an implicit equation for u^{n+1}:

$$u^{n+1} = u^n + b\Delta t v^n + \frac{b\Delta t^2}{2}\left[u^n_{xx} - \sin u^n + \frac{\beta}{\Delta t}(u^{n+1}_{xx} - u^n_{xx})\right] + \frac{b\Delta t}{2}(n_\alpha - \nu_\beta) \tag{5.78}$$

in which, $b = \frac{1}{1+\frac{\alpha dt}{2}}$. If letting $f = u^n_{xx} - \sin u^n + \frac{\beta}{\Delta t}(u^{n+1}_{xx} - u^n_{xx})$, equation (5.78) becomes

$$u^{n+1} = u^n + b\Delta t v^n + \frac{b\Delta t^2}{2} f + \frac{b\Delta t}{2}(n_\alpha - \nu_\beta) \tag{5.79}$$

This has the same form as that of the single Brownian particle in [59] and f is the external force acting on the particle or each node. The second-order position derivative of u in finite difference form can be $u_{xx} = \frac{u_{i-1}-2u_i+u_{i+1}}{\Delta x^2}$, where i denotes the i^{th} node. Hence, keeping the old u^n_{xx} terms on the right-hand-side and moving all of the new u^{n+1} terms to the left, we obtain the final version of the position equation:

$$\left(-\frac{\beta b\Delta t}{2\Delta x^2}\right)u^{n+1}_{i-1} + \left(1 + \frac{\beta b\Delta t}{\Delta x^2}\right)u^{n+1}_i + \left(-\frac{\beta b\Delta t}{2\Delta x^2}\right)u^{n+1}_{i+1} =$$
$$u^n_i + b\Delta t v^n_i + \frac{b\Delta t^2}{2}\left[\left(1 - \frac{\beta}{\Delta t}\right)u^n_{xx} - \sin u^n_i\right] + \frac{b\Delta t}{2}(n_\alpha - \nu_\beta) \tag{5.80}$$

This is a tridiagonal system of equations that need to be solved for $u = \varphi$.

5.5.2 The v-equation

We still need an discretized equation for $v = u_t$. Let's get back to the integral in equation (5.72) and let

$$\int_{t_n}^{t_{n+1}} (u_{xx} - \sin u)dt = \frac{dt}{2}\left[(u^{n+1}_{xx} - \sin u^{n+1}) + (u^n_{xx} - \sin u^n)\right]$$

so that

$$v^{n+1} - v^n = \frac{\Delta t}{2}\left[(u^{n+1}_{xx} - \sin u^{n+1}) + (u^n_{xx} - \sin u^n)\right]$$
$$+ \beta(u^{n+1}_{xx} - u^n_{xx}) - \alpha(u^{n+1} - u^n) + n_\alpha - \nu_\beta \tag{5.81}$$

which can be written as

$$v^{n+1} = v^n + \frac{\Delta t}{2}(f^n + f^{n+1}) + n_\alpha - \nu_\beta \tag{5.82}$$

where

$$f^n = u^n_{xx} - \sin u^n_i - \frac{2\beta}{\Delta t}u^n_{xx} + \frac{2\alpha}{\Delta t}u^n_i \tag{5.83}$$

$$f^{n+1} = u^{n+1}_{xx} - \sin u^{n+1}_i + \frac{2\beta}{\Delta t}u^{n+1}_{xx} - \frac{2\alpha}{\Delta t}u^{n+1}_i \tag{5.84}$$

Here $u_{xx} = \frac{u_{i-1}-2u_i+u_{i+1}}{\Delta x^2}$ and f^n and f^{n+1} are just the symbols for simplification and have nothing to do with the f or "force" term defined by (5.79). To obtain correct kinetic statistics, one might consider using the half-step velocity [60]:

$$v^{n+\frac{1}{2}} = \frac{u^{n+1} - u^n}{\sqrt{b}\Delta t} \tag{5.85}$$

So far, we have finished deriving the final programmable scheme (5.80) and (5.82) for respectively calculating the phase, $u = \varphi$, and the time derivative of the phase, $v = \varphi_t$, of each node along the discretized long Josephson junction.

5.5.3 Noise and boundary conditions

From the autocorrelation functions (5.27) and (5.31) of the local and non-local noises in the spring-mass system discussed in the previous chapters, the noise n_α corresponding to the resistive damping α due to the normal current can be expressed as

$$n_{\alpha,i} = \sqrt{2\alpha\theta\Delta t/\Delta x} \cdot \sigma_i \tag{5.86}$$

where σ_i is Gaussian random number generated by the "Ran2()" random-number generator [62], and the noise v_β corresponding to the surface/skin damping β due to the surface resistance will be

$$v_{\beta,i} = n_{\beta,i-1} - n_{\beta,i} \tag{5.87}$$

in which,

$$n_{\beta,i} = \sqrt{2\beta\theta\Delta t/\Delta x^3} \cdot \sigma_i \ . \tag{5.88}$$

where σ_i is another Gaussian random number. We will use Born-Von Karman (periodic) boundary conditions given as [102]

$$\begin{aligned} u_{-1} &= u_{N-1}, \quad v_{-1} = v_{N-1} \\ u_N &= u_0, \quad v_N = v_0 \end{aligned} \tag{5.89}$$

in which, the subscribes denote the $(*)^{th}$ nodes in the discretized long junction.

5.6 Results

The simulations presented in this chapter is to test the availability of the generalized GJ algorithm to the partial differential equation (sGE) and to test the understandings on the fluxon dynamics based on the spring-mass model. The diffusive and confined solitons will be used for the testing.

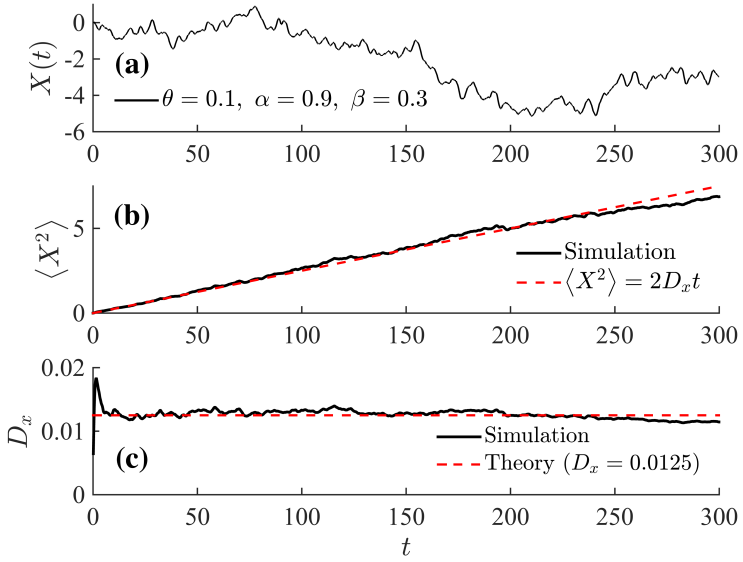

Figure 5.4. Diffusive soliton: (a) the displacement of soliton varying with time. The parameters are as shown on the plot. (b) the mean of $X(t)^2$, which increases with time linearly (solid line) and satisfies the Einstein relation (dash line). (c) The diffusion coefficient D_x by simulation and the comparison to the theoretical value.

5.6.1 Diffusive soliton

The soliton described by the long junction sine-Gordon equation (5.12) or the fluxon equation (5.62) is drifting under impact of noise in the absence of force terms. When the thermal equilibrium is attained, one can measure the diffusion constant of position by the Einstein relation $D_x = \left\langle (\Delta X)^2 \right\rangle / 2t$, where t is time and $\Delta X = X(t) - X(0)$ is the displacement of the soliton measured from the starting point. The theoretical value has been given by (5.71), that is, $D_x = \frac{k_B T / E_0}{m(\alpha + \beta/3)}$. Figure 5.4 shows the the position X, the mean square of position $\left\langle \Delta X^2 \right\rangle$, and the diffusion coefficient D_x of the soliton varying with time. In (a), we can see the soliton drifts around the starting point $X(0) = 0$ driven by noise. In (b), the mean square of position increases linearly with time and agrees well with the theory. In (c), the diffusion coefficient is maintained

around the theoretical value of 0.0125 after a short transient time. These results are as expected under the specific set of parameters $\alpha = \beta = 1,\ \theta = 0.1$. In Figure 5.5, we present the effect of the parameters in the expression of D_x. In (a) it can be seen that the D_x value is independent of the time step up to $\Delta t \sim 0.1$, beyond which, the measured D_x value will be divergent (not shown in the plot). In (b), D_x is proportional to temperature below $\theta = 0.5$ and higher than that it gradually deviates from the theoretical line. In (c) and (d), D_x agrees well with the theoretical curves as the functions of the two damping constants, α and β, within four orders of magnitude.

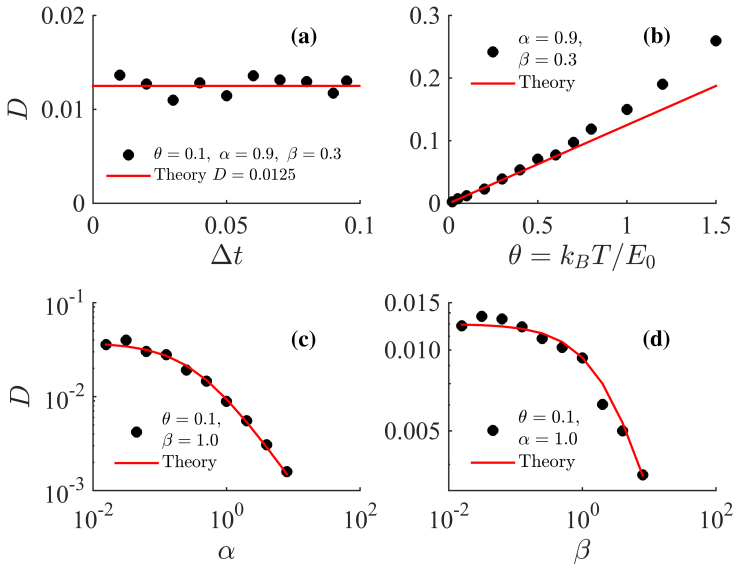

Figure 5.5. Diffusive soliton: (a) The time-step independence of the diffusion coefficient of the soliton, within the range shown in the plot. (b) The diffusion coefficient as a function of the normalized temperature θ. (c) and (d): The diffusion coefficient as a function of the two damping coefficients, α and β. The dots denote the results from simulations and the red solid curves represent the theoretical ones.

5.6.2 Confined soliton

The soliton described the equation (5.69) is driven by noise and effective restoring force. When the thermal equilibrium is attained, the position of the soliton should follow the Boltzmann distribution (5.70) with the theoretical standard deviation given by (5.71): $\sigma_x = \sqrt{\frac{\theta L}{4\pi^2 \kappa}}$, and the velocity should satisfy the Maxwell velocity distribution as well. In Figure 5.6, the parameters for the simulation are $\theta = 0.1,\ \alpha = \beta = 0.5,\ L = 4$ and $\kappa = 1.0$; the node spacing and the time step are respectively $\Delta x = 0.02$ and $\Delta t = 0.01$. Figure 5.6 (a) shows the trajectory of

the soliton in the phase space, performing a Brownian motion around the equilibrium points $(0,0)$. In (b) are the Boltzmann distribution for the soliton position and the typical Maxwell-Boltzmann distribution for the velocity by simulation compared to the theoretical curve (red, the expressions are shown on the plot). The standard deviations of the Boltzmann distribution for the position is measured to be $\sigma_x = 0.102$, which agree well with the theoretical value 0.1007. In Figure 5.7 shows the standard deviation as a function of temperature $\theta = k_B T/E_0$, effective elastic coefficient κ_e, distance Δx between two neighboring nodes on the distritized long junction, and the length of the junction L. We can see the results in (a) (b) and (d) match the corresponding theoretical curve produced by the expression (5.71); for (c) however, when the spacing between two neighboring nodes gets too large (~ 1), the measured σ_x starts deviation from the theoretical value.

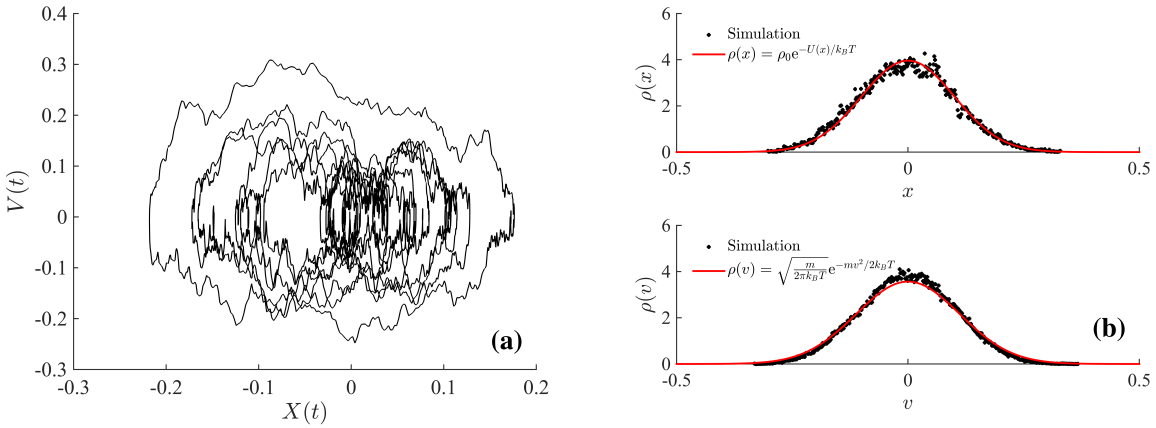

Figure 5.6. Confined soliton: (a) Trajectory of the soliton in phase space. (b) the Boltzmann distribution for the position and the Maxwell-Boltzmann distribution for the velocity by the simulation (dots) compared to the theory (red curve)]. The parameters in the simulation are $\theta = 0.1$, $\alpha = \beta = 0.5$, $L = 4$ and $\kappa = 1.0$. The node spacing and the time step are respectively $\Delta x = 0.02$ and $\Delta t = 0.01$.

5.7 Conclusion

In this chapter, we propose a spring-mass model analog to the one-dimensional long Josephson junction, and shows that the equation of this mechanical system can be mapped to the sine-Gordon equation of the long junction. With this model, we have a better understanding to the normal resistance and surface resistance in the long junction, and the corresponding noises, which is actually the local noise and non-local noise present in the spring-mass system, giving

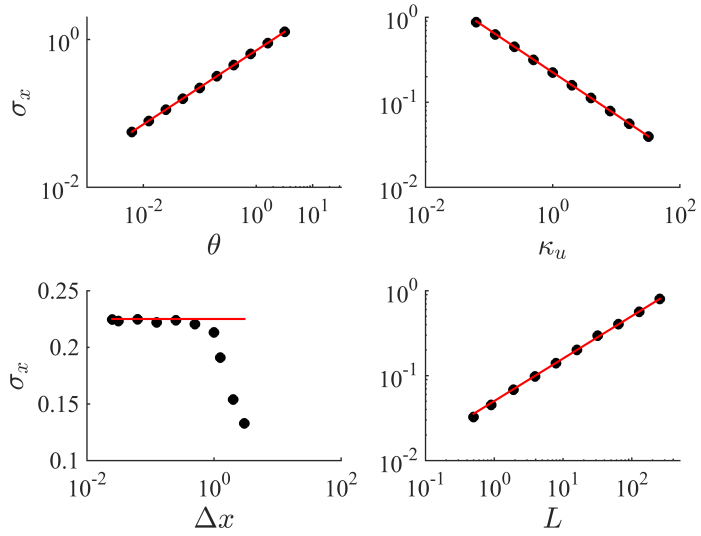

Figure 5.7. Confined soliton: the standard deviation of the Boltzmann distribution for the soliton position as a function of (a) temperature, (b) effective spring constant, (c) distance between neighboring nodes and (d) the length of the long junction. The dots denote the simulation results and the solid line is the theoretical one given by (5.71).

us specific forms for these two kinds of noises in the simulation. An Fourier analysis was done for investigating the noise properties in the wave-number (k) space, and it shows that the local and non-local noises in the k-space are still uncorrelated between any two modes, as expected. The spring-mass model itself could be a nice model applied to actual physical and engineering systems, and the relevant algorithm given in this chapter is also applicable tool for studying them.

On the other hand, we discretized the sine-Gordon equation using the method for deriving the GJF algorithm for Langevin simulation, generalizing this method so it can solve an partial different equation. To test the scheme, we performed simulations for the diffusive and confined solitons and compared the results to the existing theory of fluxon dynamics. Respectively, the diffusion coefficient of the diffusive soliton and the standard deviation of the Boltzmann distribution of the soliton position were measured and it was shown that the results were in accordance with the prediction of the theory. Besides, the confined soliton in a quadratic potential is shown attained thermal equilibrium - the position satisfies the Boltzmann distribution and the velocity follows the Maxwell-Boltzmann distribution.

This chapter is an extension of the previous chapters on single Josephson junction, but also

a prepared discussion for the future work, since the any idea presented in the previous chapters, such as saturation of SCD, chemical potential due to the plasma oscillation, etc., in principle, can be repeated on the long junction. Meanwhile, the long junction is a more complex system than single junction, meaning that it has more interesting mathematics and physics worthy to explore. This chapter is a starting point for the proceeding.

Chapter 6

Summary

In this thesis we discussed the switching problem of typical single Josephson junctions from Chapters 1 to 4, and long Josephson junction in Chapter 5. Chapter 1 is introductory and historical and physical background, basic equations and concepts of Josephson junction were presented. In Chapter 2, we demonstrated some non-equilibrium phenomena observed from the switching current distribution (SCD), where the information of switching of the junction is encoded. The switching of Josephson junction from superconductive state to the resistive state as the external bias current gets close to a critical current, can be analog to a Brownian particle (namely, phase particle) escaping from a tilting periodic potential well driven by thermal noise. We studied the effects of the bias current, temperature, damping, initial conditions of the phase to the SCD. Temperature determines the strength of the noise, which is one of a power sources of the Brownian particle. Increasing temperature may stimulate early switching of the junction. Damping is a drain of energy but also plays a role of media passing the energy to the particle from the noise. The damping and temperature have the system attained thermal equilibrium, which, however, can be destroyed by the increasing bias current, another power source for the phase particle. We confirmed by the simulations that the boundary between the equilibrium and the non-equilibrium is the unity of the ratio of damping coefficient to the the sweep rate ($\alpha/\dot{\eta} = 1$). When this ratio is low, the system would be in non-equilibrium state and the information from the initial conditions of the motion can be preserved until the escape takes place.

Thus, in Chapter 3, we continued studying the effects of the initial conditions under various

damping coefficients and temperatures, demonstrating how it affected the switching current. Since the characteristics of the initial conditions, including the width and position of the initial phase distribution, can be preserved if it is not damped out by the dissipation, one can observe the "saturation phenominon" of the SCD under $\alpha/\dot{\eta} \ll 1$. This phenomenon is interpreted by the theory of macroscopic quantum tunnelling (MQT) today, that is, the saturation SCD is due to the phase particle tunneling out of the barrier. At the end of this chapter, however, we showed that it is possible that giving an appropriate initial phase distribution can produce a temperature-independent SCD peak position curve comparable to experimental data.

In Chapter 4, based on the understanding on the saturation of SCD, and the chemical potential induced by the plasma oscillation given by the Anderson equation $\mu_0 = \hbar\omega_{j0}$, our first finding is that, in zero-temperature and zero-damping limits, just simply subtracting this potential energy from the potential height may lead to an escape current very close to the published experimental data, implying that the energy of plasma oscillation might be a key for the classical RCSJ model to successfully interpret the saturation of SCD observed in experiments. An improved Kramers model was then proposed for producing SCD using the parameters from the literature, and it was found that the peak-position curves agree well with the experimental data. On the other hand, by introducing the chemical potential to the initial conditions, we found that the peak position curve generated in Langevin simulation can be corrected in low temperatures as well. We conclude that the energy of the plasma oscillation is a necessary condition for the RCSJ model to describe the saturation phenomenon as MQT does, but we emphasize that the improved Kramers model is still incomplete and an model that can generate a correct width curve of SCD is required; in the improved Langevin simulation, there exist a free parameter for determining the width of the SCD. This is the problems to be solved in the future.

Chapter 5 is on long Josephson junction and can be treated as a prepared chapter for the future work, since all of the ideas on the switching problems of single Josephson junction should be able to be reproduced on the long junction. The long junction also has more complex physics, such as soliton dynamics. To understand the sine-Gordon equation, the governing equation of the long junction, a mechanical spring-mass model was proposed, and based on that, we generalized the GJ algorithm for solving the sine-Gordon equation. We applied this algorithm

on the soliton dynamics and obtained nice results.

Overall, this thesis proposed an alternative classical switching mechanism besides the MQT for single Josephson junction in low temperatures, and the key is the consideration of the chemical potential induced by the plasma oscillation. We expect that in the future this idea can be also verified on LJJ and a more complete model for the escape rate theory and Langevin simulation will be constructed as well.

Appendix A

Five-point system

A.1 Discrete equation for the 5-point spring-mass system

In Figure 5.3 we see a 3-point system, in which a mass is affected by its two neighbors, mathematically corresponding to a discrete equation with second-order finite difference as shown in equation (5.25):

$$u_{xx} = \frac{u_{i-1} - 2u_i + u_{i+1}}{\Delta x^2}$$

This is commonly seen in solid state physics when discussing the classical treatment for 1D lattice or linear chain. On the other hand, an partial differential equation can also be discretized by this 3-point finite difference. Now we ask: if one discretize, let say, the sine-Gordon equation with a 5-point finite difference with fourth-order accuracy:

$$u_{xx} = \frac{-u_{i-2} + 16u_{i-1} - 30u_i + 16u_{i+1} - u_{i+2}}{12\Delta x^2}, \tag{A.1}$$

does it correspond to a mass-spring system with one mass influenced by its five neighbors? Thus, here, we assume there exists such a unknown system and follow the same procedures in Chapter 5, to see if the noise still have a similar autocorrelation function under a 5-point approximation. Thus, for the discrete spring-mass equation of motion (5.25), it should be modified as

$$\ddot{u}_i = -\kappa_\alpha u_i - \alpha \dot{u}_i + \kappa_\beta \frac{-u_{i-2} + 16u_{i-1} - 30u_i + 16u_{i+1} - u_{i+2}}{12\Delta x^2} \tag{A.2}$$

$$+ \beta \frac{-\dot{u}_{i-2} + 16\dot{u}_{i-1} - 30\dot{u}_i + 16\dot{u}_{i+1} - \dot{u}_{i+2}}{12\Delta x^2} + n_{\alpha,i} + \nu_{\beta,i} \tag{A.3}$$

A.2 Discretization of the sGE with 5-point scheme

For the sine-Gordon equation discretized with the 5-point central differencing scheme, the u-equation (5.80) now turns into

$$\begin{aligned}
&\left(\frac{\beta b\Delta t}{24d\Delta x^2}\right)u_{i-2}^{n+1}+\left(-\frac{2\beta b\Delta t}{3\Delta x^2}\right)u_{i-1}^{n+1}+\\
&\left(1+\frac{5\beta bdt}{4\Delta x^2}\right)u_i^{n+1}+\left(-\frac{2\beta bdt}{3dx^2}\right)u_{i+1}^{n+1}+\left(\frac{\beta bdt}{24dx^2}\right)u_{i+2}^{n+1}\\
&=u_i^n+b\Delta t v_i^n+\frac{b\Delta t^2}{2}\left[\left(\kappa_\beta-\frac{\beta}{\Delta t}\right)u_{xx}^n-\kappa_\alpha u_i^n\right]+\frac{b\Delta t}{2}(n_\alpha-\nu_\beta)
\end{aligned}\tag{A.4}$$

which is a circulant penta-diagonal system of equation under periodic boundary conditions. The v-equation (5.82) becomes

$$v^{n+1}=v^n+\frac{dt}{2}(f^n+f^{n+1})+n_\alpha-\nu_\beta \tag{A.5}$$

where

$$f^n=\left(\kappa_\beta-\frac{2\beta}{dt}\right)u_{xx}^n-\left(\kappa_\alpha-\frac{2\alpha}{\Delta t}\right)u_i^n \tag{A.6}$$

$$f^{n+1}=\left(\kappa_\beta+\frac{2\beta}{\Delta t}\right)u_{xx}^{n+1}-\left(\kappa_\alpha+\frac{2\alpha}{\Delta t}\right)u_i^{n+1} \tag{A.7}$$

For convenience, the old u_{xx} terms are kept on the right-hand side of the u and v equations, but noting that they are approximated by the 5-point central finite difference in (A.1). The periodic boundary conditions are given as

$$\begin{aligned}
u_0&=u_{N-2}(+2\pi)\\
u_1&=u_{N-1}(+2\pi)\\
u_N&=u_0(-2\pi)\\
u_{N+1}&=u_1(-2\pi)
\end{aligned}\tag{A.8}$$

The 2π in the brackets are only for the soliton case, since the phase difference between the upper and lower boundaries is 2π.

A.2.1 Fourier Analysis for the discrete equation

Applying Fourier transform to the discrete equation of motion for the 5-point mechanical system described by (A.3), we have

$$\ddot{\tilde{u}}_i + \left[\alpha + \beta \frac{16\sin^2(k\Delta x/2) - \sin^2(k\Delta x)}{3\Delta x^2}\right] \dot{\tilde{u}}_i + \left[\kappa_\alpha + \kappa_\beta \frac{16\sin^2(k\Delta x/2) - \sin^2(k\Delta x)}{3\Delta x^2}\right] \tilde{u}_i = \tilde{n}_{\alpha,i} + \tilde{v}_{\beta,i} \tag{A.9}$$

Due to the periodic boundary conditions, $k\Delta x = \pi n/N$, $n = 0, 1, 2, ..., N-1$. The β and κ_β terms will respectively reduce to βk^2 and $\kappa_\beta k^2$ under long-wave approximation ($k\Delta x \to 0$), which is consistent with the continuous equation (5.38).

The local noise for the 5-point system is the same as in 3-point system (in physical or k-space). In k-space, it is given by

$$\begin{aligned} \langle \tilde{n}_\alpha(k,t) \rangle &= 0 \\ \left\langle \tilde{n}_\alpha(k,t) \tilde{n}^*_\alpha(k',t') \right\rangle &= 2\alpha\theta\delta(t-t')\delta_{mn} \end{aligned} \tag{A.10}$$

In the 3-point system, the non-local noise is defined by two neighboring local noises as $v_{\beta,i}(t) = n_{\beta,i-1}(t) - n_{\beta,i}(t)$, while for the 5-point system, however, it is not easy to be visualized as some kind of connections between neighboring nodes, but what can be expected is that the autocorrelation function in physical space should be able to transform to a continuous form under long-wave approximation, just like in (5.16):

$$\left\langle v_\beta(x,t) v_\beta(x',t') \right\rangle = 2\beta\theta\delta(t-t')\delta_{xx}(x-x') \tag{A.11}$$

Similar to (5.29), under the 5-point approximation, its discrete form should take

$$\left\langle v_{\beta,i}(t) v_{\beta,j}(t') \right\rangle = -2\beta\theta \frac{\delta(t-t')}{\Delta x^3} \times \frac{1}{12} \begin{cases} 0, & |i-j| \geq 3 \\ -1, & |i-j| = 2 \\ 16, & |i-j| = 1 \\ -30, & i = j \end{cases} \tag{A.12}$$

Meanwhile, inspired by the similar β terms in (5.46) and (5.51), from equation (A.9), one can predict that in k-space, the autocorrelation function would have the following form:

$$\left\langle \tilde{v}_{\beta,m}(t)\tilde{v}^{*}_{\beta,n}(t')\right\rangle = 2\beta\left[\frac{16\sin^2(k\Delta x/2)-\sin^2(k\Delta x)}{3\Delta x^2}\right]\theta\delta(t-t')\frac{\delta_{mn}}{\Delta x}, \tag{A.13}$$

where $k\Delta x = 2\pi n/N$. Based on this, we try to construct the non-local noise for the 5-point system in physical space. Assuming the non-local noise relates to the nearest four nodes as

$$v_{\beta,i} = A\cdot n_{\beta,i-2} + B\cdot n_{\beta,i-1} + C\cdot n_{\beta,i} + D\cdot n_{\beta,i+1}, \tag{A.14}$$

where A, B, C and D are the undetermined coefficients. Based on this definition and (A.12), the autocorrelation of $\mu_{\beta,i}$ will be

$$\begin{aligned}\left\langle v_{\beta,i}(t)v_{\beta,j}(t')\right\rangle &= \left\langle (A\cdot n_{\beta,i-2} + B\cdot n_{\beta,i-1} + C\cdot n_{\beta,i} + D\cdot n_{\beta,i+1})\right. \\ &\qquad \left.(A\cdot n_{\beta,j-2} + B\cdot n_{\beta,j-1} + C\cdot n_{\beta,j} + D\cdot n_{\beta,j+1})\right\rangle \\ &= 2\beta\theta\frac{\delta(t-t')}{\Delta x^3}\times\frac{1}{12}\begin{cases} 0, & |i-j|\geq 4 \\ AD=0, & |i-j|=3 \\ AC+BD=1, & |i-j|=2 \\ AB+BD+CD=-16, & |i-j|=1 \\ A^2+B^2+C^2+D^2=30, & |i-j|=0 \end{cases}\end{aligned} \tag{A.15}$$

There are 4 equations with 4 unknowns. The solution is:

$$\begin{matrix} A \\ B \\ C \\ D \end{matrix} = \left\{\begin{matrix} 0 \\ -2\mp\sqrt{3} \\ 4 \\ -2\pm\sqrt{3} \end{matrix}\right\}, \left\{\begin{matrix} 0 \\ 2\mp\sqrt{3} \\ -4 \\ 2\pm\sqrt{3} \end{matrix}\right\}, \left\{\begin{matrix} -2\mp\sqrt{3} \\ 4 \\ -2\pm\sqrt{3} \\ 0 \end{matrix}\right\}, \left\{\begin{matrix} 2\mp\sqrt{3} \\ -4 \\ 2\pm\sqrt{3} \\ 0 \end{matrix}\right\} \tag{A.16}$$

Now, let's calculate the non-local noise in k-space (select A=0):

$$\begin{aligned}
\tilde{\nu}_{\beta,n} &= \frac{1}{\sqrt{N}} \sum_{i=0}^{N-1} \nu_{\beta,i} e^{-\bar{i}\left[\frac{2\pi ni}{N}\right]} \\
&= \frac{1}{\sqrt{N}} \sum_{i=0}^{N-1} \left(B \cdot n_{\beta,i-1} + C \cdot n_{\beta,i} + D \cdot n_{\beta,i+1}\right) e^{-\bar{i}\left[\frac{2\pi n}{N}\right]i} \\
&= \sqrt{2\beta\theta\Delta t/\Delta x^3} \cdot \frac{1}{\sqrt{N}} \sum_{i=0}^{N-1} \left(B \cdot \sigma_{i-1} + C \cdot \sigma_i + D \cdot \sigma_{i+1}\right) e^{-\bar{i}\left[\frac{2\pi n}{N}\right]i} \\
&= \sqrt{2\beta\theta\Delta t/\Delta x^3} \cdot \frac{1}{\sqrt{N}} \sum_{i=0}^{N-1} \left[B\sigma_i e^{\bar{i}\left(\frac{2\pi n}{N}\right)} + C\sigma_i + D\sigma_i e^{-\bar{i}\left(\frac{2\pi n}{N}\right)}\right] e^{-\bar{i}\left[\frac{2\pi n}{N}\right]i} \\
&= \sqrt{2\beta\theta\Delta t/\Delta x^3} \left[Be^{\bar{i}\left(\frac{2\pi n}{N}\right)} + C + De^{-\bar{i}\left(\frac{2\pi n}{N}\right)}\right] \tilde{\sigma}_n \\
&= \sqrt{2\beta\theta\Delta t/\Delta x^3} \left[-8\sin^2\left(\frac{k\Delta x}{2}\right) - \bar{i} \cdot 2\sqrt{3}\sin\left(k\Delta x\right)\right] \tilde{\sigma}_n
\end{aligned} \tag{A.17}$$

This is one of the forms of the non-local noise in k-space. Since (A.15) has eight solutions, there should be eight similar forms in terms of complex numbers. Starting with the expression of $\nu_{\beta,i}$ in (A.17) or a general form with A, B, C and D, it is easy to show that the guessing $\nu_{\beta,i}$ given in (A.14) would satisfy (A.13) as expected.

Therefore, we have shown that discretizing the sine-Gordon equation with the 5-point central difference is equivalent to the 3-point central difference, since the equations of motion and the noises in physical and k space, although more complex, take the same form. The noises are still white noises and uncorrelated to the ones in different modes.

REFERENCES

[1] L. N. Cooper, "Bound electron pairs in a degenerate fermi gas," *Phys. Rev.*, vol. 104, pp. 1189–1190, Nov 1956.

[2] J. Bardeen, L. N. Cooper, and J. R. Schrieffer, "Theory of superconductivity," *Phys. Rev.*, vol. 108, pp. 1175–1204, Dec 1957.

[3] B.D.Josephson, "Possible new effects in superconductive tunnelling," *Physics Letters*, vol. 1, no. 7, pp. 251–253, 1962.

[4] P. W. Anderson and J. M. Rowell, "Probable observation of the josephson superconducting tunneling effect," *Phys. Rev. Lett.*, vol. 10, pp. 230–232, Mar 1963.

[5] S. Shapiro, "Josephson currents in superconducting tunneling: The effect of microwaves and other observations," *Phys. Rev. Lett.*, vol. 11, pp. 80–82, Jul 1963.

[6] E. Varoquaux, "Anderson's considerations on the flow of superfluid helium: Some offshoots," *Rev. Mod. Phys.*, vol. 87, pp. 803–854, Aug 2015.

[7] P. W. ANDERSON, "Considerations on the flow of superfluid helium," *Rev. Mod. Phys.*, vol. 38, pp. 298–310, Apr 1966.

[8] A. Barone and G. Paterno, *Physics and applications of the Josephson effect*, 1st ed. Wiley-VCH, 1982.

[9] P. W. Anderson, *SPECIAL EFFECTS IN SUPERCONDUCTIVITY in Lectures on the Many Body Problem*. Academic Press, 1964, vol. 2.

[10] B. Josephson, "Supercurrents through barriers," *Advances in Physics*, vol. 14, no. 56, pp. 419–451, 1965.

[11] A. J. Dahm, A. Denenstein, T. F. Finnegan, D. N. Langenberg, and D. J. Scalapino, "Study of the josephson plasma resonance," *Phys. Rev. Lett.*, vol. 20, pp. 859–863, Apr 1968.

[12] A. J. Dahm and D. N. Langenberg, "Nonlinear effects in the josephson plasma resonance," *Journal of Low Temperature Physics*, vol. 19, no. 1, pp. 145–167, 1975.

[13] D. E. McCumber, "Effect of ac impedance on dc voltage-current characteristics of superconductor weak-link junctions," *Journal of Applied Physics*, vol. 39, no. 7, pp. 3113–3118, 1968.

[14] W. C. Stewart, "Current-voltage characteristics of josephson junctions," *Applied Physics Letters*, vol. 12, no. 8, pp. 277–280, 1968.

[15] H. Kramers, "Brownian motion in a field of force and the diffusion model of chemical reactions," *Physica*, vol. 7, no. 4, pp. 284–304, 1940.

[16] M. Büttiker, E. P. Harris, and R. Landauer, "Thermal activation in extremely underdamped josephson-junction circuits," *Phys. Rev. B*, vol. 28, pp. 1268–1275, Aug 1983.

[17] J. Kurkijärvi, "Intrinsic fluctuations in a superconducting ring closed with a josephson junction," *Phys. Rev. B*, vol. 6, pp. 832–835, Aug 1972.

[18] L. D. Jackel, W. W. Webb, J. E. Lukens, and S. S. Pei, "Measurement of the probability distribution of thermally excited fluxoid quantum transitions in a superconducting ring closed by a josephson junction," *Phys. Rev. B*, vol. 9, pp. 115–118, Jan 1974.

[19] P. Silvestrini, O. Liengme, and K. E. Gray, "Current distributions of thermal switching in extremely underdamped josephson junctions," *Phys. Rev. B*, vol. 37, pp. 1525–1531, Feb 1988.

[20] R. F. Voss and R. A. Webb, "Macroscopic quantum tunneling in 1-μm nb josephson junctions," *Phys. Rev. Lett.*, vol. 47, pp. 265–268, Jul 1981.

[21] L. D. Jackel, J. P. Gordon, E. L. Hu, R. E. Howard, L. A. Fetter, D. M. Tennant, R. W. Epworth, and J. Kurkijärvi, "Decay of the zero-voltage state in small-area, high-current-density josephson junctions," *Phys. Rev. Lett.*, vol. 47, pp. 697–700, Aug 1981.

[22] M. H. Devoret, J. M. Martinis, and J. Clarke, "Measurements of macroscopic quantum tunneling out of the zero-voltage state of a current-biased josephson junction," *Phys. Rev. Lett.*, vol. 55, pp. 1908–1911, Oct 1985.

[23] J. M. Martinis, M. H. Devoret, and J. Clarke, "Experimental tests for the quantum behavior of a macroscopic degree of freedom: The phase difference across a josephson junction," *Phys. Rev. B*, vol. 35, pp. 4682–4698, Apr 1987.

[24] J. Clarke, A. N. Cleland, M. H. Devoret, D. Esteve, and J. M. Martinis, "Quantum mechanics of a macroscopic variable: The phase difference of a josephson junction," *Science*, vol. 239, no. 4843, pp. 992–997, 1988.

[25] A. O. Caldeira and A. J. Leggett, "Influence of dissipation on quantum tunneling in macroscopic systems," *Phys. Rev. Lett.*, vol. 46, pp. 211–214, Jan 1981.

[26] A. Caldeira and A. Leggett, "Quantum tunnelling in a dissipative system," *Annals of Physics*, vol. 149, no. 2, pp. 374–456, 1983.

[27] A. J. Leggett, S. Chakravarty, A. T. Dorsey, M. P. A. Fisher, A. Garg, and W. Zwerger, "Dynamics of the dissipative two-state system," *Rev. Mod. Phys.*, vol. 59, pp. 1–85, Jan 1987.

[28] A. J. Leggett, *Quantum tunneling of a macroscopic variable Chapter 1*. Netherlands: North-Holland, 1992.

[29] J. A. Blackburn, M. Cirillo, and N. Grønbech-Jensen, "A survey of classical and quantum interpretations of experiments on josephson junctions at very low temperatures," *Physics Reports*, vol. 611, pp. 1–33, 2016.

[30] V. Mel'nikov, "The kramers problem: Fifty years of development," *Physics Reports*, vol. 209, no. 1, pp. 1–71, 1991.

[31] V. I. Melnikov, "Activated decay rate: Finite-barrier corrections," *Phys. Rev. E*, vol. 48, pp. 3271–3284, Nov 1993.

[32] P. Hänggi, P. Talkner, and M. Borkovec, "Reaction-rate theory: fifty years after kramers," *Rev. Mod. Phys.*, vol. 62, pp. 251–341, Apr 1990.

[33] E. Pollak and P. Talkner, "Reaction rate theory: What it was, where is it today, and where is it going?" *Chaos: An Interdisciplinary Journal of Nonlinear Science*, vol. 15, no. 2, 06 2005.

[34] R. P. Feynman, R. B. Leighton, M. Sands, and S. B. Treiman, "The feynman lectures on physics," *Physics Today*, vol. 17, no. 8, pp. 45–46, 1964.

[35] J. M. Rowell, "Magnetic field dependence of the josephson tunnel current," *Phys. Rev. Lett.*, vol. 11, pp. 200–202, Sep 1963.

[36] M. D. FISKE, "Temperature and magnetic field dependences of the josephson tunneling current," *Rev. Mod. Phys.*, vol. 36, pp. 221–222, Jan 1964.

[37] T. A. Fulton and L. N. Dunkleberger, "Lifetime of the zero-voltage state in josephson tunnel junctions," *Phys. Rev. B*, vol. 9, pp. 4760–4768, Jun 1974.

[38] K. K. Likharev, *Dynamics of Josephson junctions and circuits*. [Amsterdam]: Gordon and Breach Science Publishers, 1986.

[39] V. Ambegaokar and A. Baratoff, "Tunneling between superconductors," *Phys. Rev. Lett.*, vol. 11, pp. 104–104, Jul 1963.

[40] M. Devoret, A. Wallraff, and J. Martinis, "Superconducting qubits: A short review," *arXiv*, 12 2004.

[41] K. Huang, *Statistical Mechanics*, 2nd ed. John Wiley & Sons, 1987.

[42] C. Cheng, G. Salina, N. Grønbech-Jensen, J. A. Blackburn, M. Lucci, and M. Cirillo, "Modeling escape from a one-dimensional potential well at zero or very low temperatures," *Journal of Applied Physics*, vol. 127, no. 14, p. 143901, 2020.

[43] P. Silvestrini, S. Pagano, R. Cristiano, O. Liengme, and K. E. Gray, "Effect of dissipation on thermal activation in an underdamped josephson junction: First evidence of a transition between different damping regimes," *Phys. Rev. Lett.*, vol. 60, pp. 844–847, Feb 1988.

[44] B. Ruggiero, C. Granata, V. G. Palmieri, A. Esposito, M. Russo, and P. Silvestrini, "Supercurrent decay in extremely underdamped josephson junctions," *Phys. Rev. B*, vol. 57, pp. 134–137, Jan 1998.

[45] S. Washburn, R. A. Webb, R. F. Voss, and S. M. Faris, "Effects of dissipation and temperature on macroscopic quantum tunneling," *Phys. Rev. Lett.*, vol. 54, pp. 2712–2715, Jun 1985.

[46] H. Risken and H. Haken, *The Fokker-Planck Equation: Methods of Solution and Applications Second Edition*. Springer, 1989.

[47] W. T. Coffey, Y. P. Kalmykov, and J. T. Waldron, *The Langevin Equation*, 2nd ed. WORLD SCIENTIFIC, 2004.

[48] L. D. Landau and E. M. Lifshitz, *Mechanics, Third Edition: Volume 1 (Course of Theoretical Physics)*, 3rd ed. Butterworth-Heinemann, Jan. 1976.

[49] Y. Zhou and J. Du, "Escape rate for the power-law distribution in low-to-intermediate damping," *Physica A: Statistical Mechanics and its Applications*, vol. 403, pp. 244–251, 2014.

[50] Z.-W. Bai, "Reactive flux theory for finite potential barriers," *Phys. Rev. E*, vol. 103, p. 042144, Apr 2021.

[51] P. Hanggi, "Escape from a metastable state," *Journal of Statistical Physics*, vol. 42, no. 1-2, pp. 105–148, Jan. 1986.

[52] J. J. Mazo, F. Naranjo, and D. Zueco, "Nonequilibrium effects in the thermal switching of underdamped josephson junctions," *Phys. Rev. B*, vol. 82, p. 094505, Sep 2010.

[53] E. Pollak, H. Grabert, and P. Hänggi, "Theory of activated rate processes for arbitrary frequency dependent friction: Solution of the turnover problem," *The Journal of Chemical Physics*, vol. 91, no. 7, pp. 4073–4087, 10 1989.

[54] C. Cheng, M. Cirillo, G. Salina, and N. Grønbech-Jensen, "Nonequilibrium transient phenomena in the washboard potential," *Phys. Rev. E*, vol. 98, p. 012140, Jul 2018.

[55] P. Talkner and E. Pollak, "Numerical test of finite-barrier corrections for the hopping rate in a periodic potential," *Phys. Rev. E*, vol. 47, pp. R21–R23, Jan 1993.

[56] C. Cheng, M. Cirillo, and N. Grønbech-Jensen, "Dissipation-dependent thermal escape from a potential well," *Entropy*, vol. 23, no. 10, 2021.

[57] F. T. Arecchi and A. Politi, "Transient fluctuations in the decay of an unstable state," *Phys. Rev. Lett.*, vol. 45, pp. 1219–1222, Oct 1980.

[58] A. L. Pankratov, E. V. Pankratova, V. A. Shamporov, and S. V. Shitov, "Oscillations in Josephson transmission line stimulated by load in the presence of noise," *Applied Physics Letters*, vol. 110, no. 11, p. 112601, 03 2017.

[59] N. Grønbech-Jensen and O. Farago, "A simple and effective verlet-type algorithm for simulating langevin dynamics," *Molecular Physics*, vol. 111, no. 8, pp. 983–991, 2013.

[60] L. F. G. Jensen and N. Grønbech-Jensen, "Accurate configurational and kinetic statistics in discrete-time langevin systems," *Molecular Physics*, vol. 117, no. 18, pp. 2511–2526, 2019.

[61] N. Grønbech-Jensen, "Complete set of stochastic verlet-type thermostats for correct langevin simulations," *Molecular Physics*, vol. 118, no. 8, p. e1662506, 2020.

[62] S. A. T. William H. Press, Brian P. Flannery, *Numerical Recipes in C: The Art of Scientific Computing*. Cambridge university press, 1992.

[63] J. A. Blackburn, M. Cirillo, and N. Grønbech-Jensen, "Classical statistical model for distributions of escape events in swept-bias josephson junctions," *Phys. Rev. B*, vol. 85, p. 104501, Mar 2012.

[64] P. Silvestrini, V. G. Palmieri, B. Ruggiero, and M. Russo, "Observation of energy levels quantization in underdamped josephson junctions above the classical-quantum regime crossover temperature," *Phys. Rev. Lett.*, vol. 79, pp. 3046–3049, Oct 1997.

[65] P. Silvestrini, B. Ruggiero, C. Granata, M. Russo, and V. Palmieri, "Energy levels quantization in josephson junctions," *Applied Superconductivity*, vol. 6, no. 7, pp. 379–384, 1998.

[66] H. F. Yu, X. B. Zhu, Z. H. Peng, W. H. Cao, D. J. Cui, Y. Tian, G. H. Chen, D. N. Zheng, X. N. Jing, L. Lu, S. P. Zhao, and S. Han, "Quantum and classical resonant escapes of a strongly driven josephson junction," *Phys. Rev. B*, vol. 81, p. 144518, Apr 2010.

[67] G. Oelsner, L. S. Revin, E. Il'ichev, A. L. Pankratov, H.-G. Meyer, L. Grönberg, J. Hassel, and L. S. Kuzmin, "Underdamped josephson junction as a switching current detector," *Applied Physics Letters*, vol. 103, no. 14, p. 142605, 2013.

[68] J. Kurkijärvi, "Intrinsic fluctuations in a superconducting ring closed with a josephson junction," *Phys. Rev. B*, vol. 6, pp. 832–835, Aug 1972.

[69] F. Tafuri, *Fundamentals and Frontiers of the Josephson Effect*. Springer, 01 2019.

[70] B. D. JOSEPHSON, "Coupled superconductors," *Rev. Mod. Phys.*, vol. 36, pp. 216–220, Jan 1964.

[71] A. Wallraff, A. Lukashenko, C. Coqui, A. Kemp, T. Duty, and A. V. Ustinov, "Switching current measurements of large area Josephson tunnel junctions," *Review of Scientific Instruments*, vol. 74, no. 8, pp. 3740–3748, 07 2003.

[72] J. Männik, S. Li, W. Qiu, W. Chen, V. Patel, S. Han, and J. E. Lukens, "Crossover from kramers to phase-diffusion switching in moderately damped josephson junctions," *Phys. Rev. B*, vol. 71, p. 220509, Jun 2005.

[73] K. Inomata, S. Sato, K. Nakajima, A. Tanaka, Y. Takano, H. B. Wang, M. Nagao, H. Hatano, and S. Kawabata, "Macroscopic quantum tunneling in a d-wave high-T_C $bi_2sr_2cacu_2o_{8+\delta}$ superconductor," *Phys. Rev. Lett.*, vol. 95, p. 107005, Sep 2005.

[74] S.-X. Li, W. Qiu, S. Han, Y. F. Wei, X. B. Zhu, C. Z. Gu, S. P. Zhao, and H. B. Wang, "Observation of macroscopic quantum tunneling in a single $bi_2sr_2cacu_2o_{8+\delta}$ surface intrinsic josephson junction," *Phys. Rev. Lett.*, vol. 99, p. 037002, Jul 2007.

[75] D. J. Cui, H. F. Yu, Z. H. Peng, W. H. Cao, X. B. Zhu, Y. Tian, G. H. Chen, D. H. Lin, C. Z. Gu, D. N. Zheng, X. N. Jing, L. Lu, and S. P. Zhao, "Macroscopic quantum tunneling and qubit design parameters of $bi_2sr_2cacu_2o_{8+\delta}$ surface intrinsic josephson junctions," *Superconductor Science and Technology*, vol. 21, no. 12, p. 125019, oct 2008.

[76] H. F. Yu, X. B. Zhu, J. K. Ren, Z. H. Peng, D. J. Cui, H. Deng, W. H. Cao, Y. Tian, G. H. Chen, D. N. Zheng, X. N. Jing, L. Lu, and S. P. Zhao, "Resonant phase escape in $bi_2sr_2cacu_2o_{8+\delta}$ surface intrinsic josephson junctions," *New Journal of Physics*, vol. 15, no. 9, p. 095006, sep 2013.

[77] D. Massarotti, A. Pal, G. Rotoli, L. Longobardi, M. G. Blamire, and F. Tafuri, "Macroscopic quantum tunnelling in spin filter ferromagnetic josephson junctions," *Nature Communications*, vol. 6, no. 1, p. 7376, 2015.

[78] I. Affleck, "Quantum-statistical metastability," *Phys. Rev. Lett.*, vol. 46, pp. 388–391, Feb 1981.

[79] J. A. Blackburn, M. Cirillo, and N. Grønbech-Jensen, "Switching current distributions in josephson junctions at very low temperatures," *Europhysics Letters*, vol. 107, no. 6, p. 67001, sep 2014.

[80] N. Grønbech-Jensen, "On the application of non-gaussian noise in stochastic langevin simulations," *Journal of Statistical Physics*, vol. 190, no. 5, p. 96, 2023.

[81] A. C. Scott and W. J. Johnson, "INTERNAL FLUX MOTION IN LARGE JOSEPHSON JUNCTIONS," *Applied Physics Letters*, vol. 14, no. 10, pp. 316–318, 10 2003.

[82] T. Fulton and R. Dynes, "Single vortex propagation in josephson tunnel junctions," *Solid State Communications*, vol. 12, no. 1, pp. 57–61, 1973.

[83] M. Salerno, E. Joergensen, and M. R. Samuelsen, "Phonons and solitons in the "thermal" sine-gordon system," *Phys. Rev. B*, vol. 30, pp. 2635–2639, Sep 1984.

[84] M. Salerno, M. R. Samuelsen, and H. Svensmark, "Thermal sine-gordon system in the presence of different types of dissipation," *Phys. Rev. B*, vol. 38, pp. 593–596, Jul 1988.

[85] N. Grønbech-Jensen, M. Salerno, and M. R. Samuelsen, "Effect of thermal noise on the phase locking of a josephson fluxon oscillator," *Phys. Rev. B*, vol. 46, pp. 308–316, Jul 1992.

[86] A. V. Ustinov, M. Cirillo, and B. A. Malomed, "Fluxon dynamics in one-dimensional josephson-junction arrays," *Phys. Rev. B*, vol. 47, pp. 8357–8360, Apr 1993.

[87] A. Wallraff, E. Goldobin, and A. V. Ustinov, "Numerical analysis of the coherent radiation emission by two stacked Josephson flux-flow oscillators," *Journal of Applied Physics*, vol. 80, no. 11, pp. 6523–6535, 12 1996.

[88] N. Grønbech-Jensen and M. R. Samuelsen, "Magnetic interaction between spatially extended superconducting tunnel junctions," *Phys. Rev. B*, vol. 65, p. 144512, Mar 2002.

[89] T. Finnegan and S. Wahlsten, "Observation of coherent microwave radiation emitted by coupled Josephson junctions," *Applied Physics Letters*, vol. 21, no. 11, pp. 541–544, 10 2003.

[90] A. Barone, F. Esposito, C. J. Magee, and A. C. Scott, "Theory and applications of the sine-gordon equation," *La Rivista del Nuovo Cimento (1971-1977)*, vol. 1, no. 2, pp. 227–267, 1971.

[91] A. C. Scott, F. Y. F. Chu, and S. A. Reible, "Magnetic-flux propagation on a Josephson transmission line," *Journal of Applied Physics*, vol. 47, no. 7, pp. 3272–3286, 07 1976.

[92] K. Likharev and V. Semenov, "Rsfq logic/memory family: a new josephson-junction technology for sub-terahertz-clock-frequency digital systems," *IEEE Transactions on Applied Superconductivity*, vol. 1, no. 1, pp. 3–28, 1991.

[93] W. Wustmann and K. D. Osborn, "Reversible fluxon logic: Topological particles allow ballistic gates along one-dimensional paths," *Phys. Rev. B*, vol. 101, p. 014516, Jan 2020.

[94] K. D. Osborn and W. Wustmann, "Reversible fluxon logic with optimized cnot gate components," *IEEE Transactions on Applied Superconductivity*, vol. 31, no. 2, pp. 1–13, 2021.

[95] A. V. Ustinov, "Long Josephson junctions and stacks," *AIP Conference Proceedings*, vol. 427, no. 1, pp. 31–55, 05 1998.

[96] G. Costabile, R. D. Parmentier, B. Savo, D. W. McLaughlin, and A. C. Scott, "Exact solutions of the sine-Gordon equation describing oscillations in a long (but finite) Josephson junction," *Applied Physics Letters*, vol. 32, no. 9, pp. 587–589, 5 1978.

[97] Z. Li, *Travelling Wave Solutions to Nonlinear Equations of Mathematical Physics (Chinese version)*. Science Press, 01 2007.

[98] N. Grønbech-Jensen, Y. S. Kivshar, and M. R. Samuelsen, "Nonlinear dynamics of a parametrically driven sine-gordon system," *Phys. Rev. B*, vol. 47, pp. 5013–5021, Mar 1993.

[99] D. W. McLaughlin and A. C. Scott, "Perturbation analysis of fluxon dynamics," *Phys. Rev. A*, vol. 18, pp. 1652–1680, Oct 1978.

[100] E. Joergensen, V. P. Koshelets, R. Monaco, J. Mygind, M. R. Samuelsen, and M. Salerno, "Thermal fluctuations in resonant motion of fluxons on a josephson transmission line: Theory and experiment," *Phys. Rev. Lett.*, vol. 49, pp. 1093–1096, Oct 1982.

[101] A. C. Scott, "A Nonlinear Klein-Gordon Equation," *American Journal of Physics*, vol. 37, no. 1, pp. 52–61, 01 1969.

[102] N. Grønbech-Jensen, "Modeling Stochastic, Thermal Partial Differential Equations," 2017, unpublished.

[103] C. Lecomte, "Zero and root loci of disturbed spring-mass systems," *Proceedings of the Royal Society A: Mathematical, Physical and Engineering Sciences*, vol. 470, no. 2164, p. 20130751, 2014.

[104] J. Cuevas-Maraver, P. Kevrekidis, and F. Williams, *The sine-Gordon Model and its Applications: From Pendula and Josephson Junctions to Gravity and High-Energy Physics*. Springer, 01 2014.

[105] R. Rajaraman, "Solitons and instantons. an introduction to solitons and instantons in quantum field theory," Jan 1982.

[106] R. Pathria, *Statistical Mechanics*. PERGAMON PRESS, 1972.